# Using STORM and TIRF in tandem to investigate adherence and migration patterns in stem cells.

by

Sandisiwe Manyathi-Mankwali Matyesini

*Thesis presented in fulfilment of the requirements for the degree of Master of Science in the Faculty of Medicine and Health Sciences at Stellenbosch University*

Supervisor: Dr Mari van de Vyver
Co-supervisors: Mrs Lize Engelbrecht & Dr Derick van Vuuren

March 2021

## Declaration

By submitting this thesis electronically, I declare that the entirety of the work contained therein is my own, original work, that I am the sole author thereof (save to the extent explicitly otherwise stated), that reproduction and publication thereof by Stellenbosch University will not infringe any third party rights and that I have not previously in its entirety or in part submitted it for obtaining any qualification.

March 2021

**Abstract**

**Background:** Cell migration is a dynamic process in physiology requiring pseudopodia, elongated cell protrusions, to associate with the extracellular matrix (ECM) and propel cells forward. The interaction is established with the assembly and disassembly of focal adhesion (FA) complexes, acting as signalling centres for communication between the ECM and the cell. Alterations within the ECM and its key proteins, such as collagen, elicit responses through the FA complexes. Here, collagen deposition was stimulated in mesenchymal stem cells (MSC) through the addition of ascorbic acid-2-phosphate (AAP). AAP is stable ascorbic acid derivative that enhances collagen synthesis and cell growth. The altered matrix stiffness allowed FA proteins forming these complexes to change as needed in response to stimuli. In this study the elusive assembly of key FA proteins, integrin β1, talin and vinculin were assessed in collagen reinforced migrating cells with various microscopy techniques, including TIRF and STORM.

**Methods:** The optimal AAP concentration (0.6mM) which did not affect cell viability was determined with a crystal violet dose response assay. Cell migration with and without AAP was assessed at (control at 0h) and 8h, a time point selected from a 24h live cell imaging experiment when distinct pseudopodia were visible in all groups. Thereafter, an immunocytochemistry (ICC) protocol was established to investigate the impact of AAP supplementation during migration on talin, vinculin and integrin-β1. Protein expression, as well as co-localisation of these proteins were determined. TIRF microscopy provided a tool for visualization of the FA complexes at the level of attachment as it imaged the focal plane directly above the coverslip. The FA complex length, breadth and area were determined using image analysis software (FIJI). Finally, STORM was optimised and applied on talin stained samples to establish if finer structural changes during migration could be revealed.

**Results:** Talin and integrin-β1 co-occurred while the majority of vinculin centralized around the nucleus irrespective of cell migration with or without AAP supplementation. TIRF assessment of FA in AAP treated migrating cells indicated a significant difference in FA complex sizes compared to SGM migrating cells with distinct and prominent FA complexes clearly visible.

**Conclusion:** Cell migration in AAP supplemented media was reduced due to increased FA proteins responding to the stiff ECM. Similarly, TIRF generated data portrayed dense prominent structures, eliminating all out of focus light and increase the FA complex contrast. The improved TIRF resolution, highlighted that AAP migrating cells FA complexes were bigger in size compared to FA in SGM migrating cells.

**Opsomming**

**Agtergrond:** Selmigrasie is 'n dinamiese proses in fisiologie wat gebruik maak van pseudopodiam of selverlengings wat assosieer met die ekstrasellulêre matriks (ESM) en selle vorentoe dryf. Die interaksie word met die opbou en afbreek van fokale adhesie (FA) -komplekse bewerkstellig, wat as sentrums dien vir kommunikasie tussen die ESM en die sel. Veranderinge binne die ESM en die belangrikste proteïene daarin, soos kollageen, veroorsaak reaksies deur en van die FA-komplekse. Hier is askorbiensuur-2-fosfaat (AAP) aangevul aangesien dit bekend is dat AAP kollageenneerlegging stimuleer. AAP is 'n stabiele askorbiensuurderivaat wat kollageensintese en selgroei verbeter. Die veranderde rigiditeit van die matriks laat FA-proteïene wat hierdie komplekse vorm, toe om te verander soos nodig om op stimuli te kan reageer. In hierdie studie is die samestelling van belangrike FA-proteïene, integrien β1, talien en vinkulien in kollageenversterkte migrerende selle met verskillende mikroskopietegnieke, insluitend TIRF en STORM ondersoek.

**Metodes:** Die optimale AAP-konsentrasie (0.6mM) wat nie die lewensvatbaarheid van die sel beïnvloed nie, was deur ‘n kristalviolet-dosisresponstoetse bepaal. Selmigrasie met en sonder AAP was om 0h (kontrole) en 8h ondersoek; die gekose tydspunt uit 'n 24h lewendige-sel-waarneemingseksperiment waartydens duidelike pseudopodia in alle groepe sigbaar was. Daarna was 'n immunositochemiese protokol opgestel om die impak van AAP-aanvulling tydens migrasie op talien, vinkulien en integrien-β1 te ondersoek. Proteïenuitdrukking, sowel as medelokalisering van hierdie proteïene was bepaal. TIRF-mikroskopie het voorsien vir die visualisering van die FA komplekse op die vlak van aanhegting, aangesien dit die fokusvlak direk bokant die dekglas kon beeld. Die FA-lengte, breedte en oppervlakte was met behulp van beeldanalise-sagteware (FIJI) bepaal. Laastens wasdie STORM tegniek geoptimaliseer en toegepas op taliengekleurde monsters om vas te stel of fyner strukturele veranderinge tydens migrasie waargeneem kan word.

**Resultate:** Talien en integrien-β1 het saam gegroepeer terwyl die meerderheid vinkulien rondom die kern gesentraliseer het, ongeag van selmigrasie met of sonder AAP-aanvulling. TIRF-assessering van FA in migrasieselle wat deur AAP behandel is, dui op 'n beduidende verskil in FA-kompleksgroottes in vergelyking met SGM-migrerende selle met duidelike en prominente FA-komplekse wat duidelik sigbaar is.

**Gevolgtrekking:** Selmigrasie in AAP aangevulde media was verminder as gevolg van verhoogde FA proteïene wat reageer op die teenwoordigheid van die rigiede ECM. Soortgelyk het die TIRF gegenereerde data digte prominente strukture uitgebeeld, wat al die lig wat nie in fokus was nie uitgeskakel het en die kotras van die FA komplekse verhoog het. Die verbeterde TIRF-resolusie het beklemtoon dat AAP-migrerende selle se FA-komplekse groter was in vergelyking met FA in SGM-migrerende selle.

## Acknowledgements

My sincere gratitude for the funding provided by **Zeiss** and the **National Research Foundation** to complete this study. It truly would have not been possible without this assistance.

**Dr Mari Van de Vyver and Mrs Lize Engelbrecht:** I would like to honour you for the support, encouragement, and faith that you had in me from day one of this journey. You have played such a pivotal role not only in my career but in my life. I will forever be grateful for the opportunity to be guided and mentored by such powerhouses.

**Dr Derick van Vuuren:** Thank you for your constant willingness to assist the team during this journey.

**Stephen Hugh Lab Colleagues**: Thank you for welcoming me into the group with open arms and truly making this place home. I have learned a lot from all of you and I will miss you dearly.

**Praying Huns:** Nomonde Ngoma, Neliswa Ndlovu and Sinothando Mbanjwa I would have not made it without your constant support in faith and availability to pray with and for me. You are truly God sent.

**Cum Laude Squad:** Thank you for everything. Thank you for being my sanity when I needed it most. I could have not asked for a better second family. I love you… I wrote it down.

Thank you to the following people whose contribution to my journey has undoubtably led me thus far: Dr Koketso Mogwera (and Strauss Lab, Biochemistry), Mrs Aboyeji, Mr Kiziri, Mr Makumbi, Mrs Stellenberg (Aunt Debie) (and Royal Academy staff).

Finally, God. Thank you. Wandithwala ebudeni balendlela, ndiyabulela Nkosi. Xandiyekelelwa nguwe ndiyophalala njemgamanzi.

## Dedication

*For my people,*

Nolubabalo Patiswa Matyesini, Ntandazo Matyesini, Siyasamkela Economy Matyesini, Papama Mapukata-Prusente

I am what a person looks like when love and support has been poured into them. You are my entire being.

Thank You for Everything.

*For my people,*

OoNyathi, Ngqila, Budede, Omwanda, Nodwengu, Nogixa, Nokhonza sihlobo sikaTshula, sikaNtongo, Omabandezi fusi engazukulilima.

Mankwali, Bukula, Mkhwanase, Magcoba, Jijila, Lusu, Nkonjane ebhabha emafini, Mashwabatha inkomo nempondo zayo.

The greatest honour I will ever have is representing you wherever I go.

I am because you were.

Thank You for Everything.

*For my people,*

Black Child.

You are worthy. All that you dream is worthy. Stay true to all that you are.

I am rooting for you, always and forever.

# List of Tables

## List of Figures

## Abbreviations

**AA:** Ascorbic acid

**AAP:** Ascorbic acid 2-phosphate

**Ab1:** Primary antibodies

**Ab2:** Secondary antibodies

**BME:** β-mercapto-ethanol

**$CO_2$:** Carbon dioxide

**DIC:** Differential Interference Contrast

**DMEM:** Dulbecco's Modified Eagle Medium

**DMSO:** Dimethyl sulfoxide

**ECM:** Extracellular Matrix

**EMCCD:** Electron Multiplying Charged Couple Device

**EM gain:** Electron Multiplying Gain

**FAK:** Focal Adhesion Kinase

**FBS:** Foetal bovine serum

**GFP:** Green Fluorescent Protein

**Grb2:** Growth factor receptor-bound *protein*-2

**HCl:** Hydrochloric acid

**ICC:** Immunocytochemistry

**KCl:** Potassium Chloride

**$KH_2HPO_4$:** Monopotassium Phosphate

**L:** Litre

**LH:** Lysly-3-hydroxylase

**MEA:** Mercapto-ethylamine

**MFI:** Mean Fluorescence Intensity

**MIP:** Maximum Intensity Projection

**Mit. C:** Mitomycin C

**Min:** Minutes

**ml:** Millilitre

**mg/L:** Milligram per litre

**mM:** Millimolar

**MSC:** Mesenchymal stem cell

**ms:** Milliseconds

**NA:** Numerical Aperture

**NaCl:** Sodium Chloride

**$Na_2HPO_4$:** Disodium Phosphate

**nm:** Nanometre

**PALM:** Photoactivation Localization Microscopy

**PBS:** Phosphate buffered saline

**PenStrep:** Penicillin-Streptomycin

**PIP2:** Phosphoinositide

**PI3K**: Phosphatidylinositol 3-kinase

**PSF:** Point Spread Function

**P3H:** Prolyl-3-hydroxylase

**P4H:** Prolyl-4-hydroxylase

**ROI:** Region of Interest

**RPM:** Revolutions per minute

**RT-PCR:** Reverse transcription polymerase chain reaction

**sec:** seconds

**SGM:** Standard growth media

**SIM:** Structured Illumination Microscopy

**SNR:** Signal to Noise ratio

| | |
|---|---|
| **SR:** | Super Resolution |
| **SRM:** | Super Resolution Microscopy |
| **STED:** | Stimulated Emission Depletion |
| **STORM:** | Stochastic Optical Reconstruction Microscopy |
| **TIRF:** | Total Internal Reflection Fluorescence |
| **TL LED:** | Tube Lens light emitting diode |
| **tM1:** | Mander's coefficient channel 1 |
| **tM2:** | Mander's coefficient channel 2 |
| **VASP:** | Vasodilator-stimulated phosphoprotein |
| **Vh:** | Vinculin head |
| **Vt:** | Vinculin talin |
| **3D:** | 3 dimensional |
| **h:** | Hours |
| **˚C** | degree Celsius |
| **µl:** | Microlitre |
| **µm:** | Micrometer |
| **µm/sec:** | Micrometer per second |

# Chapter 1: Introduction

The progression of human curiosity in biological structures and processes over the centuries has sparked interest in developing various approaches to study life forms at lower levels, from using 'simple' lamp-based microscopes to the current highly specific super resolution microscopes (Chen *et al.,* 2011). The evolution of microscopes to the establishment of super resolution microscopy (SRM) was fundamental in improving axial and lateral resolution (McNamara *et al.,* 2017). SRM improves spatial resolution beyond the diffraction limit (the limitation of a microscope to resolve two objects apart) (Bates *et al.,* 2013). Currently, there are several super resolution techniques including Stochastic Optical Reconstruction Microscopy (STORM); a technique that activates single photoactivatable fluorophores thereby improving resolution through high precision molecule specificity and localization (Yamanaka *et al.,* 2014). The improved STORM resolution can be further enhanced with the combination of other techniques such as Total Internal Reflection Fluorescence (TIRF) microscopy. TIRF excites fluorophores at an angle thus imaging incredibly thin sample sections and by doing so further improves the axial resolution (Axelrod *et al.,* 2016). Imaging resolution is influenced and regulated by sample preparation, microscope acquisition setup, processing algorithms, and post-processing systems. The maintenance of the imaging proficiency is crucial in generating high quality images that are central in a variety of research fields, such as health sciences developing and applying X-ray microscopy in radiography (Yamamoto *et al.,* 2006; Morin & Mahesh, 2018).

The aim of this research project was to optimize STORM and TIRF techniques in our laboratory whilst investigating the adhesion protein patterns in migrating mesenchymal stem cells (MSCs). Cell migration is a central function in living life forms and is essential in many processes such as wound healing, immune responses, embryonic development, and the maintenance/repair of tissues. Whilst cellular migration is notably important, uncontrollable regulation or impairment thereof can have a detrimental impact on tissue regeneration and can be a contributing factor in the progression of various diseases. Altered migration leading to impaired wound healing is at least in part due to a deviation in the expression pattern of various adhesion proteins, depending on cell type (Vicente-Manzanares *et al.,* 2005; de Lucas *et al.,* 2018; Dormann *et al.,* 2006). In this study, the involvement of key adhesion proteins (such as talin, vinculin and integrin-β1) in cellular migration was investigated using STORM and TIRF in MSCs. The effect of the extracellular matrix (ECM) on the expression of these proteins was furthermore investigated by supplementing the cell culture media with Ascorbic acid 2-phosphate (AAP). AAP is well-known to stimulate the synthesis and deposition of a key ECM component, collagen, thus reinforcing the strength of the ECM (Hata *et al.,* 1989; Padayatty *et al,* 2017; Bonnans *et al,* 2014).

The literature review (chapter 2) will highlight the significance of microscopy in biological research by providing a detailed journey of the developments in microscopy throughout history to the current available techniques. The literature review will also emphasize the impact of such developments by focusing on the physiological role of specific adhesion proteins during the migration of MSCs.

The purpose of this study was STORM and TIRF method development, with the supporting aim of investigating the expression patterns of the adhesion proteins during cell migration. More specifically to optimize a) sample preparation and immunofluorescent staining procedures, b) confocal microscope settings and c) image analysis and data processing. This was achieved in three phases as explained in the materials and methods chapter (chapter 4). The initial focus was on determining the optimal AAP concentration and subsequently the ideal time point during cell migration when pseudopodia are prominent. The immunocytochemistry (ICC) staining protocol was optimized by comparing the effects of different fixatives for varying durations, hence providing a standard sample preparation protocol. Primary and secondary antibody titrations were subsequently performed, and the optimised conditions used for investigating protein patterns in migrating and non-migrating MSCs using confocal microscopy. For the STORM and TIRF, various microscopy settings were compared to establish the optimal imaging conditions. These findings are presented in both the methods (chapter 4) and results (chapter 5) chapters. This is followed by a discussion of the research outcome of the adhesion protein expressed and STORM and TIRF imaging with limitations being highlighted and suggestions compiled for possible future improvements (chapters 6 and 7). The conclusion (chapter 8) will furthermore indicate the potential application in combining these techniques in future studies.

# Chapter 2: Literature Review

Microscopy is an invaluable tool in biological research and with constant technological advances, it is an evolving field. To date, microscopy has enabled not only the morphological study of cellular structures but has also allowed for the quantification of protein expression, protein-protein interactions, and cellular localization to elucidate various biological processes. This chapter will first give an overview and brief history of microscopy before discussing its in-depth application in the study of cellular migration and the physiological role of focal adhesion proteins in migration.

## 2.1 MICROSCOPY: Brief History and Overview of Techniques

### 2.1.1 Brief history of microscopy

There are varying accounts in historic records as to when microscopy begun; whether from ancient Egyptians 800 B.C. or 1st century roman philosophers. Nonetheless these societies described what they saw with glass lenses of the times, as “large and distinct” (Rochow & Rochow, 1978). These observations solidified the interest of magnifying small objects, which permeated throughout the years (Chen *et al.,* 2011). The “who invented the microscope” debate evolved through the decades arguing that Hans and Zacharias Jensen should be considered for their work of using multiple lenses to make a compound microscope during the 1590s (Nimesh & Nimesh, 2017). However, the title of “Father of Microscopy” was mainly ascribed to Robert Hook and Antonio von Leeuwenhoek. In 1665, Robert Hook published the book *Micrographia,* also known as *Some Physiological Descriptions of Minute Bodies, made by Magnifying Glasses.* In his observations he studied the detail of feathers, needles, snow, and the famous flea depicted in Figure 2.1.1A. (Davidson *et al.,* 2010). Meanwhile, Antonio von Leeuwenhoek during the late 1600s developed single lens microscopes which he used to identify microorganisms such as bacteria and protozoa for the first time referring to these creature as *“little animalcule*” (Fig. 2.1.1B) (Lane *et al.,* 2015).

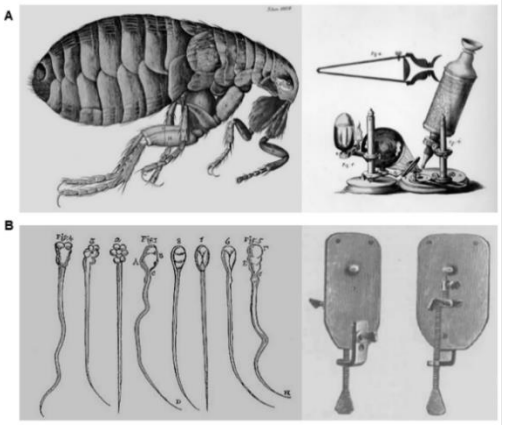


**Figure 2.1.1 Fathers of Microscopy Discoveries**. **(A)** Robert Hooke’s famous Flea Drawing in the 1665 Micrographia publication which was visualized using a compound magnifying microscope lens and **(B)**

Spermatozoa observed with a single lens microscope, visualized by Antonio Leeuwenhoek published in 1678 (adopted from Karamanou, 2010; [https://royalsociety.org/blog/2020/07/micrographia-online])

Almost two centuries later (1800s), Ernst Abbe in partnership with Carl Zeiss made innovative discoveries that revolutionized microscopic imaging methods. Abbe become well known for his work in optics including the invention of apochromatic lens which corrected chromatic aberration, the inability of lenses to focus colours on the same position (McFadden, 2000; Wimmer, 2017). For the purpose of this research study, Abbe's work revealed the existence of the resolution limit of lenses which he noted was independent of lens material or any system improvement (Davidson, 2009). Nonetheless, the latter did not deter advancements in microscopy. Marvin Minsky in 1957 developed confocal microscopy which focused on eliminating out of focus light thus improving image resolution (Singh, 1998). While the resolution limit still held true, Ernst Ruska and Max Knoll constructed an electron microscope that overcame the theoretical barrier resolution in optical microscopes at 200nm (Freundlich, 1963). With the constant need for advancement, subsequent conversations rose attempting to manipulate the above-mentioned limit and introduce a new passageway for research in investigating processes and structures occurring below the diffraction limit. The resolution limit was challenged and bypassed with the establishment of super resolution (SR) techniques (Yamanaka *et al.,* 2014). An illustration of the latter is the recent detailed analysis of mitochondrial structure using SR techniques (Jakobs & Wurm, 2014). The development of SRM opened the door for numerous advanced microscopy principals with a variety of applications especially in biological sciences as will be discussed later in this chapter. The chronological timeline depicted in Figure 2.1.2 summarized major advancements in microscopy throughout the years.

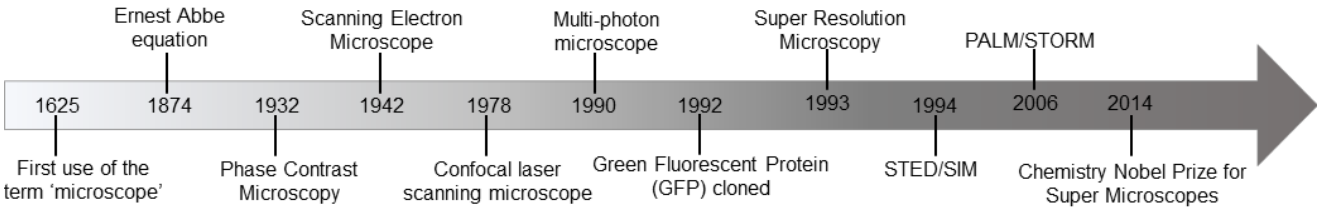


**Figure 2.1.2 Summary of Major Microscopy Advancements.** A concise timeline of the developments in microscopy technology; from the first use of the phrase 'microscope' to the latest innovations in microscopes that enable precise single molecule localizations during imaging.

## 2.1.2 Light Microscopy: Brightfield and Fluorescence

The basic principle of light microscopy is passing incident light through a series of lenses to focus on a sample and with the assistance of objective lenses the magnified sample is observed. There are two classifications of light microscopy, brightfield and fluorescence microscopy (Thorn & Kellogg, 2016). Brightfield microscopy includes Phase Contrast and Differential Interference Contrast (DIC) microscopy. Both these applied techniques yield high contrast images of thin and transparent cells

(Selinummi *et al.,* 2009; Hauch & Ratner, 2012). The DIC compared to phase contrast creates pseudo 3 dimensional (3D) images, nonetheless, both techniques are suitable for pseudopodia visualization in cellular adherence or migration studies (Paper et al., 1846).

Fluorescence microscopy, in comparison to brightfield techniques, presents higher optical contrast and specificity of sample regions during imaging. It is dependent on the use of fluorophores either as dyes to stain specific cellular structures or as conjugations with antibodies to bind specific proteins of interest (Rasnik *et al.,* 2006). Fluorescent imaging occurs when a molecule, called a fluorophore, absorbs a photon of a known wavelength and emits a lower energy impulse (with a higher wavelength) in relation to the incident photon (Martynov *et al.,* 2016). A diverse range of fluorophores is available with different properties, modes of action and target sites in a cell (Velde *et al.,* 2018). The obtainable fluorophores are either organic or inorganic, with inorganic dyes currently more accessible. The selection of fluorophores for any experiments are made on the following criteria: fluorophore excitation and emission spectra, quantum yield and extinction coefficient, detected photons per cycle, survival fraction and switching cycle (Dempsey *et al.,* 2011; Lavis *et al,* 2008; Fili and Toseland, 2014). Noting that fluorophore efficiency also depends on the fluorophore environment and acquisition settings such as laser power and laser exposure time (Li and Vaughan, 2019). A well-established and pliable/versatile fluorophore in living cells fulfilling the previous mentioned standards is the Photoactivatable Green Fluorescent Protein (GFP), which inspired the derivation of a plethora of stable fluorophore to date (Momethylase, 2002; Dempsey *et al.,* 2011). Table 1 provides a short summary of some available fluorophores and properties.

Table 1: Examples of several commercially available fluorophores with their characteristics.

| Dye | | Excitation and Emission Maximum (nm) | Extinction coefficient ($M^{-1}$ $cm^{-1}$) | Quantum yield | Detected Photons per cycle (MEA) | Survival Fraction (400s) (MEA) | Switching Cycle (Mean) (MEA) |
|---|---|---|---|---|---|---|---|
| Blue-absorbing | Alexa Fluor 488 | Ex.: 495<br>Em.: 519 | 71 000 | 0.92 | 1.193 | 0.94 | 16 |
| | Cy2 | Ex.: 489<br>Em.: 506 | 150 000 | 0.12 | 6.141 | 0.12 | 0.4 |
| Yellow-absorbing | Alexa Fluor 568 | Ex.: 578<br>Em.: 603 | 91 300 | 0.69 | 2.826 | 0.58 | 7 |
| | Cy3 | Ex.: 550<br>Em.: 570 | 150 000 | 0.15 | 11.022 | 0.17 | 0.5 |
| Red-absorbing | Alexa Fluor 647 | Ex.: 650<br>Em.: 665 | 239 000 | 0.33 | 3.823 | 0.83 | 14 |
| | Cy5 | Ex.: 649<br>Em.: 670 | 250 000 | 0.28 | 4.254 | 0.75 | 10 |
| NIR-absorbing | Alexa Fluor 750 | Ex.: 749<br>Em.: 775 | 240 000 | 0.12 | 437 | 0.36 | 1.5 |
| | Cy7 | Ex.: 747<br>Em.: 776 | 200 000 | 0.28 | 852 | 0.48 | 5 |

**Footnote:** All dyes tested were in the presence of buffer GLOX and 10mM MEA. *The fluorophore criteria was considered:* Extinction coefficient: quantity of absorbed light at a known wavelength. Quantum yield: probability of energy emission after excitation. The detected photons are considered per blinking/switching event. Survival Fraction of each dye was taken after 400s of sample illumination. The average of the number of switching cycles (switching cycles are fluorescently on and off state transitions.)

The fluorophore (probes) excitation and emission spectra are important in determining specific practical applications of a fluorophore functioning. Stoke shift, the difference between probe excitation and emission maxima, as described with a Jablonski energy diagram in Figure 2.1.3 elucidates the pathway of an incoming excitation photon. A fluorophore emits light with a longer wavelength and low energy compared to the incident excitation light. The energy lost in the system, through heat or vibration, consists of wavelengths 10nm – 100nm longer than the absorbed light (Stokes, 1998; Zhenga *et al.,* 2012). The detection of emitted light by a microscope is made possible through filtering and guided path of filters and dichromatic mirrors that block unwanted wavelengths that will contaminate the visualized image (Sanders *et al.,* 2016). The highlighted path illustrated in Figure 2.1.4 of a standard fluorescence microscope indicate the route to fluorophore excitation, emission, and detection. The light, from a laser or lamp, passes through the selective excitation filter to the selective dichromatic mirror and from there through a series of lenses to the sample. The dual dichromatic mirror allows the emitted light from the sample through the objectives, to pass the emission filter and create an image from the detected signal (Merchant *et al.,* 2009). Given the specific excitation and emission wavelength ranges of different fluorophores it is thus possible to combine multiple fluorophores in a single experiment to visualize different proteins/cellular structures simultaneously, thereby allowing assessment of not only their expression, but also interaction in a physiological setting (Hoffman, 2005).

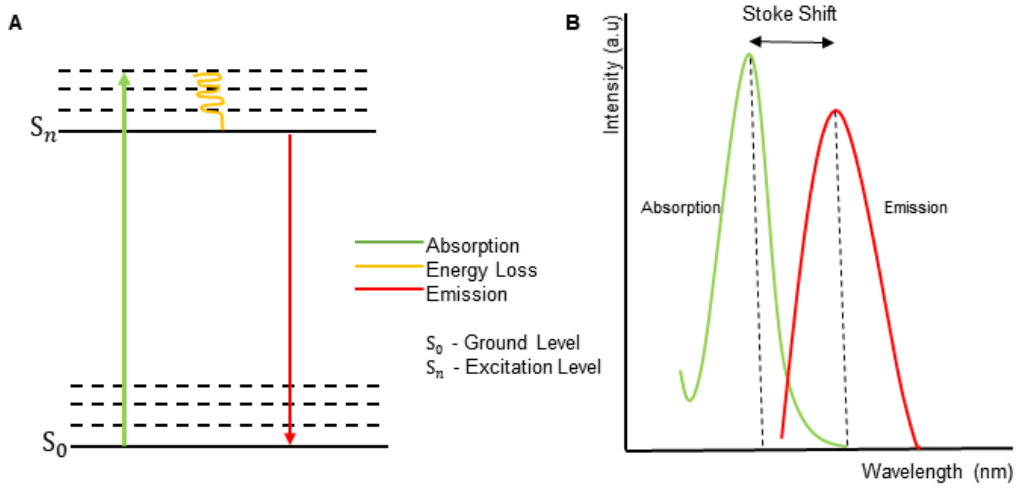


**Figure 2.1.3 Stoke Shift Overview. (A)** Jablonski energy diagram: An electron absorbs energy and moves from Ground Level ($S_0$) to Excitation Level ($S_n$) (green line). The electron is unstable in this manner and releases the energy from $S_n$ to $S_0$ (red line). Electrons are constantly vibrating hence the spontaneous energy loss (yellow line) in the system. **(B)** The difference of the absorption (green curve) and emission (red curve) amplitudes results in a Stoke Shift. The emitted energy has a longer wavelength and lower energy compared to the absorbed energy.

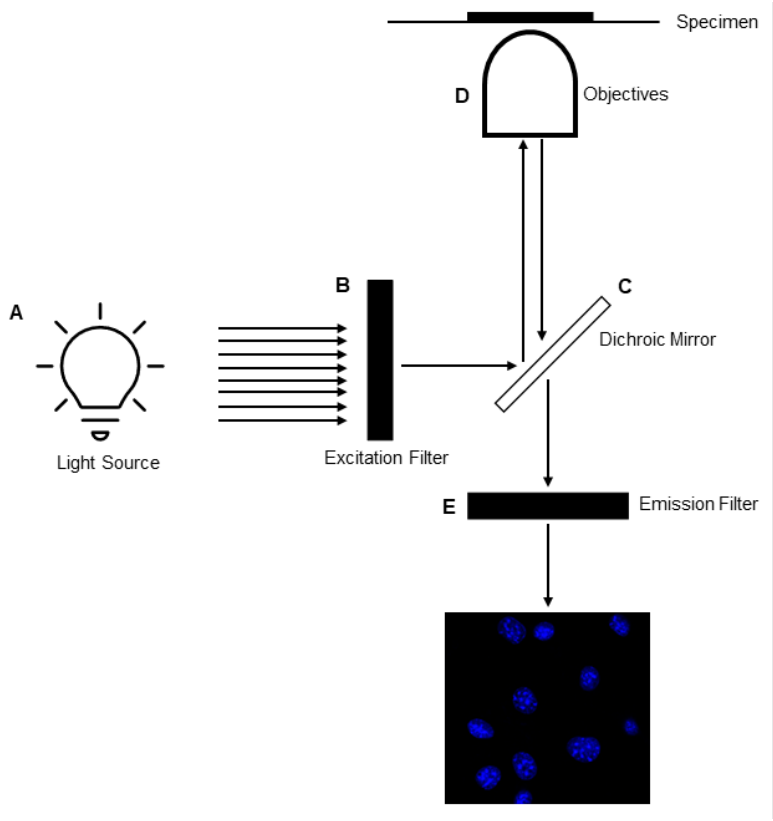


**Figure 2.1.4 Typical Fluorescent Microscope Setup.** The excitation path begins with **(A)** a laser or lamp that passes through the **(B)** excitation filter that permits a specific wavelength of light to pass through. **(C)** The selective dichromatic mirror directs the selected wavelength to the **(D)** objective lenses that allow the sample to be illuminated. The emission light from the sample pass through to the dichromatic mirror and continues path to the **(E)** emission filter which preserves image quality by blocking any scattered light. The camera detects the incoming emitted signal and translates it by constructing an image on the screen

## 2.1.3 The Diffraction Limit as limitation in microscopy

Fluorescence microscopes, as previously discussed, are efficient in providing sharp contrast images, however, the diffraction limit of light presents a constraint for target structure precision during imaging (Won, 2009; Heintzmann & Gustafsson, 2009). The diffraction limit refers to the inability of a microscope to distinguish or resolve two closely localized objects apart. Figure 2.1.5 shows various samples imageable above and below the diffraction limit. The diffraction limit of a given wavelength passing through an objective lens of a certain numerical aperture is determined with Abbe's equation of resolution (Equation 1) (Hell *et al.,* 2009; Zhuang, 2009).

$$\text{Abbe Resolution} = \frac{\lambda}{2\text{NA}} = \frac{\lambda}{2n\sin\theta} \quad \text{(Equation 1)}$$

Considering green light of 500nm wavelength (Lambda - λ) passing through an objective lens with a numerical aperture (NA) of 1, the resulting sample resolution would be ≥ 250nm (0.25µm). Cells can be visualized at 250nm while smaller components such as protein structures are unresolvable (Kawata, 2009 et al.; Joe et al., 2020). The resolving power of lenses in a microscope is directly influenced by the NA. The increase of the NA value signifies the increase of the amount of light collected into the objective lens during imaging hence generating sharper images with improved resolution (Piston,1998;

Sellaro *et al.,* 2013). Numerical aperture is defined by the refraction index of the medium in which the objective is working (*n*), such as immersion oil or water, and the maximal half-angle of the light cone that can enter the objective (θ) (Aoki *et al.,* 2001).

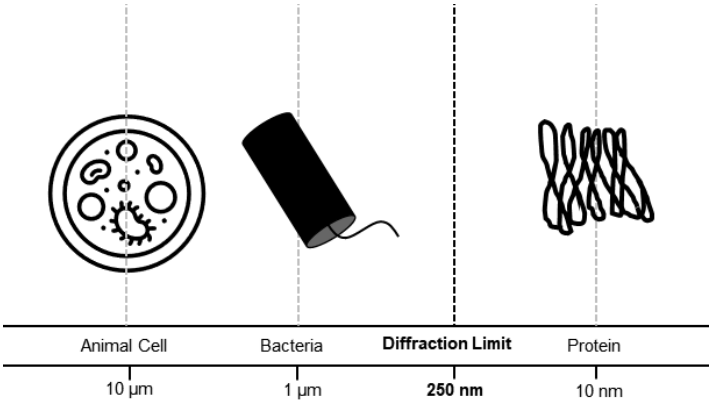


**Figure 2.1.5 Diffraction Limit.** Proteins are amongst structures that can be visualized below the diffraction limit of 250nm compared to whole bacteria or animal cells. However, it is important to note that Electron microscopes can visualize surface proteins at 100 nm but not internal structures (which is the focus of the overcoming the diffraction limit).

The resolving power of a microscope is governed by The Rayleigh Criterion based on the point spread function (PSF) (Cremer *et al.,* 2015). The Rayleigh Criterion states that two objects are resolvable at a distance ≥ than the radius of the airy disk (Verdaasdonk *et al.*, 2014; Patterson *et al.,* 2010; Tham *et al.,* 2017).An airy disk is the bright central region of an airy pattern formed by single point source of light in 3D view (also known as the PSF) depicted in Figure 2.1.6.

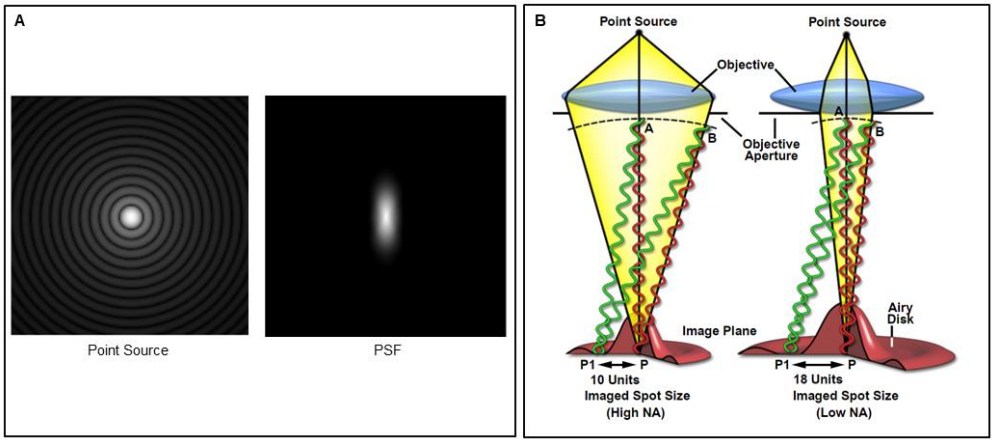


**Figure 2.1.6 Point Spread Function (A)** is a 3D representation of airy patterns seen as normal rings in lateral dimension and as elongated ellipsoid in axial dimension from a single point source of light. **(B)** The airy patterns lead to the central bright peak referred to as an airy disk. A high NA objective collects a lot of incoming light from the point source, in contrast to low NA objectives, therefore generating smaller airy disks that yield images with greater resolution. (*image adopted from: A: Bertero, 2009*; B *Nikon Microscopy*). *Image Permissions Appendix E, pg 101.*

*2.1.3.1 Extending Resolution beyond the Diffraction Limit*

The diffraction limit is applicable when certain assumptions for fluorescence microscopy are maintained, namely: i) excitation light must be uniform throughout the sample, ii) the fluorescence of a molecule depends on absorbing energy from a single photon and emitting it linearly, and iii) observations will occur in the same manner light is collected by a single objective lens. Therefore, extending resolution beyond the diffraction limit can be achieved with various microscopy modalities which do not adhere to these assumptions (Gustafsson, 1999; Huang *et al.,* 2009). These modalities include the following:

- With *Confocal Microscopy*, the use of lasers enables the excitation light to reach samples at various positions, not uniformly. The stationary laser is focused at varying positions on the sample and an image is constructed pixel by pixel. By closing the pinhole aperture to a point where out of focus light and a percentage of in-focus light is rejected, resolution can be improved beyond the diffraction limit (Sanderson *et al.,* 2016; Hovis & Heuer, 2010).
- *Multiphoton Methods* such as Two-Photon microscopy excite a single molecule with two photons (or more photons i.e. Three-photon microscopy) using high powered laser beams. The excited molecule thereafter follows normal energy emission (Mayers *et al.,* 1990). Multiphoton methodology as a non-linear microscopy technique was therefore an improvement on single photon linearized imaging. The ability of Two-photon microscopy to improve resolution greatly advanced deep tissue imaging (Helmchen & Denk, 2005).
- *4Pi confocal microscopy and* $I^nM$ improve axial resolution through the addition of more lenses that collect emission light. The newly collected signal encompasses molecule information that would otherwise be lost. 4Pi confocal microscopy and $\mathrm{I^nM}$ are the same techniques but differ with associated - confocal microscopy (4Pi) and wide-field microscopy ($\mathrm{I^nM}$) (Bewersdorf *et al.,* 2006).

The improvement of resolution by using these techniques did not, however, overcome the diffraction limit of light but lowered it to approximately 100nm (Shao *et al.,* 2008). Electron microscopy also introduced techniques such as scanning electron microscopy which provided high resolution imaging of surface structures at 100nm (Robson *et al.,* 2018). There was still a need to conquer the diffraction limit thus to study deep cellular components and protein structures. This led to the development of the ground-breaking SRM.

## 2.1.4 Super Resolution Microscopy (SRM)

SRM describes techniques that surpass the diffraction limit through Ensemble and Single molecule-based methodologies (Huang *et al.,* 2010). Ensemble techniques rely on manipulating the size of the PSF while single molecule techniques selectively activate fluorophores during imaging (Yao & Carballido, 2014; Galbraith *et al.,* 2011). The overview presented in Figure 2.1.7 described SRM techniques: Ensemble techniques comprise of Stimulated Emission Depletion (STED) Microscopy and Structured Illumination Microscopy (SIM) while Single Molecule-based techniques comprise of

Photoactivated Localized Microscopy (PALM) and Stochastic Optical Reconstruction Microscopy (STORM). The launch of SRM techniques has undoubtably started, as Werner Kühlbrandt stated, an resolution revolution (Kühlbrandt., 2014). Supporting the latter, the new era in microscopy was denoted with the recent awarding of Nobel Prizes for SRM development (2014) and cryo-EM (2017). Furthermore, the imaging industry has never experienced the high cross-disciplinary opportunities SRM has introduced noting an age of the "*holistic approach*" (Valm *et al.,* 2017; Alfieri *et al.,* 2016).

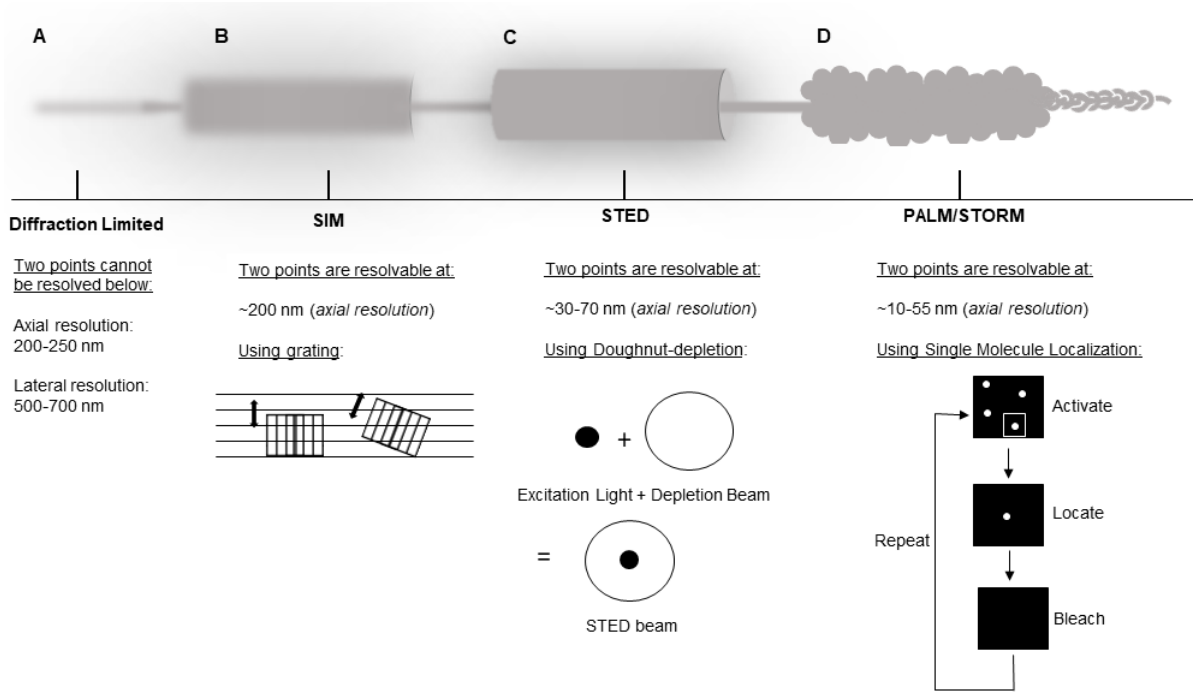


**Figure 2.1.7 SRM Synopsis. (A)** For diffraction limited samples **(B)** SIM (100 nm resolution with grating system), **(C)** STED (30-70 nm with doughnut-depletion system) or **(D)** PALM/STORM (10-55 nm with single molecule localization) can be used to improve resolution (*Adopted from Galbraith, 2011*).

### *2.1.4.1 Ensemble Techniques*

The following ensemble techniques are currently used to overcome the diffraction limit:

*Stimulated Emission Depletion (STED) Microscopy:* STED Microscopy functions similarly to a laser scanning microscope by scanning the sample with high powered lasers exciting fluorophores. However, STED follows the initial excitation with a second doughnut-shaped beam that depletes excitation everywhere except at the centre (doughnut open centre) (Otomo *et al.,* 2015). The reduced area of excitation improves specific emission detections and ultimately controls resolution due to the narrow PSFs detected that can be lowered below 100nm (Hell, 2003). The use of a stable dye such as GFP in STED assists with the photobleaching process leading to the improved temporal resolution and highest spatial resolution (Gustafsson, 2005; Gustafsson, 2000).

*Structured Illumination Microscopy (SIM):* SIM uses a grating system on the excitation laser, to create a patterned light beam that undergo interference enables the generation of various patterns and fringes

to extrapolate the original structure imaged (Heintzamann & Huser, 2017; Gustafsson, 2005). SIM as a wide-field based technique does not require special probes, so a range of conventional fluorescent probes can be used (Huang *et al,* 2010). SIM improves axial and lateral resolution by a factor of two, with ~200nm and ~100nm respectively (Gustafsson, 2000).

*2.1.4.2 Single Molecule-Based Techniques*

The following Single Molecule-Based techniques are currently being used to overcome the diffraction limit:

*Photoactivated Localized Microscopy (PALM):* The standard functioning procedure for PALM involves stimulating photoactivatable fluorescent probes randomly at low density during a time lapse acquisition, building a high-density image by combining all the frames. The probes are activated in small subsets randomly using relatively weak activating light therefore increasing the accuracy of molecule localization (Zhong, 2010). PALM and STORM probes, such as PAm-Cherry and EosFP PA, have specific requirements including obtaining high photon count, non-clustering ability, and high contrast ratio to ensure single molecule localization (Patterson & Lippincott-Schwartz, 2012; Betzig *et al.,* 2006). PALM yields high spatial resolution, up to ~10nm resolution, however this is significantly influenced by the selected fluorophore (Betzig *et al.,* 2006). Moderate to high photodamage and photobleaching is observed during PALM image acquisitions (Sydor *et al.,* 2015).

*Stochastic Optical Reconstruction Microscopy (STORM):* STORM imaging constructs a highly resolved image from photo-switchable fluorophore organic dyes, as opposed to photo-switchable fluorescent proteins in PALM. STORM utilizes several types of synthetic dyes (Alexa 488, Alexa 647, Alexa 532), and cyanine dyes (Cy5) (Godin *et al.,* 2014; Heilemann *et al.,* 2008). Probes require specific buffers with reducing properties (thiols) to function optimally, and lack thereof hinders efficient blinking and generation of resolved images (Wombacher *et al.,* 2010; Jones *et al.,* 2011). A blinking event is defined by the ability of a fluorophore to switch on and off. The on state allows fluorophores to be excited, hence emitting photons upon excitation and returning to the relaxed ground state when excitation is terminated. However, probes can enter a relatively short period of non-excitation, called the triplet state, this off-state can be extended in the presence of an appropriate redox buffer to last several minutes, which is called the dark state. During STORM microscopy fluorophores are first manipulated to turn into the dark state and then allowed to return from the dark state to the on-state by illumination with the violet laser (Nahidiazar *et al*., 2016; Ha & Tinnefed, 2012). Common buffer choices for STORM contain mercapto-ethylamine (MEA) and β-mercapto-ethanol (BME) (Cabriel *et al.,* 2019; Heilemann *et al.,* 2008). The combination of these components introduces an enzymatic oxygen scavenging system and reducing agents enabling optimal fluorophore photo-switching (Olivier, 2013; Kwakwa *et al.,* 2016). The difference between blinking and bleaching is that the latter process is irreversible, permanently switching off the fluorophore (Ha & Tinnefed, 2012).

The improved precision of molecule localization is accomplished by activating a few fluorophores within the field of view at a time, thus resolving the PSF gaussian distribution of fluorophores accurately (Rust *et al.,* 2006). STORM resolution is, therefore, influenced by the accuracy of fluorophore location and

blinking during imaging cycles, improving spatial resolution to ~10nm (Heilemann *et al.,* 2008). Accurate and quantifiable data from STORM experiments is affected by the sample preparation procedures, as well as image acquisition and processing (Metcaf et al., 2013). *Sample preparation*, such as fixative or antibody labelling, influence the overall performance of fluorophores (brightness, lifetime, photostability) (Dempsey *et al.,* 2011; van de Linde *et al.,* 2011). *Image Acquisition* is crucial in collecting bright "blinks" that are spatially separated as quick as possible for accurate localization. The optimal acquisition settings, such as exposure time and laser power, are dependent on preparation of samples and its consistency (Shroff *et al.,* 2018; Rees *et al.*, 2012). *Image Processing* and subsequent analysis methodology depends on the type of data generated during imaging. Additionally, the accurate interpretation of the generated data depends on the analysis accomplished on various software. Well-spaced blinks and overlapping blinks can be analysed with rainSTORM and deconSTORM software plugins respectively. Whereas the robust FIJI plugin, ThunderSTORM, can be utilized for a combination of low- and high-density datasets (Rees *et al.,* 2012; Mukamel *et al.,* 2012).

Taken together, sample preparation, image acquisition and processing contribute to the noise that can be detected in the generated data. The relevant steps to reduce the signal to noise ratio (SNR) varies depending on the source of the noise (Hagen *et al.,* 2015). A major contributing factor to SNR is the out of focus light emitted from the sample in regions above and below the focal plane of interest. The unwanted signal can thus be reduced with the implementation of Total Internal Reflection Fluorescence Microscopy (TIRF) during STORM acquisition. The overlay of unwanted signal reduction (TIRF) with improved PSF distribution (STORM) enhance the resolution of target structures (Almada *et al.,* 2015).

*Total Internal Reflection Fluorescence (TIRF):* TIRF is an imaging technique that removes unwanted signal through optical sectioning by exciting fluorophores within a thin region (100 nm) above the coverslip with an evanescent wave (Webb *et al.,* 2009). An evanescent wave is generated when the angle of an incident excitation light is greater than the critical angle resulting in Total Internal Reflection, meanwhile leaving a residual incident energy (evanescent field) that excites fluorophores (Fig. 2.1.8) (Mattheyses *et al.,* 2010). The evanescent field produced is attributed to the different refractive indices such as light from the immersion oil on the objectives into the aqueous sample environment. TIRF is governed by Snell's Law (Equation 2) that follows an incident beam travelling from a higher refractive index ($n_i$) into lower refractive index ($n_t$) at an angle (θ) greater than the critical angle resulting in total reflection into the first media ($n_i$) (Fish, 2015; Thompson & Lagerholm 1997).

$$n_i \mathrm{Sin}\theta_i = n_t \mathrm{Sin}\theta_t \qquad \text{(Equation 2)}$$

TIRF is categorized into Prism based TIRF and Objective based TIRF, which equally excite fluorophores within the 100nm coverslip with the fleeting evanescent wave (Axelrod, 2001). Prism based TIRF consists of a prism attached to the coverslip that allows a larger incident angle and thinner sectioning while Objective based TIRF delivers light directly on the sample and is very convenient for imaging (Vizcay-Barrena *et al.,* 2011; Mattheyses *et al.,* 2006). The evanescent wave intensity decays exponentially as it travels further than 100nm into the cell. However, near surface fluorophores are

excited sufficiently and unwanted signal is reduced due to the limited excitation (Martin-Fernandez *et al.,* 2012; Fang, 2015).

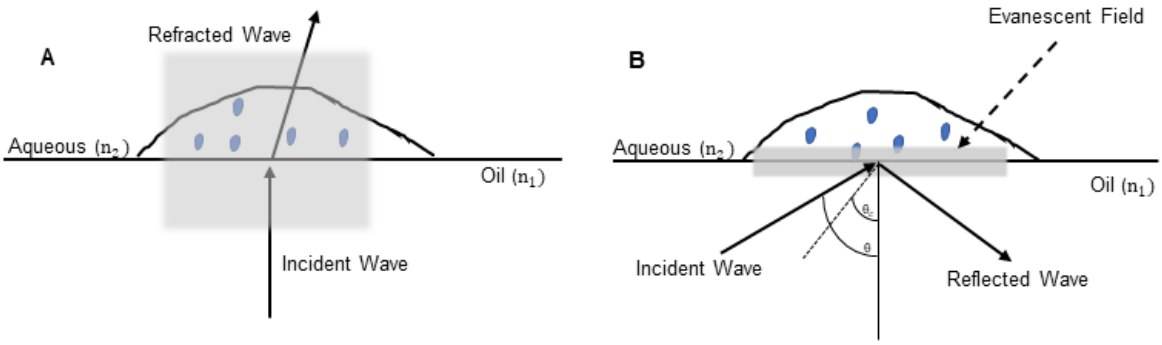


**Figure 2.1.8 Overview of the TIRF Principle. (A)** EPI illumination (standard reflected incident light in microscopy) excites the whole sample with the refracted light waves while **(B)** TIRF excites fluorophores within 100nm of the coverslip by evanescent field due to the reflected beam. Reflection is accomplished with the incident beam angle ≥ critical angle. The different refractive indices of the oil on objective lens and the sample aqueous solution enable TIRF.

Ezratty and his colleagues (2009), amongst various scientists, utilized TIRF principle to investigate cell-substrate interactions. The crucial role of clathrin in focal adhesions was investigated and established through TIRF imaging of the NIH3T3 cell lines expressing GFP-clathrin LC transfected with RFP-FAK (FAK: Focal Adhesion Kinase is a key recruited focal adhesion protein) to interact with integrin enriched cell membranes (Ezratty *et al.,* 2009). Similarly, cell membrane studies were continued with TIRF throughout the years, as with Haugh and his colleagues (2000) investigating phosphoinositide lipids' spatial distribution in plasma membrane recruitments. NIH3T3 GFP-transfected fibroblasts were excited with an evanescent field highlighting probe translocation and variations in intensity distributions in the cytoplasm and plasma membrane (Haugh *et al.,* 2000). Additionally, the mitochondria (150nm diameter) were resolved with SRM techniques highlighting clathrin-coated regions with hemispherical shapes which were previously diffraction limited. Further studies were conducted on a variety of proteins (such as synaptotagmin clusters in neuronal exocytosis) with exceptional novel results (Huang *et al.,* 2009).

The application of TIRF with or without the complementation to other techniques such as STORM revealed its usefulness in assessing cell-substrate interactions as exemplified by the above-mentioned studies.

## 2.2 PHYSIOLOGY: Cellular migration and the influence of the extracellular matrix on the assembly of focal adhesion complexes

### 2.2.1 Cellular Migration

Cellular migration is a fundamental process responsible for maintaining many functions such as embryonic development, immune defence, tissue repair and regeneration. Aberrant cell migration and signalling is observed in many pathologies such as cancer (upregulated cell migration) and/or diabetes associated impaired wound healing (impaired cell migration) (Yamada, 2019; Horwitz *et al.,* 2000; Manahan *et al.,* 2004). A better understanding of the intracellular factors and protein interactions during aberrant migration could potentially inform therapeutic strategies.

There are two main modes of cell migration: single cell migration and collective cell migration. Single cell migration is characterized by the absence of mature focal adhesions (FA) compared to collective cell migration. Cellular organisms such as amoeba demonstrate single cell migration as well as the physiological immune response of multicellular organisms using neutrophils, for instance, in single cell locomotion (Fackler & Grosse, 2008; Renkawitz *et al.,* 2019; Lammermann *et al.,* 2009; Friedl & Wolf, 2003). Collective cell migration is observed when cells, sharing mature adhesion junctions, co-ordinate their locomotion within the extracellular matrix (ECM) (Friedl, 2009). Collective cell migration is the most common mode of migration in physiology (Ghabrial & Krasnow, 2006). Epithelial cells and mesenchymal cells are an illustration of collective cell migration that occur during routine tissue repair and maintenance. Epithelial cells have mature tight junctions which perform their function of maintaining barriers. Mesenchymal cells, on the other hand, have transient junctions that assemble and dissemble constantly propelling the cells forward in response to chemotactic signals upon tissue damage (Edelblum *et al.*, 2015; Das *et al.,* 2015).

Cells junctions with neighbouring cells or the ECM are classified under five main categories namely: i) Tight Junctions, ii) Gap Junctions, iii) Desmosomes and iv) Adhesion Junctions v) Cell-ECM complexes as seen in Figure 2.2.1 (Alberts *et al.,* 2002). Tight junctions are responsible for creating a barrier between cells that is selectively permeable. These junctions are spanned with transmembrane proteins (occludin and claudin) which effectively separate apical and basal membrane domains (Nusrat *et al.,* 2005; Furuse *et al.,* 1993; Balda & Matter 2008). Gap junctions, compared to tight junctions, intentionally connect the cytoplasm of adjacent cells serving as well-defined cell-cell communication portals. The connected cells are joined by a transmembrane protein, connexin (Mese *et al.,* 2007). Desmosomes are intercellular junctions that connect with intermediate filaments from adjacent cells and are responsible for signalling, differentiation, cell strengthening and proliferation (Getsios *et al.,* 2004; Garrod & Chidgey, 2008). Similarly, Adherens junction maintain and stabilize cells and perform regulatory functions. In contrast to desmosomes, adherens junction connect adjacent cells with actin and microtubules and is found in all tissues distinct from desmosomes predominantly found in high physical stress tissues such as the heart (Harris & Tepass, 2010). Cadherin is an example of a transmembrane protein that transversely span adherens junction to sustain cell homeostasis and bring about stable cell integrity (Hartsock & Nelson, 2008; Cavey & Lecuit, 2009).

Cell-cell junctions are crucial in maintaining homeostasis; however, they do not function unaided. Cell-matrix interactions are equally important and must be considered especially in cell migration discussions. Cell-matrix interactions are elaborate multi-protein cell interactions with the ECM. The ECM is comprised of collagens or proteoglycans linking and sending signals to the cell via transmembrane proteins known as integrins. The signal housing cell-matrix complexes are referred to as focal adhesions (FA) and serve as processing and “command” centres for signals going in and out of the cell to the cell substrate (Erickson, 1990; Lock *et al.*, 2007; Geiger *et al.,* 2009).

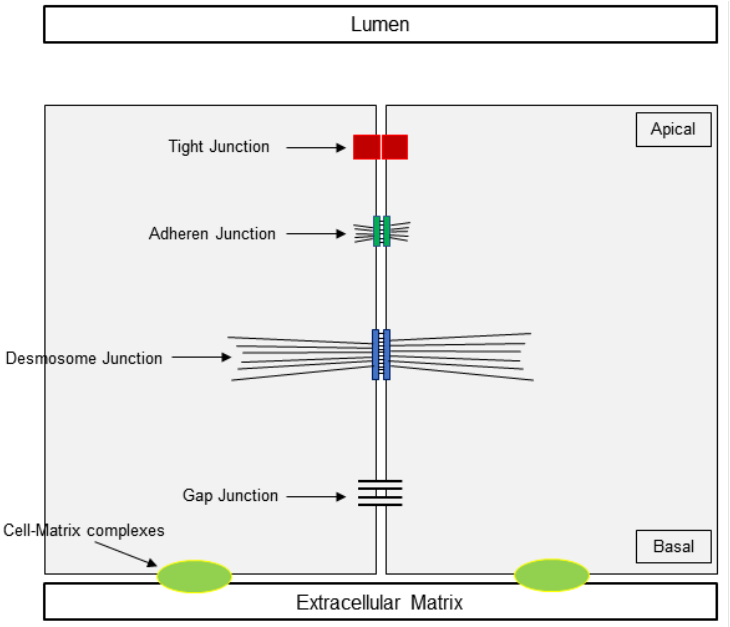


**Figure 2.2.1 Overview of Cell Junctions** between adjacent cells and the extracellular matrix. Tight Junctions seal cells together, Adherens Junction enable interaction of neighbouring cells’ cytoskeleton, Desmosomes anchor neighbouring cells to each other like adherens, Gap Junctions act as open gates for constant cell communication and molecule movements. The cell-matrix interaction or FA complexes allow adhesion with ECM through interaction with integrins.

## 2.2.2 Focal Adhesion Complexes

FA are highly organised multi-protein clustering complexes that facilitate the transfer of signals of mechanical tension between the ECM and the cell. The signalling pathways are dependent on the presence of integrin physically connecting the ECM and cell (Burridge, 2017; Hood & Cheresh, 2002). There are several types of adhesions at integrin sites namely: focal complexes, fibrillar adhesions and focal adhesions. Focal complexes are short lived, small complexes that initiate stabilization in cell edges and that mature into stable focal adhesions while fibrillar adhesions are observed in ECM remodelling

(Kuo, 2011; Pasapera *et al.,* 2010; Ilic *et al.,* 2004). The integrin-based FA are constantly associating and dissociating (FA turnover) to mediate cell migration (Wegener *et al.,* 2007; Kim *et al.,* 2003). Various adhesion proteins are recruited into these integrin-based FA to form the functional complexes responsible for cellular migration. The formation of FA complexes has been a topic of debate throughout the decades, with different pathways implicated in the multi-protein recruitment course (Lawson *et al.,* 2012).

The Integrin transmembrane protein anchors the cell to the ECM, thereby facilitating signal transduction between the ECM and the cell. Integrin consists of non-covalently bound alpha and beta subunits and varying ligands. While still not fully understood, the latter greatly affect the recruited proteins within the FA complex, as well as the elicited responses (Alberts *et al.,* 2002). One of the most well-known integrin-based FA recruitment pathways is mediated by Focal Adhesion Kinase (FAK) (Zhao & Guan, 2011). FAK was noted to be an integrin-depended tyrosine phosphorylated protein prominently located in FA complexes (Schaller *et al.*, 1992). In the cytoplasm, FAK exist in an inactive form but becomes activated when near integrin-β (Schaller *et al.,* 1995). The FAK conformational change enables the binding of other components such as the non-receptor receptor tyrosine kinase Src complex. Src-FAK complex phosphorylates p130cas (docking protein coordinating kinase signalling in cell migration) and further enlists key adapter proteins such as paxillin (crucial transduction protein in ECM-Cell signalling for adhesion) during cell migration (Klemke *et al.,* 1998; Cary *et al.,* 1996; Cary *et al.,* 1998). Another observed pathway for cell migration mediated by integrin-FAK, recruit phosphatidylinositol 3-kinase (PI3K) and additional signalling intermediates (e.g., Growth factor receptor-bound *protein*-2 (Grb2)) further stimulating cell migration with the addition of Rac proteins (subset of Rho GTPase signalling proteins) (Han & Guan, 1999; Parson *et al.,* 2000; Mitra *et al.,* 2005). While the integrin-FAK Rho protein recruitment into the pathway shows inconsistent results for cell migration (Ren *et al.,* 2000; Chen *et al.,* 2002). The above-listed integrin-FAK mediated protein recruitments provide a window into the complex FA assembling mechanisms. Furthermore, talin and vinculin mediated pathways perform essential roles in migration signalling and are the most likely candidates to form linkages between integrin and actin (Huttenlocher & Horwitz, 2011). The subsequently talin and vinculin will be discussed in detail focusing on the specific roles during cell migration.

*2.2.2.1 Talin*

The talin homodimer is an adhesion protein with binding sites for FA proteins including integrin and actin. Talin exists in a closed confirmation in the cytoplasm and can switch to an open conformation upon protein binding (Klapholz & Brown, 2017; Molony & Burridge, 1985). Although the equilibrium of the closed and open conformation is unclear, it is known that the addition of ligands such as phosphoinositide (PIP2: regulate several actin binding proteins) activate talin by stimulating its transition to an open conformation (Martel, 2001; Schramp *et al.,* 2012). Talin recruitment to integrin regions is independent on its conformation. Both configurations can be enlisted in FA regions with the closed talin form directly activated by integrins while the activated open talin form undergoes further conformational changes) (Klapholz & Brown, 2017). Talin binding to integrins depends on the binding site and can

result in a perpendicular or parallel binding (Wang *et al.,* 2011). Protein binding changes conformation so that integrins progress from closed to extended states and eventually open states that will subsequently bind ECM ligands (Anthis *et al.,* 2009; Goult *et al.,* 2010). Talin-Integrin dimers jumpstart the activation of adjacent integrins. Actin filaments consequently bind talin and the establishment of this network facilitate signal transmission in and out of the cell (Shattil *et al.,* 2010; Kim et al., 2011). Figure 2.2.2 outlines the basic talin mediated FA pathway. Additional adapter proteins have also been noted to support the talin-integrin established network. The previously mentioned Src-FAK complex encourages the binding of PIPK1γ90 to talin and together with Calpain 2 escalates the complex translocation to the plasma membrane (Zaidel-Bar *et al.,* 2007; Franco *et al.,* 2004).

The role of talin in migration has been investigated in several studies. From multi-cellular organisms to *in vitro* settings MSCs talin has been found to heavily influence cell migration. Cram and colleagues in 2003 used nematode (*C. elegans*) strains with a GFP tagged talin sequence to investigate the effect of talin knock-out. Real time reverse transcription polymerase chain reaction (RT-PCR) and fluorescent microscopy analysis of talin deficient groups revealed defects in migration, causing inappropriate turns and abrupt stops in counted L4 hermaphrodites migration (Cram *et al.,* 2003). On the opposite side of the spectrum, talin defects in undifferentiated embryonic stem cells resulted in slower migration due to the disrupted cell adhesion complexes and cytoskeletal structures. Interestingly, fibroblasts derived from a talin defective cell line adhered normally due to a secondary closely related talin gene being activated. However, the transfection of talin-GFP into talin null fibroblasts nullified the secondary talin gene effects (Zhang *et al.*, 2008; Priddle *et al.,* 1998). Talin was concluded to be critical in adhesion formation and subsequent cell migration in contrast to vinculin which was seen as an adhesion strengthening adapter proteins (Xu *et al.*, 1998). Regardless, the multi-protein assembly of FA complexes allowed the unfolding of various talin domains and hence additional binding of proteins such as vinculin in support of migration (Gingras *et al.*, 2005; Atherton *et al.,* 2015).

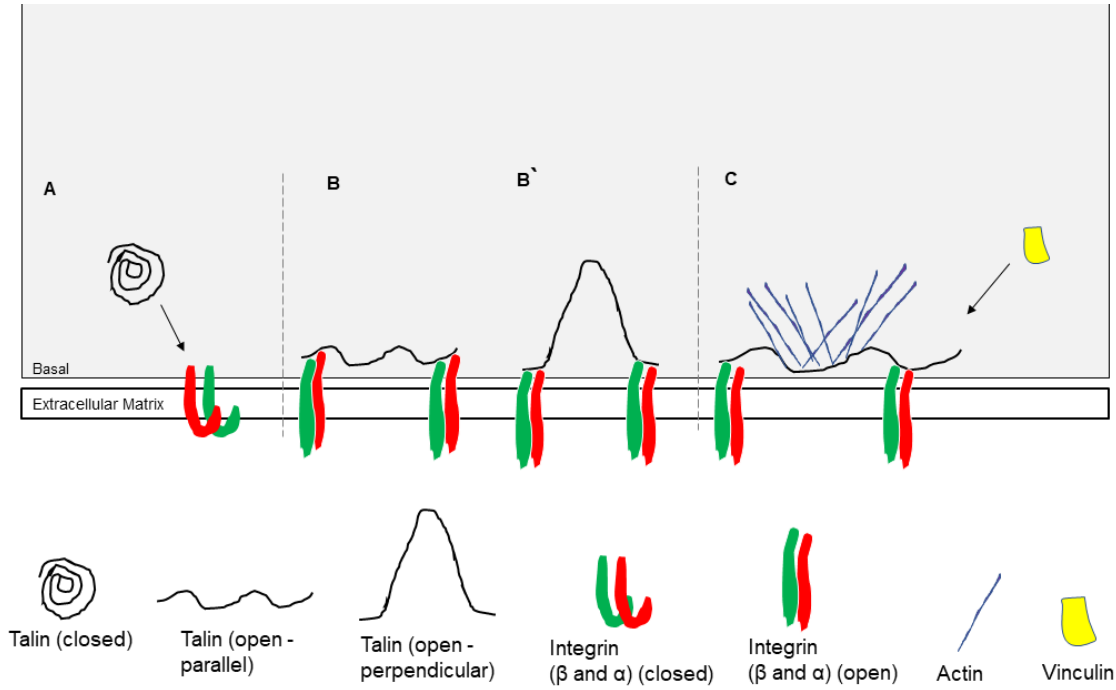


**Figure 2.2.2 Talin mediation in Focal Adhesion Complex. (A)** Talin is recruited to integrin and opens conformation. **(B)** Both talin and integrin change conformation to active states, with talin existing in either parallel or perpendicular open configurations. **(C)** In the open conformation Talin offers binding sites for actin filaments and additional adhesion proteins as required such as vinculin.

*2.2.2.2 Vinculin*

Vinculin is a cytoplasm-based protein that has been noted as a key protein in mechano-sensing. FA, as they act as connecting ducts, change shape and size in response to mechanical stimuli whether from the substrate or any external force (Galbraith *et al.,* 2002; Balaban, 2001). The protein is composed of two domains, the Vinculin head (Vh) and Vinculin tail (Vt) connected by a flexible belt (Galbraith *et al.,* 2002). Vinculin has a variety of binding partners to the different vinculin domains (Goldman, 2016). The binding partners depend on the mechanical impulse detected through the integrin-talin complex from the ECM substrate (Humphries *et al.,* 2009).

There are a host of hypothesized pathways for vinculin recruitment in FA. Figure 2.2.3 presents the largely accepted theory, but some aspects such as the relevance of recruiting adhesion proteins in a certain order, are still unclear. Nonetheless, vinculin portrays a combinatorial activation into FA complexes (Goldman, 2016). Vinculin exists in a constant flux between its open and closed conformation within the cytoplasm through phosphorylation- and dephosphorylation events that do not influence FA induced activation (Bakolitsa *et al.,* 1999; Janssen *et al.,* 2006; Goljiet *et al.,* 2012). Chen in the 2006 publication noted the strong forces between Vh and Vt domains could not be overcome by a single ligand binding to vinculin hence a combinatorial approach to vinculin activation. Therefore, vinculin binds talin and actin as the base activation points within the FA complexes, with talin binding to the Vh and actin binding Vt (Grashoff *et al.,* 2010; Janoštiak *et al.,* 2014; Pasapera *et al.,* 2010). Once vinculin is activated and exists in an open conformation, recruiting a plethora of key adhesion

proteins such as paxillin. Depending on the intensity of the ECM stimuli other adhesion proteins are recruited through vinculin binding to FA complexes: stronger stimuli encourage the recruitment of additional adhesion proteins and henceforth formation of stronger FA (Zamir & Geiger, 2001; Ziegler *et al.,* 2006).

Unmistakeably FA complexes comprises of a dense network of proteins such as paxillin, actin, vasodilator-stimulated phosphoprotein (VASP: assists in cytoskeleton remodelling as actin regulatory proteins), PIP2 and others. However, for the purposes of this research study *ECM-integrin-talin-vinculin* link were of interest. Xu *et al.,* (1998) noted vinculin deficient embryonic stem cells contributed to heart and brain defects in mice upon recombinant vector transfection. Irregular migration patterns and FA assembly was evident in vinculin deficient cells (Xu *et al.,* 1998). The continued examination of vinculin null cells indicated a dysregulation in myosin dependent traction and adhesion forces, while intriguingly vinculin was not necessary for the communication of adhesive and traction forces (Dumbauld *et al.,* 2013). Traction forces describes the strength of the cell propulsion influenced by FA proteins, as observed with vinculin modifications in cells (Goldmann 2002; Alenghat *et al.,* 2000).

FA size increased as substrate stiffness or ECM rigidity increased, because of elevated adhesion proteins recruitments. The generated traction force was therefore greatly increased with substrate stiffness. The alterations in FA complexes, or adhesion proteins assembly, was therefore proposed to respond mechanical stimuli resulting from ECM rigidity (Stutchbury *et al.,* 2017; Han *et al.,* 2012; Pelham & Wang, 1997).

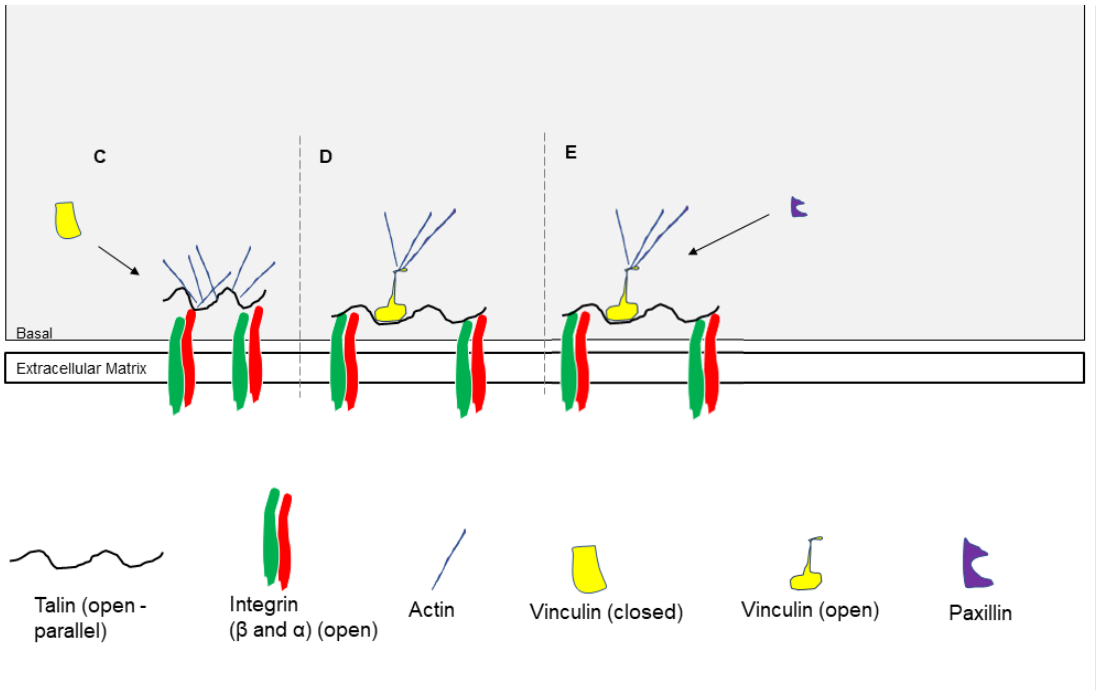


**Figure 2.2.3 Vinculin recruitment and function in a Focal Adhesion Complex. (C)** Vinculin is recruited in an integrin-talin stable complex **(D)** and binds to talin and actin, activating vinculin into open conformation. **(E)** Additional adhesion proteins such as paxillin assisting in strengthening the FA complex are added on the vinculin

## 2.2.3 Substrate Stiffness: The effect of ECM rigidity on cellular dynamics

### *2.2.3.1 Collagen in ECM*

Cell growth, migration and differentiation have been observed to be influenced by molecules introduced into the system eliciting a specific response or signalling in cell-cell connections. However, the ECM environment plays an equally important role in the aforementioned processes (Yue, 2014; Cox & Erler, 2011; Kular *et al.,* 2014). Recently it has been confirmed that mechanical forces generated from the substrate elasticity plays a vital role in cell adhesion, growth, and survival (Discher *et al.,* 2005; Maitre & Heisenberg, 2011). The phenotype of dendritic cells was altered with an increase in the substrate stiffness (Mennens *et al.,* 2017). The significance of ECM elasticity led to the development of synthetic substrates used in conjunction with natural substrates. Synthetic modulations of substrates can be achieved through chemical processes or ECM protein density manipulation as observed in gels such as fibril and Type I Collagen (Liu *et al.,* 2017; Trappmann & Chen, 2014). Collagen is the largest class of protein found in mammals, making up most of the ECM that ultimately maintains homeostasis (Mouw *et al.,* 2014). Several forms of collagen are available, specific for certain tissues with a set role in cell adhesion. All collagen types have the well-known triple helix structure of homo and hetero trimers (Richard-Blum, 2011). Due to the stable bioactivity of collagen and abundance in major tissues of the body, collagen has been widely used in tissue engineering and 3D cell models (Chattopadhyay & Raines, 2014). The introduction of collagen in cell culture protects cells from stress and increases cell survival while maintaining optimal cell growth and migration (Somaiah *et al.,* 2015).

### *2.2.3.2 Ascorbic acid 2-phosphate in ECM*

Ascorbic acid (AA), also known as Vitamin C, acts as a cofactor responsible for collagen biosynthesis and involves three enzymes: prolyl-3-hydroxylases (P3H), prolyl-4-hydroxylases (P4H) and lysyl hydroxylases (LH) (Linster & Schaftingen, 2007; Pinnell, 1985). However, AA is highly unstable in cell culture conditions (pH = 7; Temperature = 37°C) (Padayatty & Levine, 2016). Ascorbic acid 2-phosphate (AAP) is a stable derivative of AA and is therefore utilized as a supplement instead of AA (Hata & Senoo, 1989; Fermor *et al.,* 1998). AAP is a glucoside AA derivation amongst lipophilic AA derivations, conjugates of vitamins and butanolide AA derivations (Mecan *et al.,* 2019). *In vitro* collagen biosynthesis and collagen lattice contraction models indicated an influence by AAP. AAP inhibits the breakdown of the key enzymes (LH, P3H and P4H) responsible for collagen hydroxylation (important for collagen helical structure formation) thus increasing collagen production and lattice contractions (Boyera *et al.*, 1998).

The extended effects of AAP in cell culture varies depending on cell density and AAP concentration in a dose-dependent manner (Wu *et al.,* 2020). Takamizawa et al. (2004) used human osteoblast-like MG-63 cells to investigate the effect of AAP concentrations (0.25mM to 1mM) on proliferation and differentiation. Cells were cultured for 3 days in media with and without AAP at various concentrations. Significant cell growth (proliferation) was observed in all AAP treatments (0.25mM to 1mM) and encouraged collagen synthesis and maturation. Table 2 lists additional AAP outcomes conducted on various studies.

*2.2.3.3 ECM rigidity mechanical stimuli on cells*

A change in collagen synthesis influences key regulated cell processes such as cell migration due to ECM remodelling, that in turn contributes to developed migratory pathologies when ECM remodelling is dysregulated (Bonnans *et al.,* 2014). Cell migration models based on collagen deposition have been constructed and indicated that collagen deposition in ECM characterized migration patterns (Wolf & Friedl, 2009). The external mechanical stimuli utilized three components to elicit a response: substrates, sensors, and effectors. Substrates are ECM constituents (proteins, glycoproteins, and proteoglycans), sensors are key signalling proteins such as integrins and effectors are whole functioning cells such as fibroblasts synthesizing ECM components under high tensile stress conditions increasing traction forces (Humphrey, 2015). The induced stress of the ECM stimulates FA complexes formation to alleviate the strain and maintain homeostasis. The actin cytoskeleton and FA accessory proteins remodel to accommodate ECM changes (Webster *et al.,* 2014; Yoshigi *et al.,* 2005). The magnitude and frequency of the detected strain/stress will determine the type of elicited response, also depending on cell type (Jungbauer *et al.,* 2008).

Therefore, the research study at hand aims to investigate the influence of ECM stiffness, due to AAP supplementation, on FA expressed proteins (talin, vinculin and integrin-β1) in migrating cells. The application of STORM/TIRF in the analysis of talin, vinculin and integrin-β1 will reveal previously illusive information on 1) Protein distribution (at FA sites: actual colocalization or co-occurrence) and 2) Resolved protein locations and binding sites. The reduced unwanted background signal (TIRF) with improved PSF detections (STORM) enable pinpoint of molecule information such as molecule location and intensity in relation to conventional microscopy (such as confocal microscopy).

Table 2: Additional AAP effects as reported in various publications.

| Study ID | Antioxidant | Concentration | Cell Type | Outcome | Mechanism |
|---|---|---|---|---|---|
| Choi et al., 2008 | Ascorbic acid 2-phosphate | 0.01-0.5mM | Mesenchymal stem cells (MSCs) | AAP increase proliferation (with highest proliferation rate at 0.25mM) | AAP increased collagen synthesis, calcium (at 50mM) and oil deposition (at ≥250mM) enhancing MSCs |
| Mekala et al., 2013 | Ascorbic acid 2-phosphate | 0.05 -0.5mM | Human umbilical cord blood-derived stem cells (hUCB-SCs) | AAP significantly increase osteogenic differentiation at 0.05mM. In contrast: AAP at 0.25mM and higher yielded significant adipogenic differentiation. | AAP effect is dose dependent. Created a model evaluating factors leading to differentiation. |
| Sun et al., 2013 | Ascorbic acid 2-phosphate | 0.2mM | Adipose-derived stem cells (ADSCs) | Antioxidants in ADSCs culturing media showed significant increase in proliferation | CDK (cyclin dependent kinase inhibitors) downregulated by antioxidant regulating cells entering S1 phase |
| Wang et al., 2016 | Ascorbic acid 2-phosphate | 0.2mM | Human ADSCs | Antioxidant resulted in reduced apoptotic events and less caspase-3 levels | Antioxidants reduce ROS generation and therefore apoptosis |
| Yu et al., 2014 | Ascorbic acid 2-phosphate | 0.25mM | ADSCs | Increased proliferation and differentiation and maintained cellular stemness | Antioxidant additions assists in ADSCs expression of stemness proteins |

# Chapter 3: Aims and Objectives

It is hypothesized that there is a change in the expression patterns of talin, vinculin and integrin-β1 during cellular migration and that this is affected by collagen deposition within the ECM. The hypothesis was tested whilst establishing and optimizing TIRF and STORM microscopy techniques.

**Aim 1:** Determine the highest non-toxic AAP concentration that will maintain MSCs viability to a similar extent as the standard control culture condition.

**Objectives:**

1.1 Conduct a dose response using varying AAP concentrations (2.4mM, 1.2mM, 0.6mM, 0.3mM and 0.15mM) over 24hours (h), 48h and 6 days, respectively.

1.2 Assess cell viability over time in the various treatment conditions using Crystal Violet Staining.

**Aim 2:** Determine the migration rate of MSCs over time and identify the ideal time point where pseudopodia are clearly visible.

**Objectives:**

2.1 Conduct live cell migration studies using the Ibidi 2 well-insert $\mu\text{-Dish}^{35\text{ mm, high}}$ to determine if AAP treatment affects the migration rate of MSCs compared with standard culture conditions over a period of 24h.

2.2 Assess whether cellular proliferation is occurring concurrently over the 24h time period by adding mitomycin C (Mit. C) to the migrating cells within each treatment condition.

2.3 Use image analysis to identify the optimum time point of migration where pseudopodia are clearly visible.

**Aim 3:** Optimize the ICC staining protocol whilst investigating protein distributions and interactions.

**Objectives:**

3.1 Determine the most appropriate fixative (methanol vs paraformaldehyde) and the optimum time period required for fixing of cells.

3.2 Perform antibody titrations on primary and secondary antibodies to determine the optimal concentration/dilutions and test the fluorescent mounting media.

3.3 Perform migration assays in media with and without optimized AAP (*aim 1*) at the defined time point where pseudopodia are clearly visible (*aim 2*) and stain the cells using the optimized ICC protocol (*aim 3, objective 3.1*).

3.4 Use multi-colour confocal microscopy to quantify the expression of the adhesion proteins (talin, integrin-β1, vinculin) and the possible interaction between these proteins through co-localisation analysis.

3.5 Identify one of the expressed proteins preferably with defined FA/filament structure for further investigation using STORM and TIRF.

**Aim 4:** Optimize STORM and TIRF techniques whilst investigating a specific adhesion protein.

**Objectives:**

4.1 Optimize STORM and TIRF microscope settings for image acquisition.

4.2 Use the optimised microscope settings to investigate the adhesion protein of interest using STORM and TIRF in migrating and non-migrating cells with and without AAP treatment and quantify shape changes in the FA based on expression patterns of the selected adhesion protein at the level of attachment.

# Chapter 4: Materials and Methods

## 4.1. Cell Culture: Expansion of Cell Number

All experiments for this research project were conducted using a mesenchymal stem cell line (MSCs) (C3H/10T1/2, Clone 8; ATCC®CCL-226) that falls under level 1 of the biosafety regulations and thus received exemption from ethical clearance (BEE-2020-1604E) *(Appendix A, pg 93)*

MSCs were stored in cryovials (CRYO.S, Greiner Bio-One, Germany), preserved in liquid nitrogen, with the cell integrity maintained using freezing media. Freezing media consisted of 5% dimethyl sulfoxide (DMSO) (Sigma-Aldrich, USA), high glucose (4.5g/L) Dulbecco's Modified Eagle Medium (DMEM) with ultra-glutamine (Lonza BioWhittaker, Belgium), 1% penicillin-streptomycin (PenStrep) (Lonza BioWhittaker, Belgium) and 10% foetal bovine serum (FBS) (Biochrom, Berlin, Germany).

MSCs (passage 9 - 12) were thawed in a 37˚C water bath and seeded at a density of 5 000 cells/$cm^2$ in culture dish with a growth area of 55 $cm^2$ (Nest Biotechnology, China). Cells were maintained in standard growth media (SGM) at 37˚C, 5% $CO_2$ and 90% humidified air, under sterile cell culture conditions. SGM consisted of high glucose (4.5g/L) DMEM with ultra-glutamine (Lonza BioWhittaker, Belgium), 1% PenStrep (Lonza BioWhittaker, Belgium) and 10% FBS (Biochrom, Berlin, Germany). Growth media was changed every 3 days until cells reached ≥ 80% confluence. Refer to Fig. 4.1.1 for representative images of MSCs growth over time.

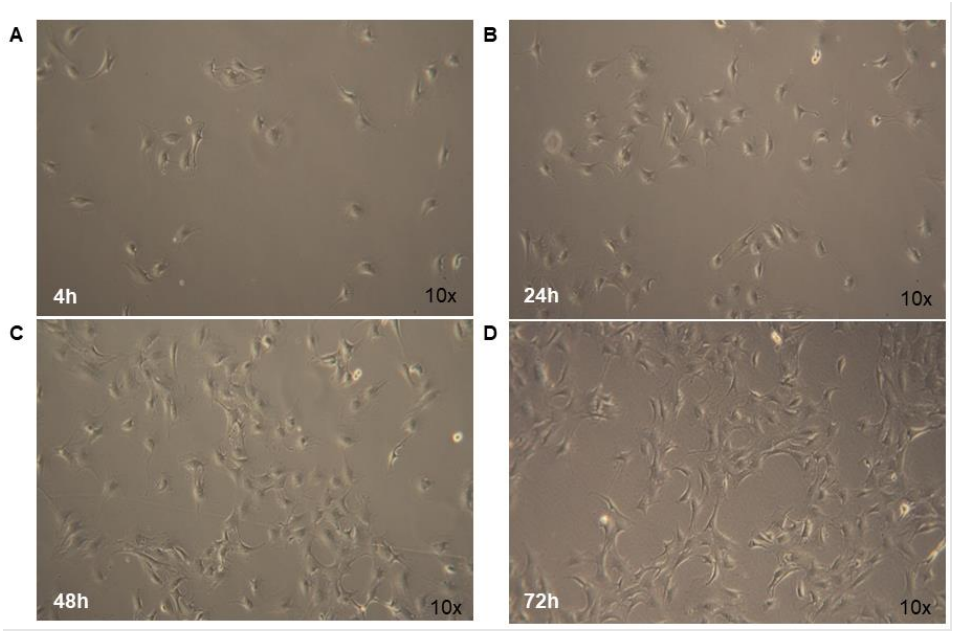


Figure 4.1.1 C3H/10T1/2 Cell Confluency over Time in standard culture conditions at (A) 4h (B) 24h (C) 48h and (D) 72h post seeding. Images were taken with a Light Microscope at 10x/0.25NA objectives (Primovert Microscope, Zeiss) (Camera: Canon EOS 650D).

At ≥ 80% confluence SGM was aspirated and pre-warmed phosphate buffered saline (PBS) was used to wash cells. PBS consisted of 8g NaCl, 0.2g KCl, 1.44g $Na_2HPO_4$ and 0.24g $KH_2HPO_4$ made up to a final volume of 1L with $dH_20$ and pH deviations adjusted with HCl to pH7.4. After PBS was discarded, adherent cells were detached from the culturing dish by addition of 1ml pre-warmed 0.05% w/v Trypsin (200 mg/L Versene EDTA, Lonza, Belgium) and gentle tapping/swirling motions on the dish for 3-5 minutes (min). This was followed by the addition of 2ml SGM to the dish to quench Trypsin enzymatic activity. The resulting cell suspension was centrifuged (Centrifuge 5804, Eppendorf) in 15 ml centrifuge tubes (WhiteSci, USA) at a relative centrifugal force of 179 *g* for 5 min to pellet cells. The supernatant was discarded, and cells were resuspended with 1ml SGM. The number of viable cells in the cell suspension was determined using a haemocytometer chamber (Fuchs-Rosenthal, Western Germany) with the counting grid shown in Fig. 4.1.2. Trypan blue (Invitrogen, Thermo Fisher Scientific) was added in 1:1 dilution with cell suspension to distinguish between viable and non-viable cells during cell counting. Trypan blue exclusion test stains dead cells by passing through the porous cell membrane and binding proteins therefore rendering the dead cell dark blue.

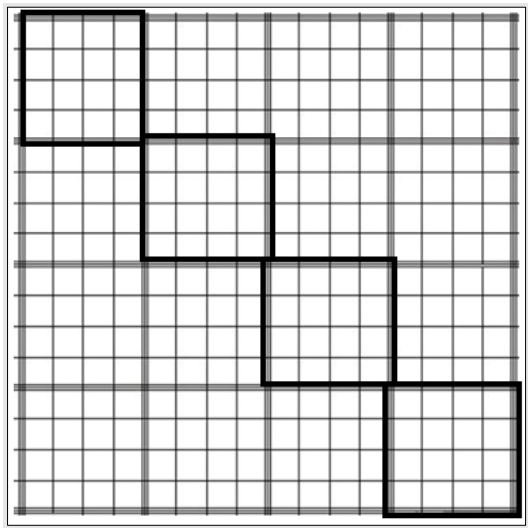

**Figure 4.1.2 Haemocytometer Counting Grid.** The highlighted squares represented the areas used for cell counting.

The formula below was used to calculate the total number of viable cells/ml:

$$\text{Total number of viable cells in 1ml} = \text{Total number of cells counted x } \frac{\text{dilution factor}}{\text{\# of Squares}} \text{ x 10 000 cells/ml.}$$

The cells were either sub-cultured to further expand cell numbers or plated for other experimental purposes. A seeding density of 5 000 viable cells/$cm^2$ was maintained throughout the study; the quantity of seeded cells for subsequent experiments depended on specific experimental design requirements such as type of cell culture dish utilized as indicated in table 3.

The flow diagram in Figure 4.1.3 provides an overview of the study design and experimental procedures for the study in chronological order.

Table 3: Cell seeding densities according to growth areas.

| Cell Culture Plate | Growth Area | Volume of total content | *Seeding Density |
|---|---|---|---|
| 10 cm Dish | 55 $cm^2$ | 10 ml | 5 000 cells/$cm^2$ |
| 96 well plate | 0.3 $cm^2$ | 0.1 ml | 1 500 cells/$cm^2$ |
| 8 well plate | 0.8 $cm^2$ | 0.4 ml | 4 000 cells/$cm^2$ |
| 2 well insert | 0.22 $cm^2$ | 0.07 ml | 1 100 cells/$cm^2$ |

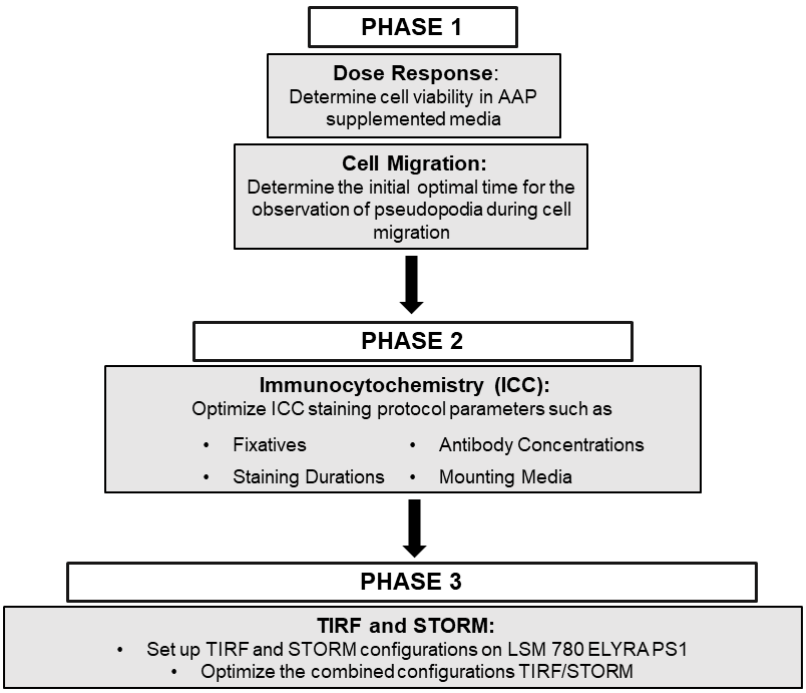


**Figure 4.1.3 Study Design Outline: PHASE 1** Various AAP concentrations were tested to determine the highest non-toxic dosage to add in standard growth media (SGM). Subsequently, live cell imaging was used in different treatment groups (SGM and AAP treated media) to determine the ideal cell migration time for visualising pseudopodia. **PHASE 2** Sample preparation was optimized in the immunofluorescence staining procedure for an improved and effective antibody staining for imaging. **PHASE 3** TIRF and STORM configurations were optimized on LSM 780 ELYRA PS1 microscope whilst investigating an adhesion protein (talin) in migrating MSCs.

## 4.2. Dose Response: Determination optimal AAP concentration that maintains cell viability.

The highest non-toxic concentration of AAP, that will not negatively affect cell viability, was determined with a dose response experiment. Cell viability in AAP supplemented media was assessed using crystal violet staining (hexamethyl pararosaniline chloride) that binds proteins and DNA of viable adherent cells. As dead cells are not adherent and are usually washed off during the staining procedure, only the remaining viable cells will be stained. The assay is quick and versatile, while it is also insensitive to metabolic changes. Fig. 4.2.1 details the experimental design for determining the optimal AAP supplementation in media.

A total of 1 600 cells/well was the optimized cell number for seeding in 96 well plates. Following seeding, cells were incubated at 37˚C, 5% $CO_2$ and 90% humidity in SGM for ± 5h to allow cellular adhesion. Subsequently, SGM was removed from wells (except control group wells) and substituted with varying AAP supplemented media concentrations (0.15mM, 0.3mM, 0.6mM, 1.2mM and 2.4mM) (Sigma-Aldrich, Germany) for 24h, 48h and 6 days. The serial dilution of AAP stock solution (480mM) is depicted in Fig. 4.2.1 indicating a consecutive 1:1 dilution of the treatment groups resulting from the initial 100x dilution of stock AAP and SGM.

Cell media was removed at the end of each incubation period (24h, 48h, 6days) and the cells washed with PBS then fixed for 30seconds (sec) with 150µL ice cold methanol (Sigma-Aldrich, Merck chemicals (Pty) Ltd., RSAUS). Staining was achieved with 0.01% Crystal violet solution (Sigma-Aldrich, Germany) incubated for 5min and washed twice with PBS before imaging. Pertaining to the 6day time point, cell media was refreshed on day 3 with the applicable AAP concentration. The dose response was conducted with biological (N=3) and technical (n=3) repeats.

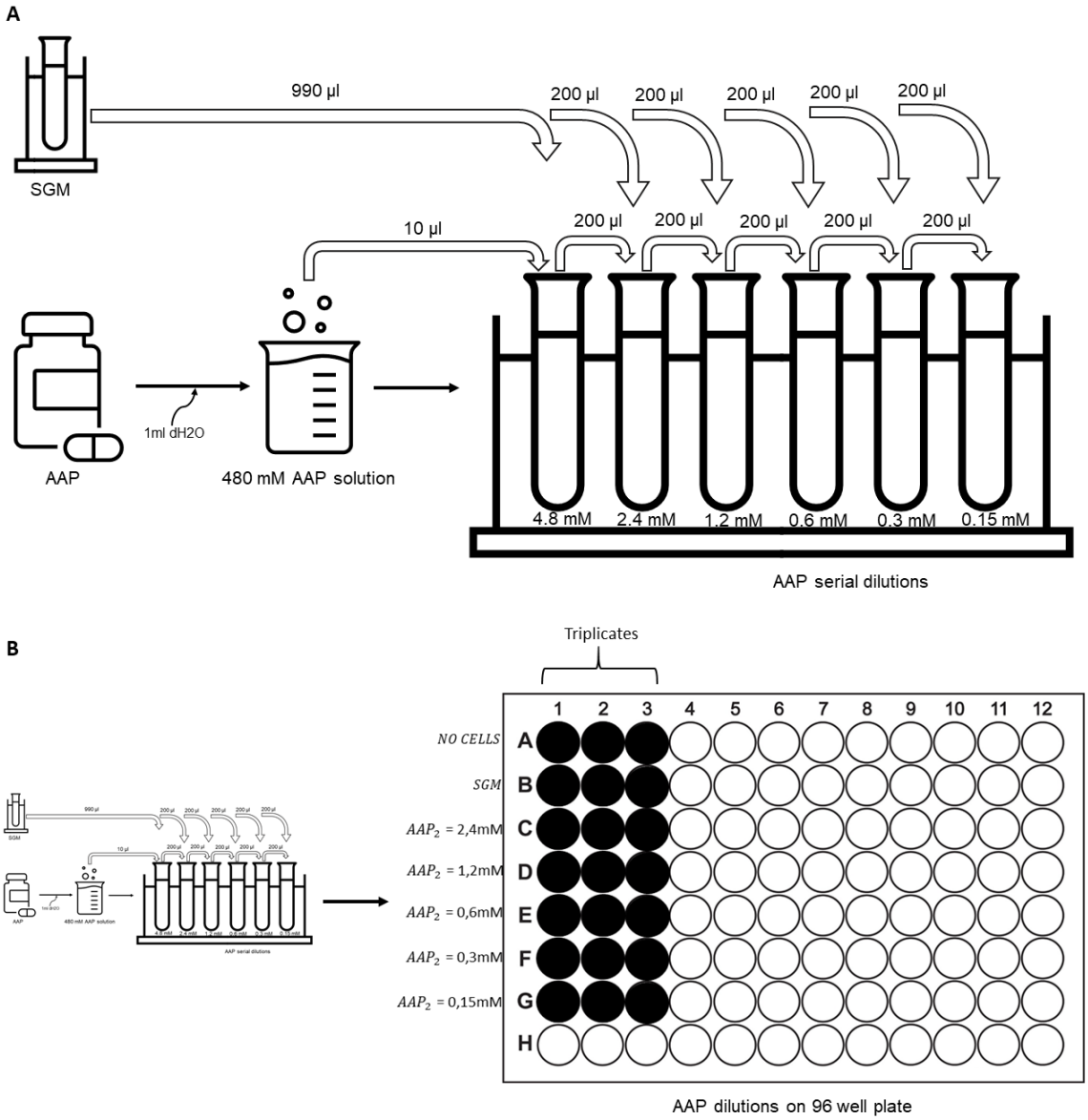


**Figure 4.2.1 AAP Dose Response on 96 well plate. (A)** AAP serial dilution: 10µl (480mM) stock AAP was diluted with 990µl SGM creating 1ml (4.80mM) AAP solution. Thereafter AAP was diluted at a ratio of 1:1 with SGM yielding final concentrations of 2.4mM, 1.2mM, 0.6mM, 0.3mM and 0.15mM. **(B)** Cells were incubated with and without varying AAP concentrations in triplicate wells for 24h, 48h and 6 days, respectively. The experiment was repeated 3 times (n=3).

### *4.2.1 Crystal Violet Image Acquisition*

The crystal violet stained cells were imaged on the Zeiss Axio-Observer 7 Inverted Microscope with Zen 2.6 imaging software. Figure 4.2.2 depicts the image acquisition workflow: from locating and imaging cells to analysing images. Brightfield microscopy was used for imaging with: 10% illumination intensity, 10x/0.25NA objectives and Axiocam 503 (iXon Ultra 888). An advanced tile scan acquisition was setup in each well, at the same position, imaging 18 x 20 scenes per well that were eventually stitched together. Images were exported using tiff format and analysed with Fiji imaging software (ImageJ 1.52p, nih.gov, USA). The FIJI Thresholding tool was used to measure percentage surface

area of crystal violet stained cells within each well. The quantity of purple stained cells indicated the number of viable cells following incubation with the respective AAP concentrations. This was done to define the highest non-toxic AAP concentration to use in subsequent experiments. Refer to Fig. 4.2.3 for a representative image of crystal violet stained cells.

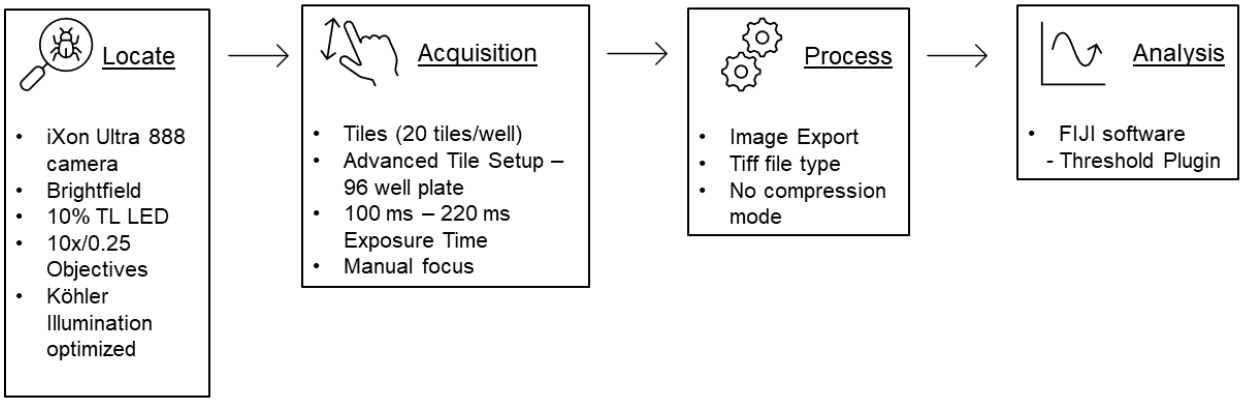


**Figure 4.2.2 Image Acquisition Workflow** for crystal violet stained acquisition in a 96 well plate determining cell viability. Cells were imaged at 10% intensity, iXon Ultra 888 (Axiocam 503) and 10x/0.25NA magnification. Tile scan images of 18 x 20 scenes in each well were acquired and stitched together for the final image. Files were saved with tiff format and processed on FIJI (ImageJ 1.52p, nih.gov, USA).


**Figure 4.2.3 Crystal Violet Staining.** Representative image illustrating viable cells in a 96 well plate following incubation with SGM cultured for 24h. Scale bar was set at 200µm.

## 4.3 Cell Migration: Determination the optimal time point for visualizing distinct pseudopodia.

Cell migration experiments were conducted using the *in vitro* Ibidi wound healing assay (µ-$\mathrm{Dish}^{35\ \mathrm{mm},\ \mathrm{high}}$ Ibidi, Germany) as portrayed in Figure 4.3.1. A cell monolayer (100% confluent) was established overnight by incubating 18 000 cells/well under standard culture conditions at 37˚C, 5% $CO_2$ and 90% humidity. Upon reaching confluence, the 2-well insert was carefully removed using sterile tweezers and the cells washed with pre-warmed PBS to remove cellular debris. Cell migration and closure of the cell free gap was monitored with cells incubated in SGM with and without optimum AAP concentration. An additional migration experiment was conducted with the introduction of Mit. C (0.1mg/mL) (Sigma-Aldrich, China) in treatment groups as control to inhibit cell proliferation during *in vitro* migration studies.

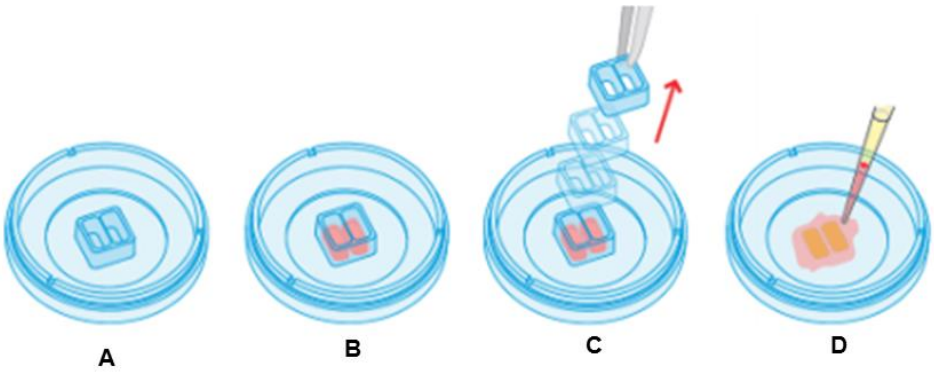


**Figure 4.3.1 Cell Migration Workflow** using the Ibidi wound healing assay µ-$\mathrm{Dish}^{35\ \mathrm{mm},\ \mathrm{high}}$ **(A)** Illustration of the Ibidi 2-well culture insert plate with **(B)** 70 µl cell suspension in each well, incubated overnight at 37˚C, 5% $CO_2$ and 90% humidity. **(C)** After cells reached confluence, the 2-well insert was removed using sterile tweezers. **(D)** After removal of the insert additional growth media (with or without AAP) was added and cell migration tracked using live cell imaging.

### *4.3.1 Live Cell Imaging*

Cell migration was tracked with continued live cell imaging over a period of 24h with a set hourly time lapse on the Zeiss Axio-Observer Microscope. A 24h live cell migration assay was performed once for each treatment group: SGM, AAP treated media, SGM with mit. c, AAP treated media with mit. c.

The microscope consisted of an on-stage incubator (Ibidi Stage Top Incubation System, Multi-Well Plates, K-Frame, CO2/O2) (Ibidi, Germany) located within the environmental chamber as seen in Fig. 4.3.2. Standard cell culture conditions (37˚C, 5% $CO_2$ and 90% humidity) were maintained: Temperature of 36.9˚C, $CO_2$ range 5% - 7% and humidity range 75% - 90%. Images were acquired with a 5x/0.15NA magnification at 15%TL LED maximum intensity. A tile scan image (1 x 5 scenes) was taken along the length of the artificial wound with an autofocus strategy.

Subsequently, the 24h time lapse was assessed on FIJI (ImageJ 1.52p, nih.gov, USA) with Freehand Tool to identify the optimal migration time point characterized with distinct, visible, and clear pseudopodia as depicted in Fig.4.3.3. Once the optimal time point was identified, the subsequent

migration assays were repeated in triplicate (N=3 and n=3) for each treatment group with images taken only at two time points: 0h – no cell migration (immediately following removal of insert) and *n*h – cell migration with prominent pseudopodia visible (optimal time point identified).

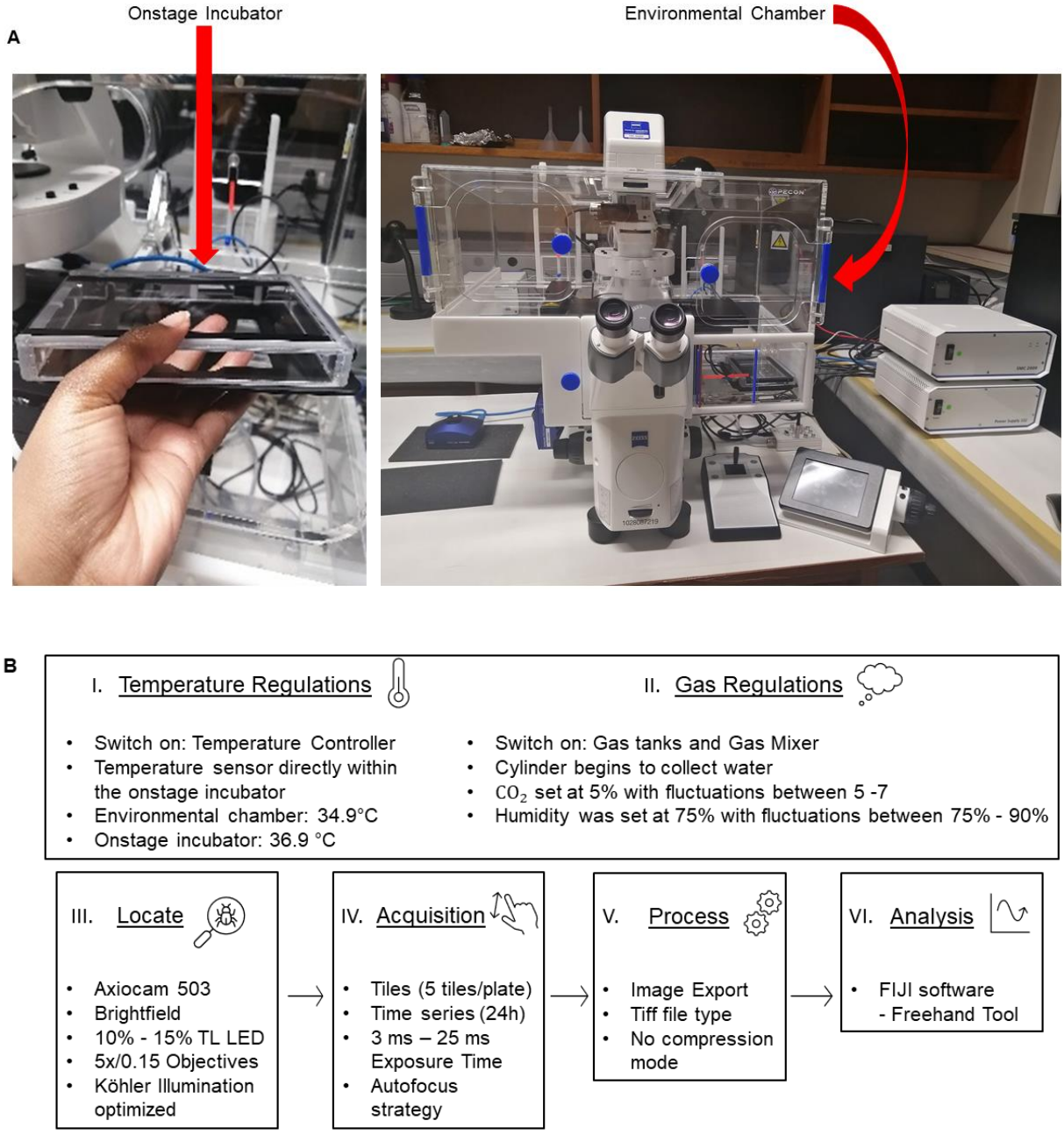


**Figure 4.3.2 Zeiss Axio-Observer Microscope Live Imaging System. (A)** Ibidi onstage incubator located within the environmental chamber to simulate and regulate incubator-like standard cell culture conditions during live cell imaging. **(B) Live Cell Imaging Workflow:** *I-II*. Temperature and Gas sensors were set within the onstage incubator with III-VI. Zen 2.6 acquisition settings set as indicated above.

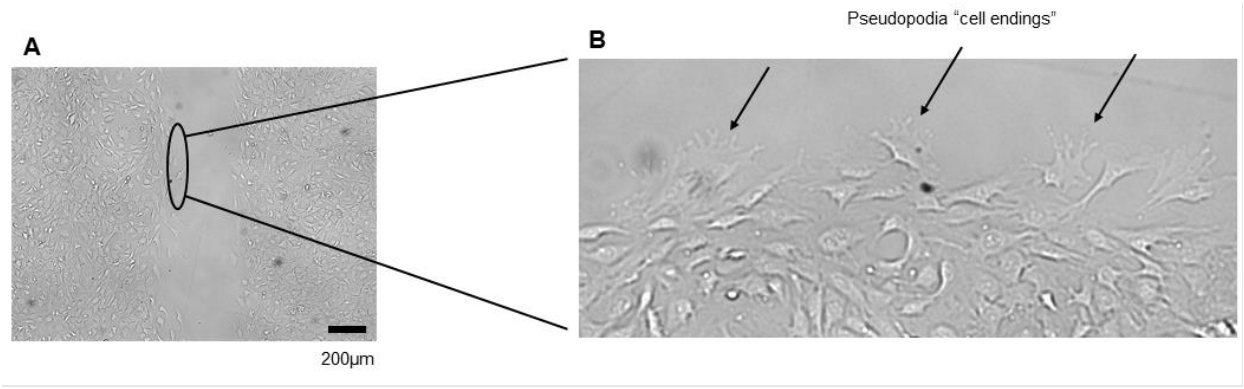


**Figure 4.3.3 Cell Migration.** Representative images illustrating **(A)** confluent monolayer of cells with the cell free gap and **(B)** prominent pseudopodia visible at higher magnification at the 8h time point in AAP supplemented media in the cell free gap. Scale was set at 200µm.

Note: To optimise the visualization of pseudopodia, techniques such as phase contrast and DIC can be compared. Since no quantification was however done using these images in the current study with only visual confirmation required for the presence or absence of pseudopodia no optimisation was performed.

*4.3.2 Quantification of Cellular Migration*

The tiff exported images were opened in FIJI software (ImageJ 1.52p, nih.gov, USA) to calculate the percentage wound closure over time (cell free gap) using the following formula:

$$\text{Wound Closure (\%)} = \frac{\text{Area 0h} - \text{Area } n\text{h}}{\text{Area 0h}} \text{ x } 100$$

Migration dynamics were further investigated using the independent software: Chemotaxis and Migration Tool (v. 2.0, Ibidi, Gräfelfing Germany). The main software configurations considered for analysis were time interval and x/y calibrations. The compressed time for the live migration videos that was taken over a period of 24h was 22 sec. The x/y calibration indicated the camera pixel size in x and y over the magnification used for imaging, $\frac{4.54\ \mu m}{5x} = 0.908 \mu m$. Directional preference was not set since migration occurred linear to close the artificial wound. To track the movement of a single cell over time, tracks were added for each frame, the centre of every cell was the selected reference point during cell tracking (centring correction – local maximum).

## 4.4 Immunocytochemistry (ICC): Optimization of the sample preparation ICC protocol.

*4.4.1 Antibody Titrations*

30 000 cells/well were cultured in SGM overnight at 37˚C, 5% $CO_2$ and 90% humidity in Lab-Tek 8-well Chambered Coverglass Dishes (Thermo Scientific Nunc; USA). To protect the glass coverslips from scratching and improve sterility, the 8-well chambered dishes were kept in petri dishes. SGM was removed from each well and the sub-confluent cells washed with pre-warmed PBS (1x). Cells were

subsequently fixed with 100 µl absolute methanol for 10min at 4°C. After methanol removal, 200µl PBS (1x) was used to wash cells for 30 sec. Cells were permeabilized with 100 µl 0.1% Triton X-100 (Sigma-Aldrich; USA) at 4°C for 10min. After Triton X-100 was discarded, 200 µl PBS (2x) was used to wash cells for 30sec. A 100µl blocking solution of 20% FBS (Biochrom; Berlin Germany) was added to each well and incubated at room temperature for 20min. The blocking serum was removed from the wells, and primary antibodies were subsequently added without washing the cells with PBS. Primary antibodies (100µl) were added to each well and incubated overnight at 4°C. Table 4 comprises of detailed information on the primary and secondary antibody titrations performed.

In a dark room, primary antibody was discarded and the cells washed with 200 µl PBS (1x). Following PBS removal, 100µl secondary antibody was added to each well and incubated at room temperature for 60 min. Secondary antibodies were removed and 200 µl PBS (1x) used to wash the cells. A 100µl dilution of 1:100 of the nuclear stain Hoechst 33342 (MACS Miltenyi Biotec GmbH; Germany) was thereafter incubated in each well for 10 min at room temperature, followed by another wash step with PBS (1x). Dishes were stored at 4°C with a foil covering and one drop of glycerine based Fluorescent Mounting Media in each well preserving fluorescence (Dako North America Inc; USA). Ideally fluorescent imaging was completed on the same day for optimum fluorescence intensity. The workflow illustrated in Fig. 4.4.1 was followed to obtain confocal images during antibody titrations. The highlighted concentration in Table 4 indicated the optimal antibody dilutions determined during titrations. The optimal dilutions were selected based on: 1) low background noise, 2) low non-specific binding, 3) lowest antibody concentration used whilst still staining essential target proteins as depicted in Fig.4.4.2 A-C.

Table 4: Primary (Ab1) and Secondary (Ab2) Antibody Titrations

| **Ab1** / **Ab2** | **PBS (control)** | **1:100** | **1:200** | **1:400** |
|---|---|---|---|---|
| **1:200** | Talin | Talin | Talin | Talin |
| | Vinculin | Vinculin | Vinculin | Vinculin |
| | Integrin-β1 | Integrin-β1 | Integrin-β1 | Integrin-β1 |
| **1:400** | Talin | Talin | Talin | Talin |
| | Vinculin | Vinculin | Vinculin | Vinculin |
| | Integrin-β1 | Integrin-β1 | Integrin-β1 | Integrin-β1 |

Footnote: All antibodies were purchased from Abcam England (*Vinculin:* Rabbit Anti-Vinculin ab155120 and Alexa Fluor 647 (Goat pAb to Rb IgG). *Talin:* Mouse Anti-Talin 1 antibody ab157808 and Alexa Fluor 488 (Goat pAb to Ms IgG). *Integrin-β1:* Rat Anti-Integrin-β1 ab95623 and Alexa Fluor 555 (Goat pAb to Rat IgG)). Antibody stocks were centrifuged (to pellet down crystals) and antibody dilutions were vortexed before use for ≤5sec. *Final concentrations selected are highlighted in the table.*

*4.4.2 Fluorescence Image Acquisition (Confocal microscopy)*

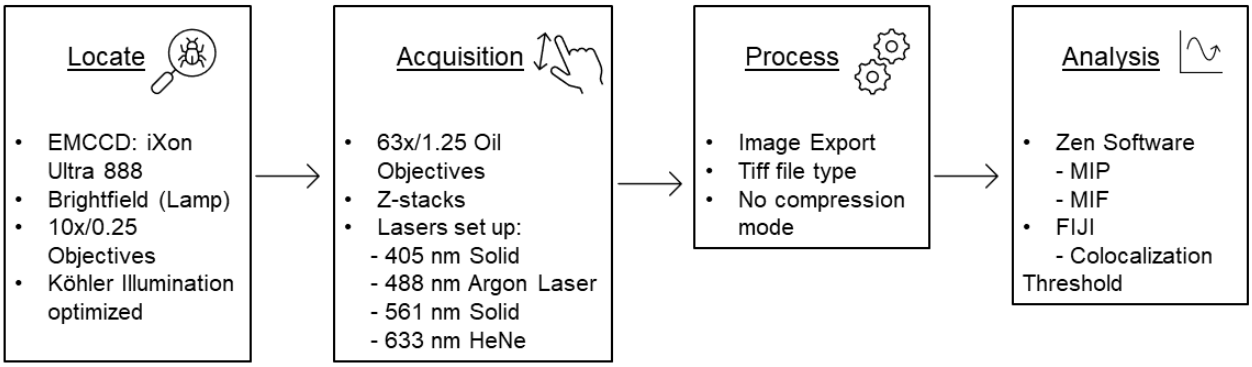


**Figure 4.4 1 Workflow of Confocal Image Acquisition.** Fluorescent imaging was performed on LSM780 ELYRA PS1 microscope. Low intensity settings were used to locate cells (brightfield lamp illumination and 10x/0.25 objectives), while imaging was accomplished with high powered lasers. 488nm Argon Laser: Talin, 561nm Solid: Integrin-β1, 633nm HeNe: Vinculin, 405nm: Nucleus (violet laser). The intensity in generated images was analysed with MIP (maximum intensity projection) and MFI (mean fluorescent intensity)

Photobleaching (loss of fluorescent intensity) before cell imaging was reduced by turning off main lights in the microscope room and locating cell under the microscope with brightfield settings (20% TL LED illumination).

Confocal imaging was conducted on an LSM 780 ELYRA PS1 microscope with ZEN 2011 software. Z-stack imaging was of all planes including from above the coverslip through the cell. The step width of each plane was the default value of the imaging interval over the number of slices, ranging from 0.5281 µm to 0.5545 µm ($\frac{3.169\ \mu m}{6\ slices}$ to $\frac{4.436\ \mu m}{8\ slices}$). Detailed confocal settings, and wide-field settings, are in Appendix B, pg 94. A magnification of 63x/1.25NA Oil objective was used along with the following setup: 1) Talin - Alexa Fluor 488 was excited with the 488nm Argon laser and emission was detected with the GaAsP detector from 490nm to 570nm, 2) Vinculin - Alexa fluor 647 excitation was achieved with the 633nm laser and emission detected from 637nm to 758nm, 3) Integrin-β1 - Alexa Fluor 555 was excited at 561nm and emission detected from 565nm to 626nm, 4) Hoechst 33342 was excited with the 405nm laser and emission detected in the range 415nm – 490nm. Negative controls, a reference for non-specific binding, were included as stains without primary antibody. Single stained controls confirmed whether spill over was eliminated.

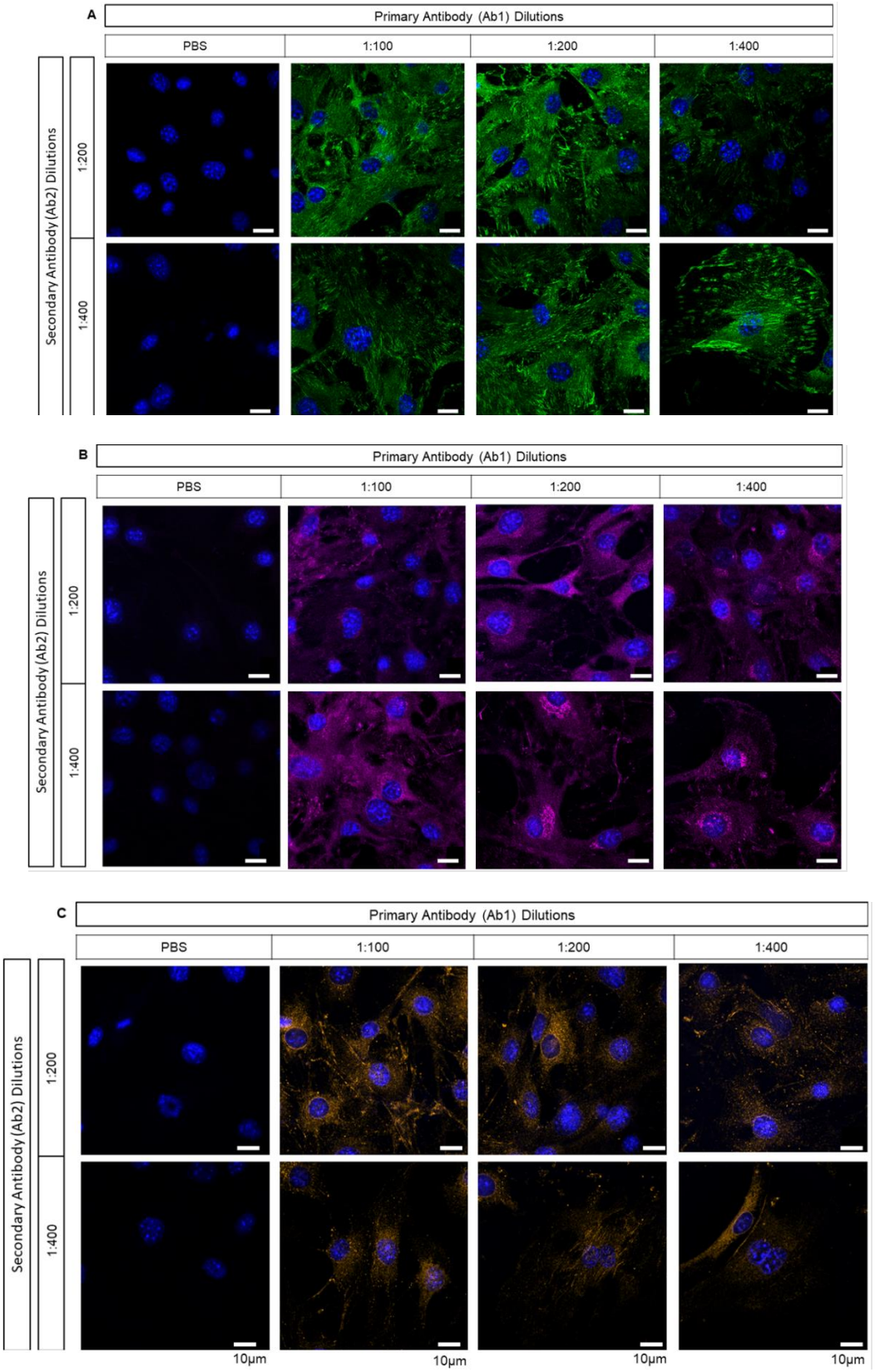


**Figure 4.4.2 Antibody Titrations** with **(A)** Talin (green**) (B)** Vinculin (pink) and **(C)** Integrin-β1 (orange) stains on methanol fixed cells**.** The primary and secondary dilutions were as follows respectively: (PBS & 1:200); (PBS & 1:400); (1:100 & 1:200); (1:100 & 1:400); (1:200 & 1:200); (1:200 & 1:400); (1:400 & 1:200); (1:400 & 1:400) for all the titrations. Scale bar set at 10µm.

*4.4.3 Fixative Testing*

In comparison to the above utilized methanol additional fixatives were optimized namely: 4% formaldehyde (Merck Schuchardt OHG, Germany) and a mixture of 4% formaldehyde and 2.5% glutaraldehyde (Agar Scientific, Stansted Essex). Table 5 indicate fixative optimization at 37°C using varying time points.

An alternate ICC staining protocol was followed to optimize cell fixatives: 1) Following SGM removal and cell washing with pre-warmed PBS (1x) at room temperature, a fixative was added in a dish and incubated for a specific time (90min, 40min, 10min) at 37°C. 2) After fixative removal, cells were washed with 100µl pre-warmed PBS (2x) for 5min at room temperature and permeabilized with 100µl of 0.1% Triton X-100 for 6min at 4˚C. Permeabilization was halted with Triton-X removal and thorough cell rinsing with PBS (2x) for 5 min at room temperature. 3) Non-specific binding was blocked with 20% FBS for 20min at room temperature. 4) After blocking serum was removed cells were incubated with 100µl of primary antibody cocktail overnight at 4˚C. The antibody cocktails contained the optimal antibody dilutions determined during titrations, highlighted in Table 4. The primary antibody cocktail was discarded, and cells washed with PBS (1x) at room temperature. 5) A 100µl secondary antibodies cocktail was added to cells for 1 hour and thereafter cells washed with PBS (1x). 6) Fluorescence was preserved with the addition of mounting media and foil covering at 4°C. Images were acquired as discussed previously and depicted in Fig.4.4.3A.

Table 5: Fixative Optimization

| Fixative | Temperature (°C) | Duration (min) |
|---|---|---|
| 4% Formaldehyde | 37°C | 90min |
| | | 40min |
| | | 10min |
| 4% Formaldehyde & 2.5% Glutaraldehyde | | 90min |
| | | 40min |
| | | 10min |

Footnote: Sample dishes were incubated in an incubator for allocated times

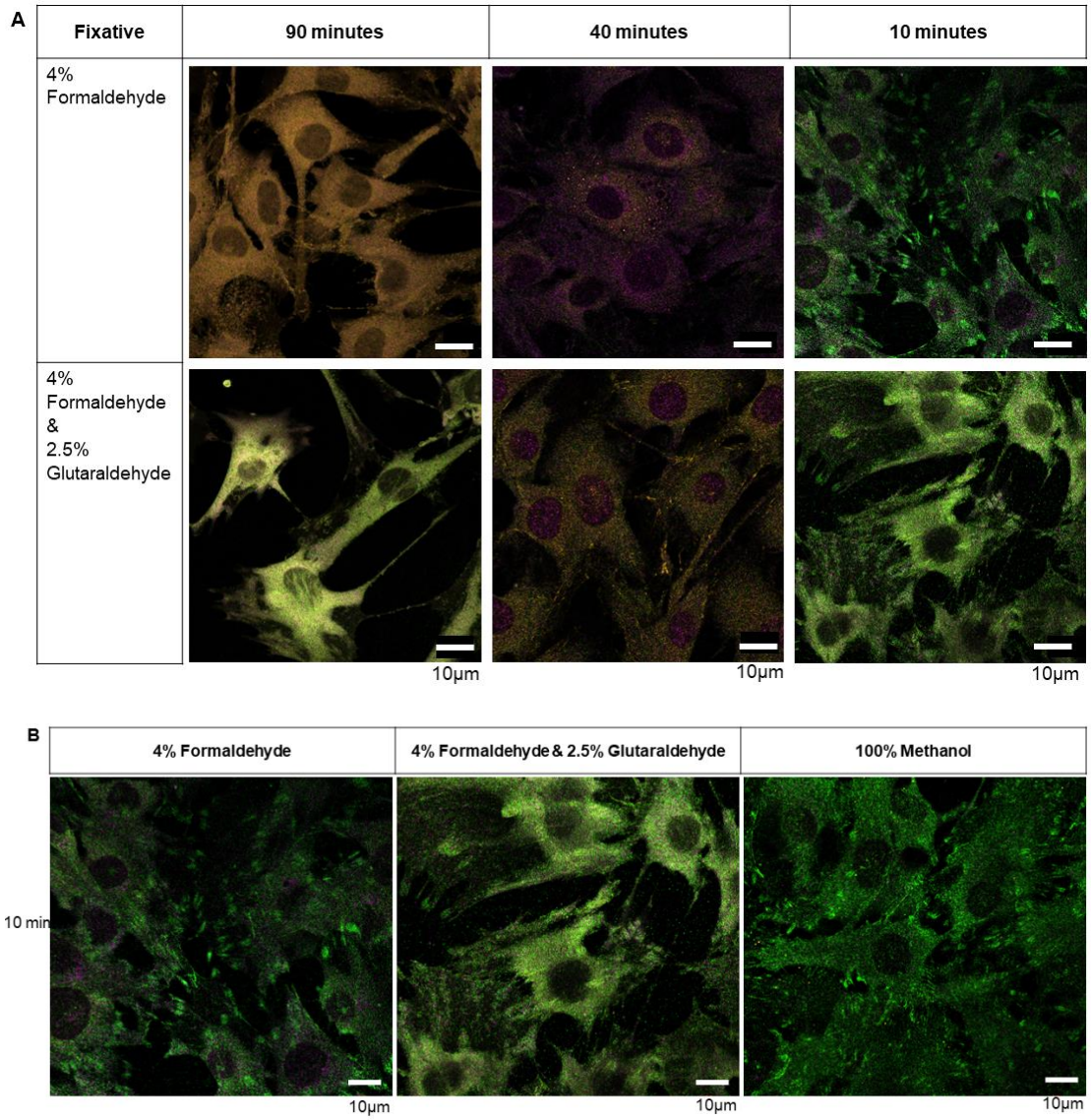


**Figure 4.4.3 (A) Comparing effect of different fixatives.** 4% Formaldehyde and 4% Formaldehyde & 2.5% Glutaraldehyde incubated at 37ºC for 90 min, 40 min and 10 min. The antibody cocktail stained talin (green), vinculin (pink) and integrin-β1 (orange). **(B)** Methanol compared to Optimal Fixatives. 4% Formaldehyde and 4% Formaldehyde & 2.5% Glutaraldehyde and absolute Methanol were comparable and hence optimal at 10 min. Image acquisition settings on LSM 780 Elyra PS1 are provided in *Appendix B, pg. 94* The scale bar was 10µm.

In subsequent confocal experiments aimed at quantifying the expression of adhesion proteins during cellular migration, methanol was used as fixative, due to the low background noise with high intensity of detected proteins associated with it (Fig.4.4.3B). Methanol fixing is however not ideal for advanced super resolution microscopy with scientific literature showing preference for the use of formaldehyde as fixative. Based on the optimization experiments, 4% formaldehyde (incubated for 10min) was therefore utilized in TIRF and STORM experiments since prominent FA complexes were also visibly stained and suitable for imaging. The testing of varying fixatives and fixative durations was crucial in generating images with accurate structure representation. The long fixation incubations provided insight into effects of prolonged fixations in ICC, in contrast to well used prolonged fixations in tissues staining (immunohistochemistry) *(Van Seijen, M. et al., 2019; Berod & Pujol., 1981)*.

### *4.4.4 Confocal Imaging*

Following all ICC optimization, a four-colour confocal experiment was set up to assess the expression and localization of the adhesion proteins of interest during cell migration. The experiment was done in triplicate (N=3, n=3) with three cells imaged along the migration front in each well.

*Confocal obtained Image analysis*

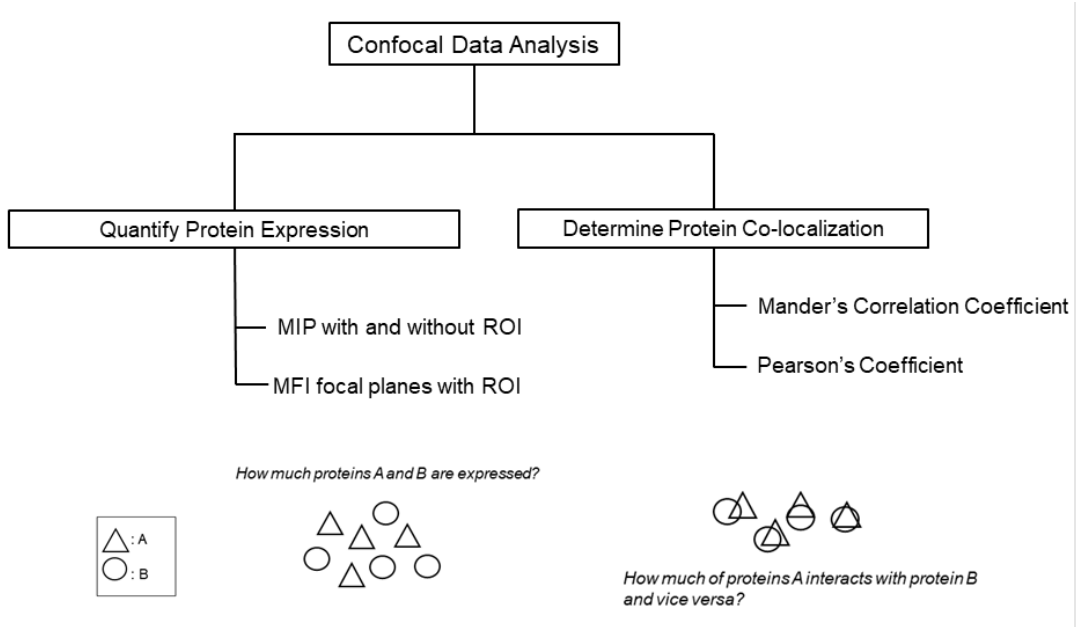


**Figure 4.4.4 Confocal microscopy data analysis overview**. Z-stack images were taken, and the quantity of expressed proteins determined using 1) MIP (Maximum Intensity Projections) of the entire Z-stack and 2) MFI (Mean Fluorescent Intensity) on 3 selected focal planes. Protein co-localization was subsequently assessed using Mander's Correlation Coefficient and Pearson's Coefficient. Image analysis was performed using Zeiss software. (ROI: region of interest.)

The Zen software generated fluorescent intensity values from the acquired Z-stack images were generated using two different methods 1) Maximum Intensity Projection (MIP) and 2) Mean Fluorescent

Intensity (MFI) of selected focal planes to quantify protein expression. MIP measured the highest intensity values within the Z-stack while MFI considered the average intensity on one plane. Subsequently, co-localization analysis evaluated the co-occurrence and correlation of two proteins with each other using Mander's Correlation and Pearson's Coefficients, respectively. The analysis was conducted on FIJI (ImageJ 1.52p, nih.gov, USA) with Colocalization Threshold following the steps summarized in Fig.4.4.4.

The set parameters in FIJI (ImageJ 1.52p, nih.gov, USA) included: 1) Clearing of image background noise with 75 subtraction before analysis. Subtracting values above 75 had no significant changes in background noise reduction while values below 75 removed essential protein signals; and 2) Selecting the longest wavelength of the specific protein pair for Channel 1 (i.e., Alexa Fluor 555 generated images vs Alexa Fluor 488 or Alexa Fluor 647 generated images) and the shorter wavelength for Channel 2. The analysis was completed with and without the selection of a region of interest (ROI). A ROI in generated images was the outline of the specific cell, excluding the background pixels. The ROI was determined/outlined manually in each image to avoid bias (Fig. 4.4.5). Thereafter, analysis was performed on the ROI selected regions of the image. The resulting data generated provided insight into protein quantity and potential interactions as well as the importance of selecting the appropriate image analysis strategy.

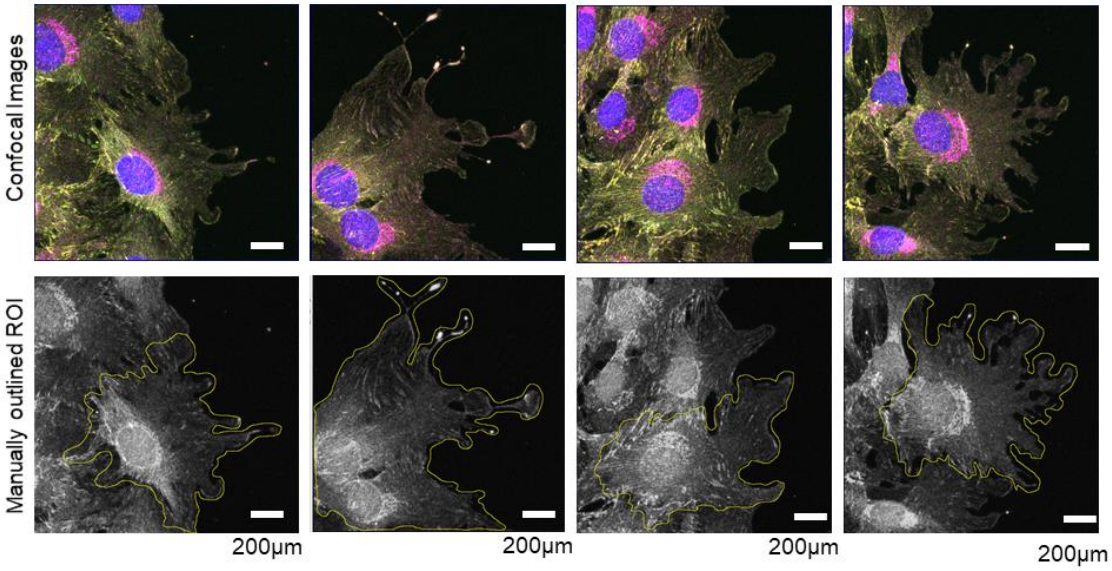


**Figure 4.4.5 Identification of a ROI in confocal image analysis.** In FIJI software freehand tool was used to outline ROI for all generated images and organised in ROI manager. Scale bar 200µm.

## 4.5 Super Resolution (SR): TIRF and STORM Optimization

There were a few considerations taken to ensure effective imaging before the actual SR imaging such as: 1) utilizing the recommended coverslips of #1.5H thickness (high performance) (found on ibidi µ-Dish$^{35\ mm,\ high}$ migration dishes), 2) specific buffers during imaging such as Abbelight Smart Kit Super-resolution buffer solution, and 3) Frequent objective oil changes.

The optimized sample preparation protocol described previously (section 4.4) was used to prepare TIRF and STORM samples. Figure 4.5.1 indicates the workflow of acquiring data through TIRF and STORM configurations.

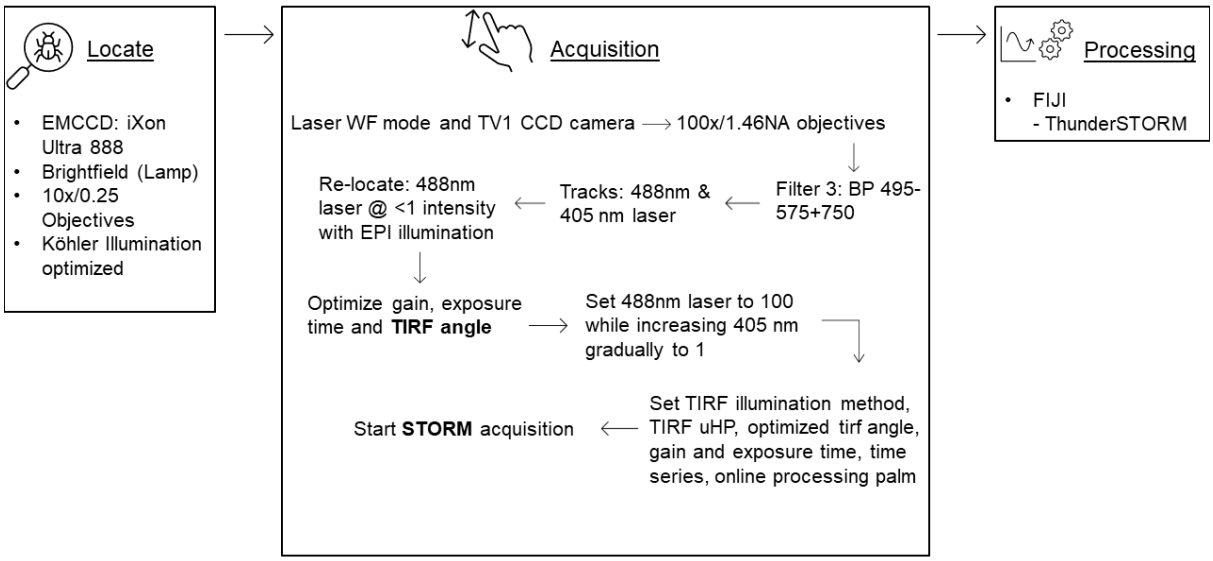


**Figure 4.5.1 TIRF and STORM configuration summary.** Cells are located at low intensities with 488nm laser and standard EPI illumination, along with the optimal TIRF angle, exposure time and gain. The 488nm laser is set on 100 for STORM imaging, and violet laser 405nm set to 1 to assist blinking. The parameters are set, and image acquisition is initiated. The generated data was processed and analysed with ThunderSTORM.

### *4.5.1 TIRF Establishment*

Imaging the optimized protein for SR, talin, the 488nm laser was set at low intensity (4-5%), and emission was detected with the BP 495-575+750 (Zeiss filter set 3). An electron multiplying charged couple device (EMCCD camera) (iXon Ultra 888, Andor) with fastest megapixel collection and high single photon sensitivity was used during imaging. The light path followed to accomplish the latter was Laser WF mode in the ZEN2011 software. TIRF angle optimization was done on low laser settings (<1%), gain (5-10) and exposure time (milliseconds) (50ms – 100ms) with initially EPI illumination mode, followed by optimizing TIRF angle required for total internal reflection fluorescence. Even illumination across the field of view was maintained with the collimator kept constant. Images were acquired in Z-stack with a step width of 0.5µm to evaluate the efficacy of the TIRF settings.

### *4.5.2 TIRF analysis*

TIRF analysis evaluated the FA dense network of the different treatment groups. The Freehand Tool on FIJI was used to outline the detected FA complexes for Area, Length and Breadth measurements. The compiled data was further assessed with statistical analysis to determine significance within the measured groups and the FA shape factor. Figure 4.5.2 outlined the TIRF analysis process.

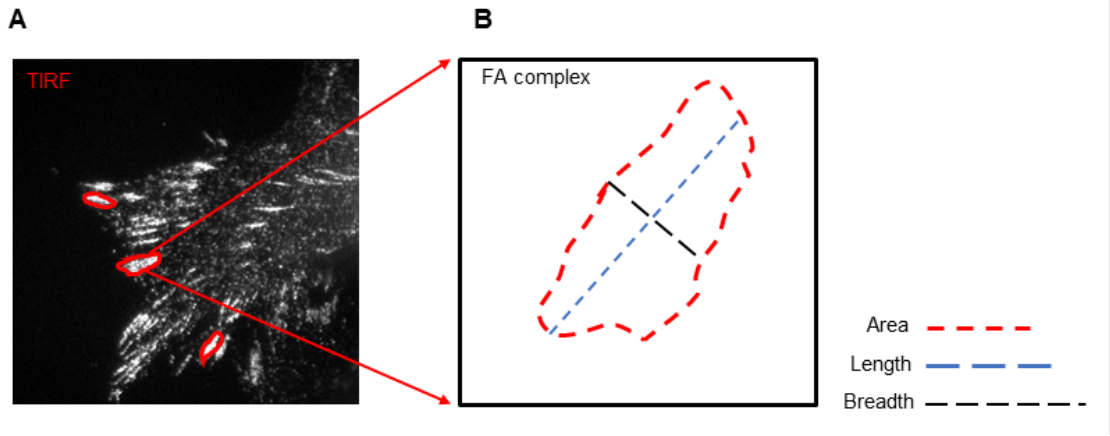


**Figure 4.5.2 TIRF FA analysis.** The imaged FA complexes were measured for Area, Breadth and Length to determine FA Shape Factor. Shape factor = 1 = perfect circle; Shape factor = 0 = perfect straight line

*4.5.3 STORM Establishment*

A reducing buffer is required for fluorophores to assist in the generation of a blinking event during STORM imaging. A commercial product called Smart Kit Super-Resolution Buffer solution (Abbelight, France) was used for consistent fluorophore blinking. 100µl super-resolution buffer was added on a migration dish in a designated area drawn with a wax pen (Dako, Denmark) prior to imaging. Cells were located using the 488nm excitation laser at intensity <1% with the EPI illumination mode. The area of illumination was reduced by using TIRF-uHP in the ZEN software and cropping field of view as low as possible i.e., 256x256 pixels thereby reducing laser exposure time to as low as 18ms. The range indicator was used to ensure the gain level was not saturating the signal, yielding optimal gain at 300. STORM imaging started with the 488nm laser increased to 100% while the 405 laser was increased gradually during blinking from 0.1 – 1%. Time series was selected and set to acquire 50 000 frames. Definite Focus was activated ensuring the sample stayed in focus during acquisition. The microscope is also mounted on an anti-vibration table to ensure no major fluctuations. Online Processing Palm was activated during imaging to follow image build up in real time. The experiment was done in triplicate and at least three cells per treatment group were imaged. STORM and TIRF configurations described above were combined to image Talin in a single focal plane above the coverslip. Detailed TIRF and STORM settings are found in Appendix C, pg 95.

*4.5.4 Image Analysis (ThunderSTORM)*

ThunderSTORM was ideal for image analysis as it works well with datasets generated from Zeiss Elyra microscopes while the wide variety of algorithms within the plugin enable fine tuning of data.

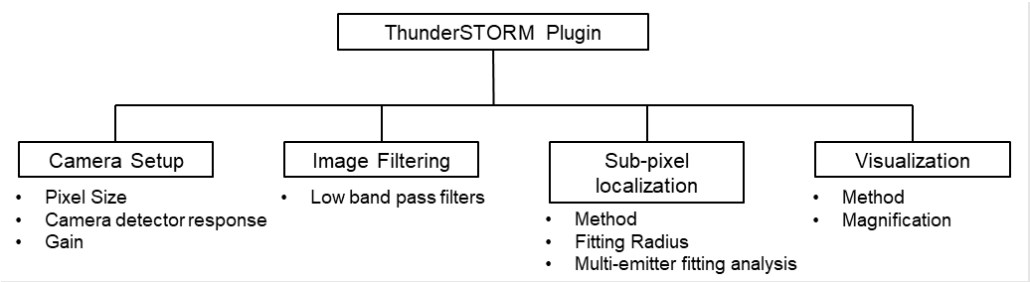


**Figure 4.5.3 Parameters for ThunderSTORM plugin.** The parameter settings were optimized for accurate localization from the acquired data. The camera setup is crucial in the estimation of fluorophore localization and fitting methods. Image filtering enhances the generated data and eliminate unwanted signals. Approximate localization of molecules is optimized with specific methodology, fitting radius, and peak intensity threshold. The generated data is used to construct resolvable structures.

ThunderSTORM was installed on FIJI software (ImageJ 1.52p, nih.gov, USA) and all parameters seen in Figure 4.5.3 were custom set tailored to the generated data sets. The camera detector response was 3.6 (photoelectrons per A/D count) and 500 (base level A/D count). The effective pixel size was 130 nm and electron multiplying gain (EM gain) was 100. The preferred low band pass filter for image enhancement and filtering was the Gaussian Blur with smallest kernel (B-spline order and scale were 3 and 2.0, respectively). Non maxima suppression algorithm was used to find the approximate position of molecules with an 8-neighbouring connectivity. The threshold value is highly influenced by the nature of the data, and ThunderSTORM updates the value for every input image. Sub-pixel localization of molecules was determined with Point Spread Function: Gaussian and the maximum likelihood estimation fitting method with a radius of 3. Multi-emitter fitting was disabled. The data was processed and visualized with methods such as histograms or scatter plots.

The generated data from ThunderSTORM yielded results into various categories, as depicted in Fig.4.5.4, required to construct the projected image.

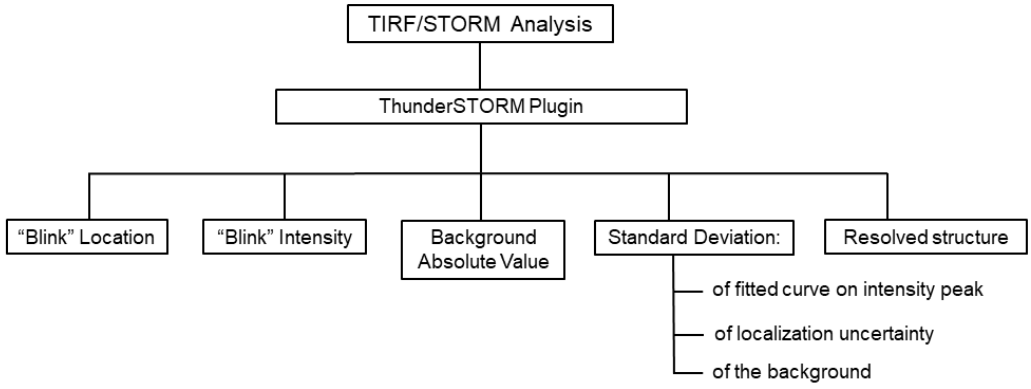


**Figure 4.5.4 ThunderSTORM generated results.** The improved resolution structure is constructed with STORM data: fluorophore "blinking" location, fluorophore "blinking" intensity, background noise and standard deviations. Single fluorophore intensity distribution and location is crucial in accurate molecule localization, with the use of the standard deviations and background noise reduction to improve localization.

## 4.6 Statistical analysis

Statistical analysis was performed using GraphPad Prism (version 8.2). One-Way ANOVA with Tukey post hoc test was used to determine either a treatment effect or an effect of time. Factorial ANOVA was used to determine effect of time, effect of treatment, effect of treatment x time. The level of significance was accepted at $p<0.05$.

# Chapter 5: Results

## 5.1 Dose Response: Cell viability in AAP supplemented media

The highest non-toxic AAP concentration was determined through cell viability testing over a period of 24h, 48h and 6 days (6d). Refer to Figure 5.1.1 for representative images illustrating crystal violet staining during the respective time points for the SGM (control) and AAP (0.15mM, 0.3mM, 0.6mM, 1.2mM and 2.4mM) treatment groups. A steady growth curve was evident, under SGM conditions, with cell confluency increasing by 3.1±1.7 (48h) and 4.6±0.9 (6d) fold change relative to viability at 24h ($p<0.05$) (Fig. 5.1.2A). The highest concentration of AAP tested (2.4mM) was cytotoxic with a significant reduction in cell viability evident over the 6d time point (0.3±0.07 fold), ($p<0.01$) compared to SGM at the same time point. Cell viability was maintained in all experimental conditions exposed to lower AAP concentrations (0.15mM, 0.3mM, 0.6mM) (Fig. 5.1.2 B-D). The highest non-toxic AAP dose that maintained cell viability to a similar extent to SGM over the 6d period was 0.6mM. Refer to Figure 5.1.3 for comparative images of crystal violet-stained cells after 6 days of treatment with 2.4mM and 0.6 mM AAP concentrations against SGM (control).

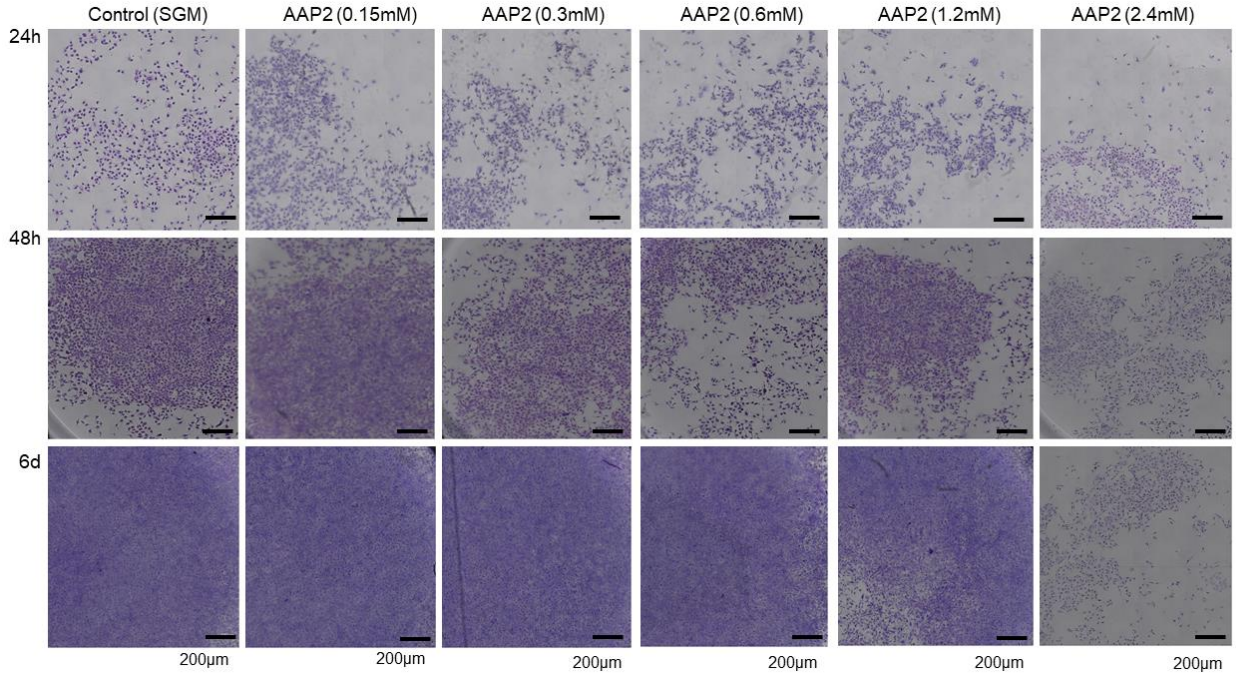


**Figure 5.1.1 Representative images of Crystal Violet Staining.** Images were acquired with 10% TL LED intensity (brightfield) using the 10x/0.25NA objectives on Zeiss Axio-Observer Microscope. Viability was assessed after 24h, 48h and 6d of media supplementation with (0.15mM, 0.3mM, 0.6mM, 1.2mM, 2.4mM) and without (control: SGM) AAP. The scale bar was 200µm.

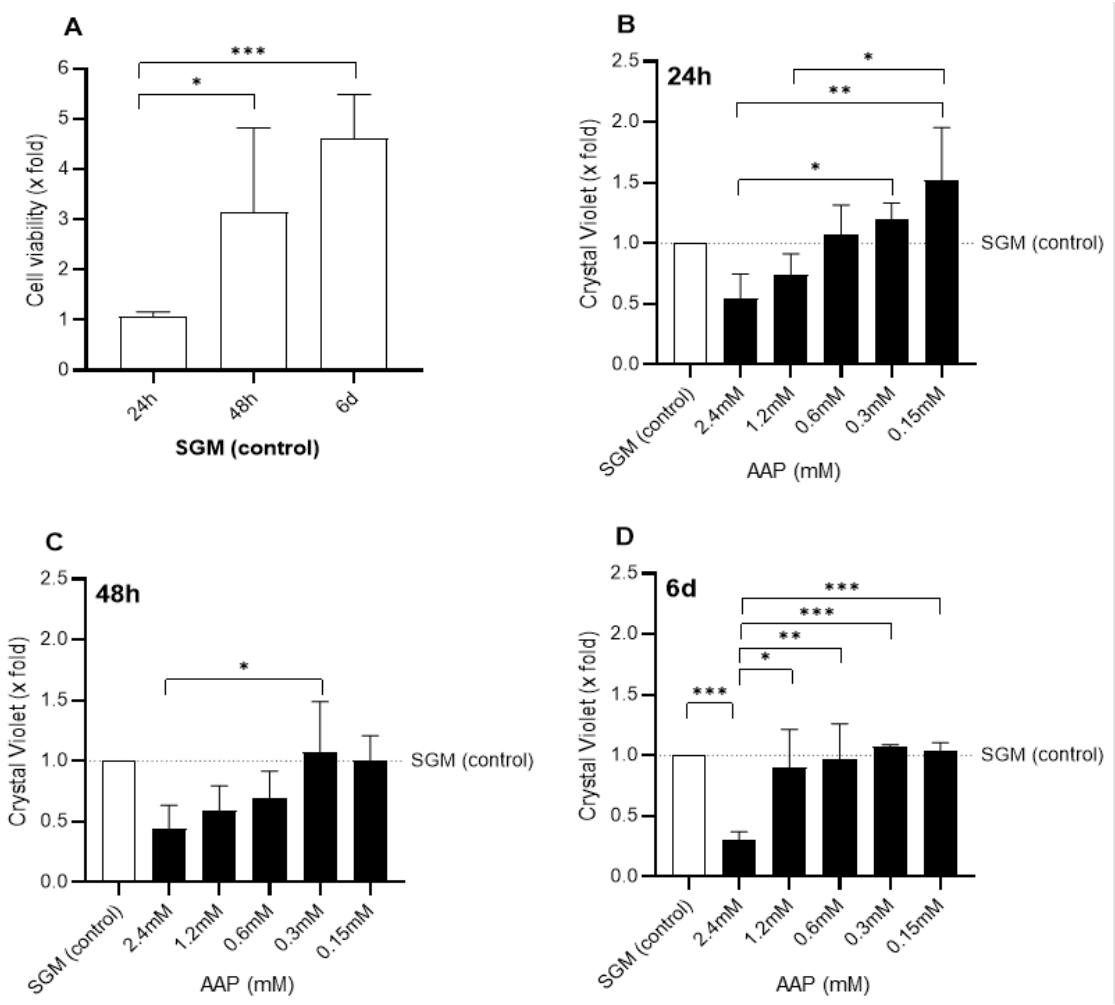


**Figure 5.1.2 Quantification of Crystal Violet Staining.** MSCs were cultured in either standard growth media (SGM) or treated with different concentrations of AAP and cell viability assessed with Crystal Violet staining at 24h, 48h and 6d. **(A)** MSC growth over time under standard culture conditions. **(B-D)** The effect of AAP treatment on cell viability compared to SGM (set=1) at 24h **(B),** 48h **(C)** and 6 days **(D).** Values are presented as mean±SD. *Statistical analysis:* One-way ANOVA with Tukey hoc test (*p<0.05; **p<0.01; ***p<0.001).

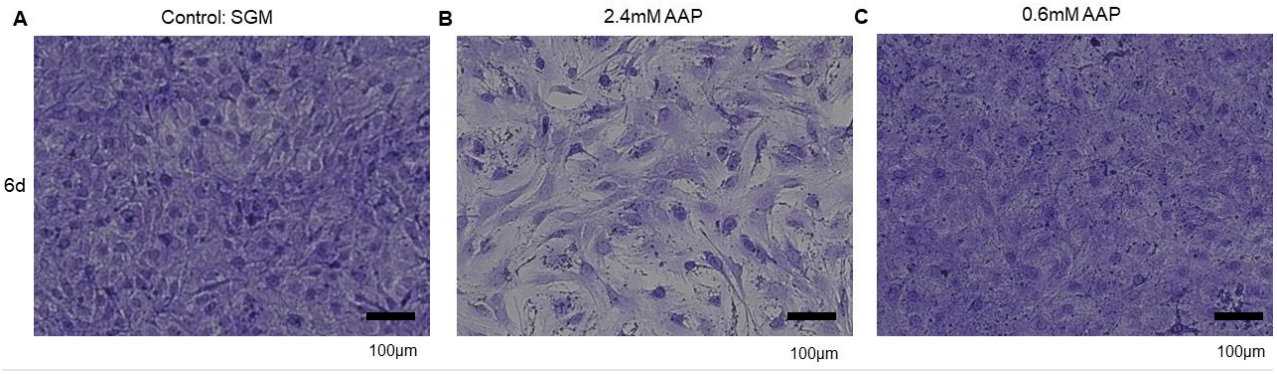


**Figure 5.1.3 Crystal Violet Staining in 96-well plates. (A)** Control: SGM **(B)** 2.4mM AAP and **(C)** 0.6 mM AAP supplementation over 6d. Images were acquired with 10% TL LED intensity (brightfield) using the 10x/0.25NA objectives on Zeiss Axio-Observer Microscope. Scale bar was 100µm.

## 5.2 Cell Migration: Ideal time point at which distinct pseudopodia are identifiable in migrating MSCs.

Cell Migration (wound closure) was followed with live cell imaging over a period of 24h as illustrated in Figure 5.2.1 for SGM (control) and 0.6mM AAP supplemented media. Complete wound closure in SGM and AAP treated media was observed after 20h and 24h respectively. Pseudopodia and cell endings were noticeably elongated and satisfactory visible at 8h in all treatment groups. Figure 5.2.2A compares the visible pseudopodia at 8h in contrast to the undistinguishable cell endings at 0h and starting pseudopodia at 4h. Quantification of the percentage wound closure over the initial 12h period indicated significant differences ($p<0.05$) in the migration rate of SGM and 0.6mM AAP treatment groups for all time points. Compared to SGM (12h: 70.4±7.3% wound closure), AAP supplemented media (12h: 44.3±10.0% wound closure) significantly delayed cell migration (Fig. 5.2.3).

Mit. C was the additional control in all treatment groups inhibiting proliferation, therefore ensuring only migration was tracked, as cells regulate migration and proliferation closely. Distinct pseudopodia at 8h were observed in SGM (with mit. c) and AAP treated media (with mit. c) (Fig. 5.2.2B). A delay in cell migration was noted in AAP supplemented media (with mit.c) compared to SGM (with mit.c) for all time points. A significant difference in wound closure at 12h was noted between SGM (without mit. c) (70.4±7.3%) and SGM (with mit. c) (33.9±3.6 %) (Fig. 5.2.3).

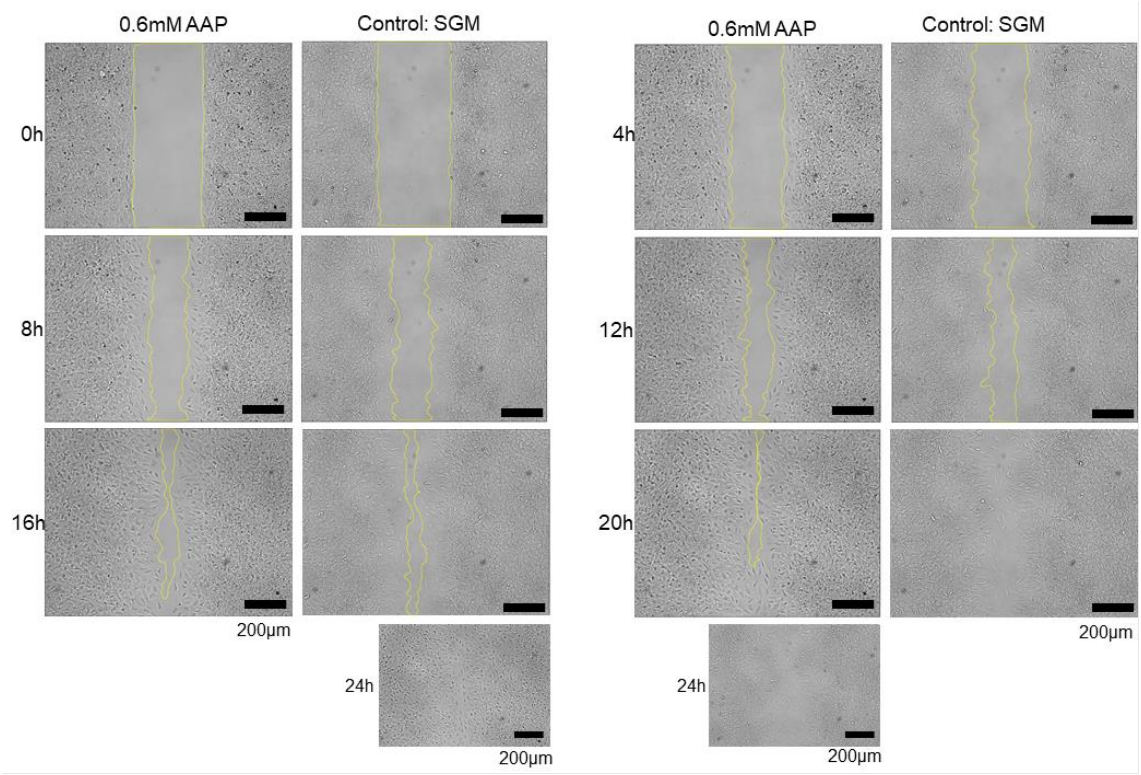


**Figure 5.2.1 Live Cell Migration over 24h** (at 4h intervals) in SGM (control) and AAP treated media was monitored over a 500µm artificial wound gap on the Zeiss Axio-Observer Microscope with 15% LED intensity using 5x/0.15NA objectives. Scale bar was 200µm. *Appendix D, pg. 98 shows the complete 24h cell migration.*

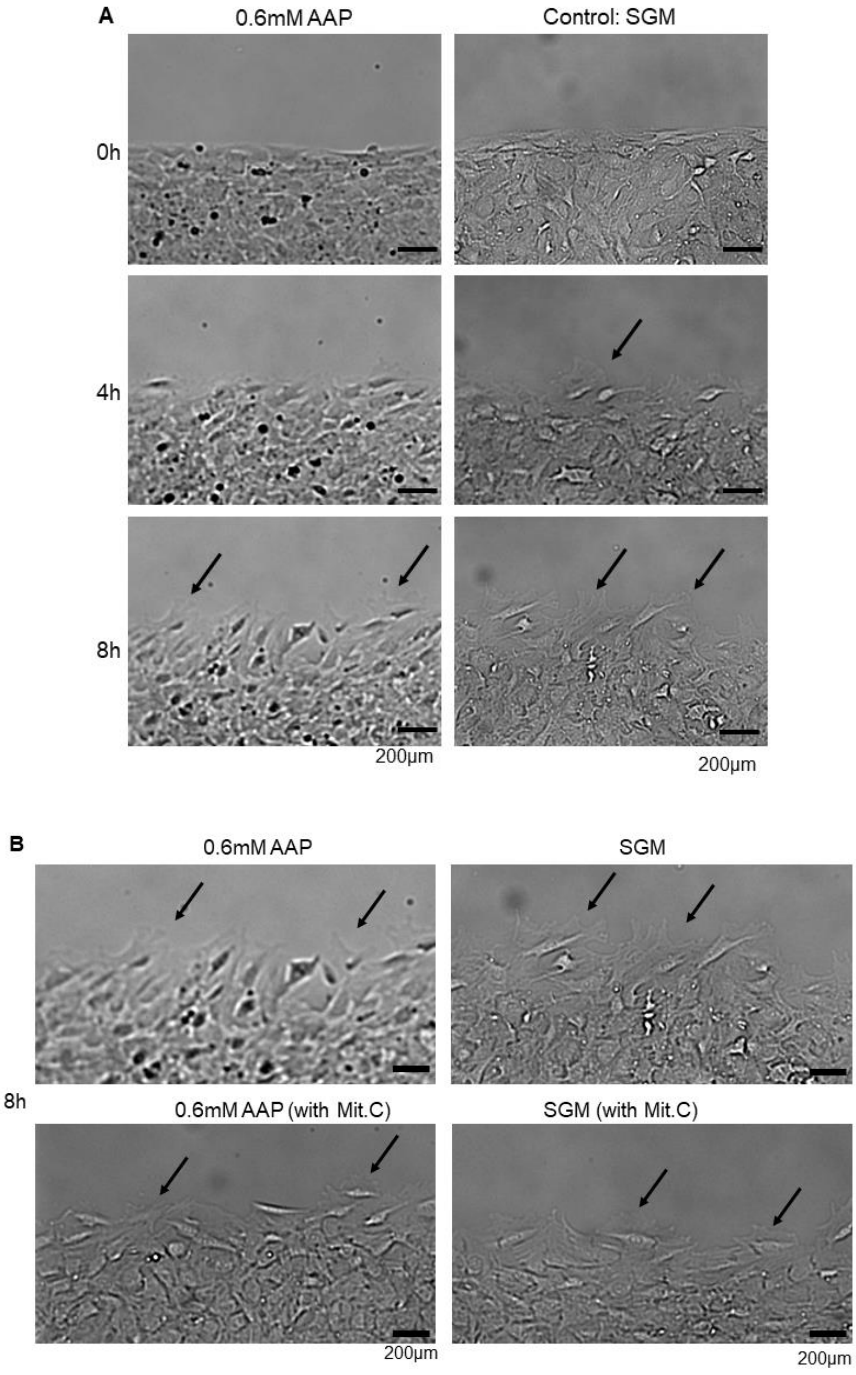


**Figure 5.2.2 Comparing Cell Endings. (A)** SGM and AAP treated media indicated defined cell pseudopodia at 8h compared to 4h time point, with the non-migrating cells (0h) as the no pseudopodia reference. Images were magnified to 29%. **(B)** At 8h all treatment groups indicated defined cell endings. Images were magnified 46%. Images were acquired with 15% LED intensity using 5x/0.15NA objectives. Scale bar was 200µm.

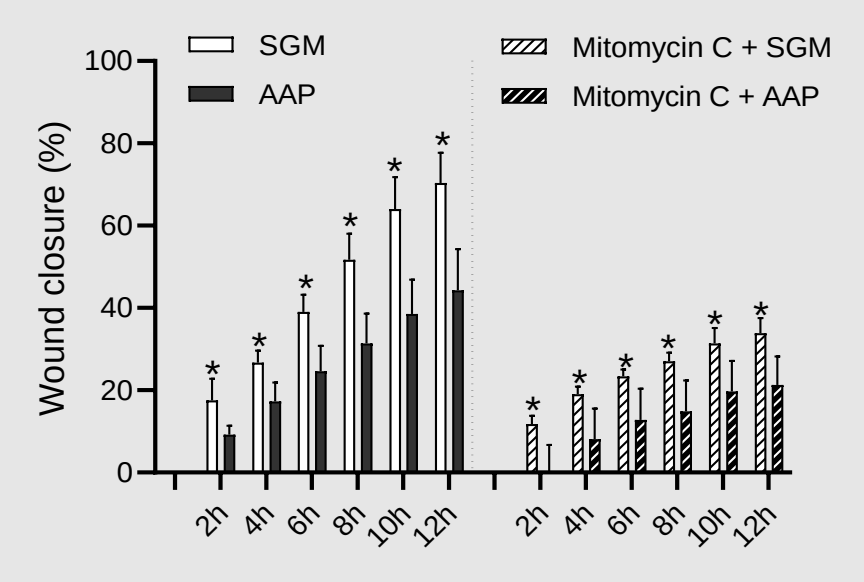


**Figure 5.2.3 Percentage Wound Closure over 12h** in SGM and AAP treated cells with and without Mitomycin C. *Statistical analysis:* Factorial ANOVA with Tukey post hoc test, *p<0.05 indicate significant difference between treatment groups; with values presented as mean±SD. *Appendix D, pg. 98 shows the complete 24h cell migration for all treatments with mitomycin c.*

*Cell Tracking*

For each of the treatment groups, the live cell imaging experiment was used to track 6 individual cells in each well. It should be noted that the selected cells were the fastest migrating cells in each well and does therefore not accurately represent overall migration and the rate of wound closure. Migrating cells showed accumulated distance (measured distance considering the entire path travelled) of 377.9±32.6µm and 351.9±60.9µm in SGM and AAP supplemented media, respectively. Figure 5.2.4 demonstrate the accumulated migration distance in SGM and 0.6mM AAP supplemented media with directionality. Cell migration was directional in SGM and AAP treatments, with directionality of 0.74530 and 0.7303, respectively (Directionality = 1 = straight line motion; Directionality = 0 = non-straight motion). The average velocity at which cells travelled in SGM was 0.7214±0.071µm/sec while in AAP treated media was 0.6660±0.115µm/sec. Additionally, euclidean distance was measured, considering the distance between two points, the beginning and final point, which is advantageous in overlooking any objects in the travelled distance that might affect analysis. The euclidean distance for SGM and AAP treated media was 281.49±32.4µm and 254.29±29.6µm, respectively. It should be noted that to accurately quantify differences between SGM and AAP treated cells, at least 50 cells should be tracked per treatment group. The data presented here is only indicative of the “fastest” migrating cells and not the overall rate of migration / wound closure.

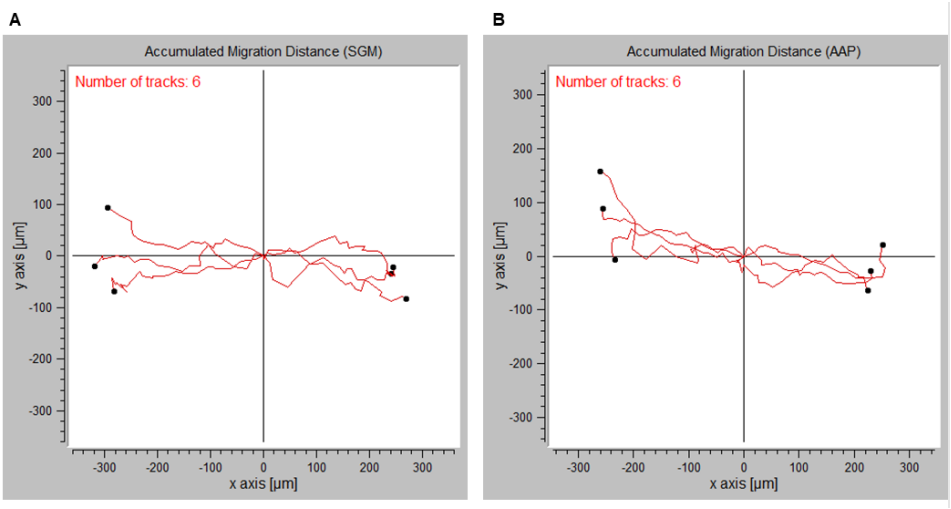


**Figure 5.2.4 Accumulated Distance and Direction Plots** for SGM and AAP treated media migration. The Chemotaxis and Migration Tool was used to follow 6 cells in each treatment (three on either side of the artificial wound). The migration of each cell (black dot) is presented on a centred grid with x/y calibration of 0.908µm over 22 seconds tracked on 25 slices.

## 5.3 Immunocytochemistry (ICC): Assessing expressed proteins with confocal microscopy.

Confocal microscopy was used to investigate the distribution of, and possible interactions between the proteins of interest: integrin-β1, talin and vinculin. The proteins of interest in AAP treated media were organized densely in FA complexes compared to SGM at 8h. Vinculin was predominantly located in the cytoplasm, around the nucleus in all treatment groups while integrin-β1 and talin overlayed on each other as seen in Figure 5.3.1 with combined channels, while separate channels are indicated in Figure 5.3.2. FA complexes were defined with the elongated dense/prominent filamentous structures effectively seen in Figure 5.3.1 0.6mM AAP treatment group indicated with the white arrows.

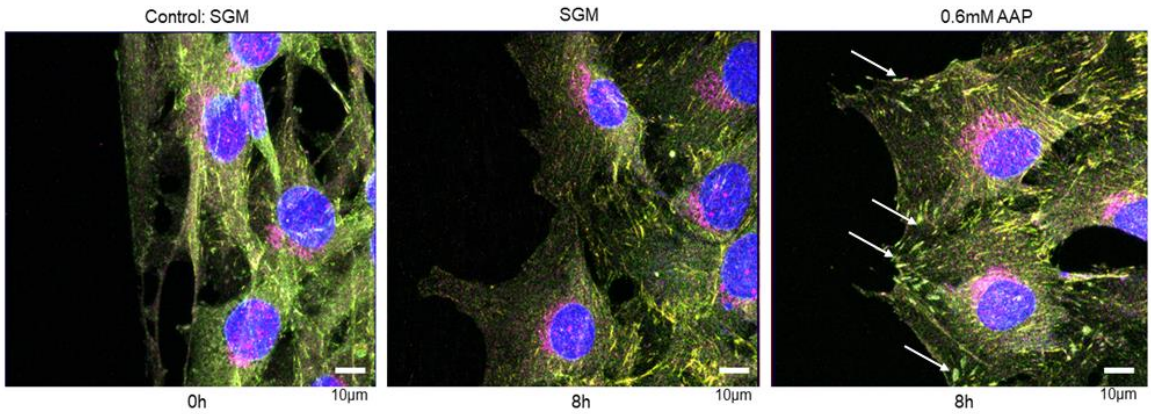


**Figure 5.3.1 Confocal ICC imaging with combined channels**: Non-migrating cells (0h) protein distribution compared to migrating cells in SGM and 0.6mM AAP treated media at 8h. Staining: Talin (green), Vinculin (pink) and Integrin-β1 (orange), Nucleus (blue). Scale bar was 10µm. Appendix B, pg. 94, indicate all Confocal Microscopy settings. Arrows: Indicate the FA sites

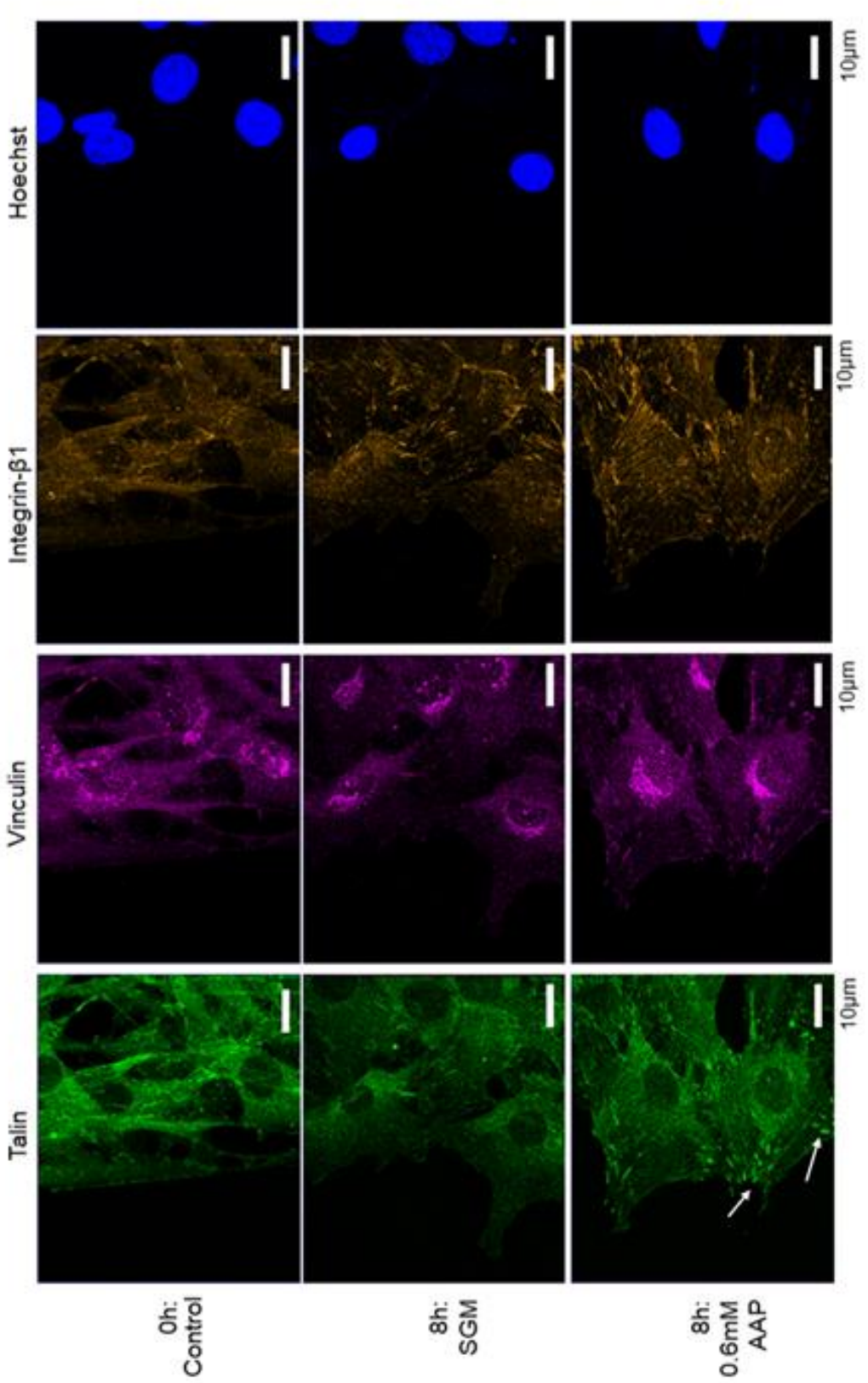


Figure 5.3.2 Multi-channels imaging protein distributions. Protein distribution in Non-migrating cells (0h) compared to migrating cells in SGM and 0.6mM AAP treated media at 8h. Stains: Talin (green), Vinculin (pink) and Integrin-β1 (orange) shows distinct patterns of protein expression. Hoechst was used to stain the nucleus blue. Scale bar was 10µm. Appendix B, pg. 94 indicate all Confocal Microscopy settings. Arrows: Indicate the FA sites

*5.3.1 Protein Quantification*

*5.3.1.1 Quantification of protein expression in Z-stack using Maximum Intensity Projection (MIP).*

Confocal micrographs were acquired in Z-stack, combining images taken at different focal planes throughout a cell including the out of focus coverslip region. The Z-stacks were processed as maximum intensity projection (MIP) images with an outlined cell selected as Region of Interest (ROI). MIP is a technique considering all intensities accumulated during imaging from the entire Z-stack, as opposed to Best Fit technique that considers the brightest intensities in acquired images. MIP analysis was further optimized with the selection of an ROI, that considered the cell and excluded background pixels. Figure 5.3.3 indicates the MIP for the expressed talin, vinculin and integrin-β1 detected in all treatment groups. Talin and vinculin were significantly higher in non-migrating control cells compared to SGM ($p=0.0023$) and AAP supplemented ($p<0.0001$) migrating cells. Similarly, integrin-β1 expression in AAP supplemented media tended to be lower than in non-migrating cells but did not reach statistical significance. Taken together this data suggest that regardless of treatment, there seem to be a reduction in the expression of adhesion molecules with the onset of cellular migration. AAP treatment did however not seem to have an effect on the overall the expression of adhesion molecules throughout the entire cell (MIP), since no significant difference in talin ($p=0.3783$), vinculin ($p=0.3783$) and integrin-β1 ($p=0.7427$) was observed between migrating cells in SGM and AAP treated media.

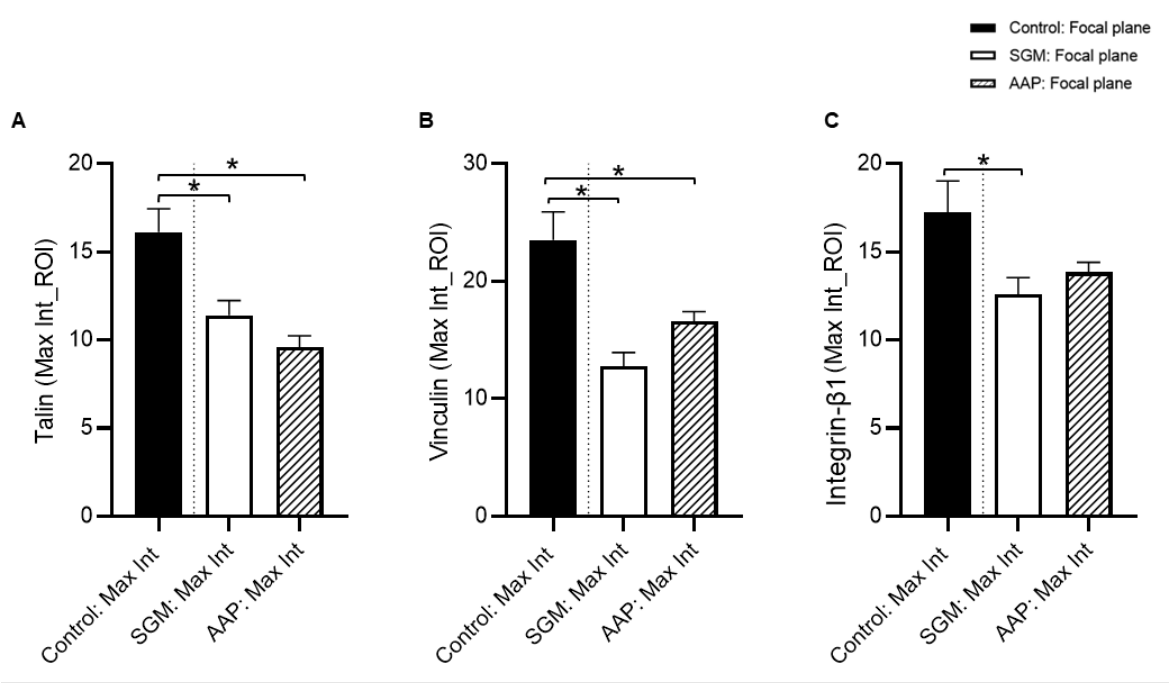


**Figure 5.3.2 Expressed Proteins assessed with MIP** (with ROI). **(A)** Talin **(B)** Vinculin and **(C)** Integrin-β1 were measured from a confocal microscope generated Z-stack. Values were expressed as mean±SD. *Statistical analysis*: Tukey's multiple comparisons test. Significance of $p<0.05$

*5.3.1.2 Quantification of protein expression in a single slice of Z-stack using Mean Fluorescent Intensity.*

MPI, as observed previously did not produce significant results during the comparison of expressed proteins in migrating cells followed in SGM and AAP treated media. To confirm this observation, additionally analysis using Mean Fluorescent Intensity (MFI) were conducted, which considered the optimal pixel intensities in a single slice of a Z-stack as opposed to entire Z-stack like MIP. The advantage of single slice analysis, particularly in our study was to investigate adhesion proteins occurring above the coverslip. The single plane above the coverslip was therefore referred to as the focal plane, as the focus for our study will be on adhesion proteins occurring in this plane. Figure 5.3.4 indicates the relative protein abundance based on MFI with and without making use of a defined ROI.

The effect of AAP treatment on adhesion molecule expression at the site of adhesion (immediately above the coverslip) was assessed by comparing it with SGM in migrating cells. No differences were detected in the expression of Talin between SGM and AAP treated cells (Fig. 5.3.4 B), whereas a significant difference was evident in the expression of both Vinculin and Integrin-β1 (Fig. 5.3.4 D, F) (#$p<0.05$) between treatment groups. The selection and importance of a ROI was adequately emphasised in these graphs, which indicate that significant differences were only noted between AAP treated media and SGM with the use of ROI. Care should however be taken that unintentional bias is not introduced to the date when the ROI is selected. A comparison of MFI analysis with and without a selected ROI was conducted to elucidate the importance of excluding extracellular space or background pixels during analysis.

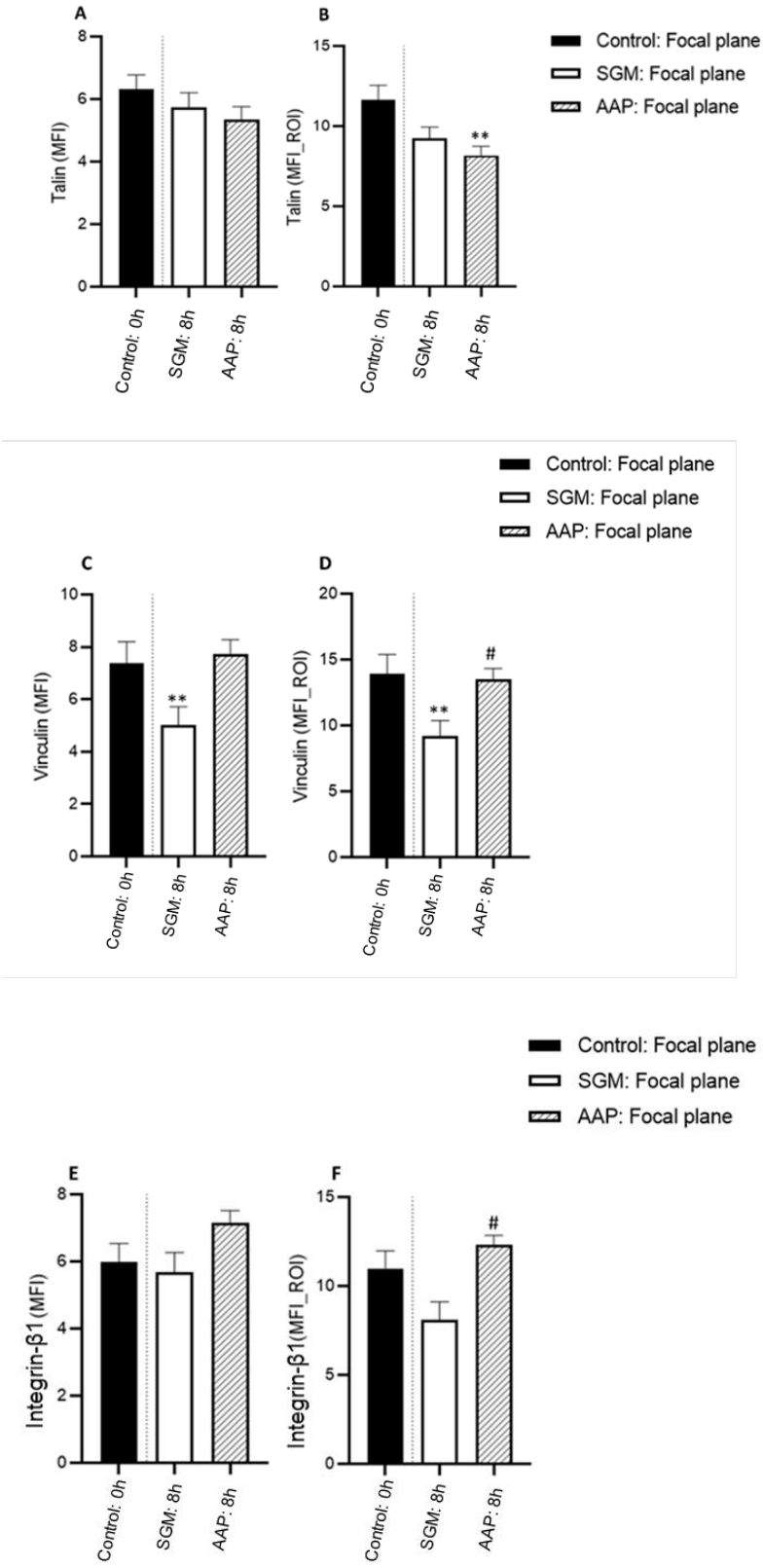


**Figure 5.3.3 Expressed Proteins assessed with MFI: (A)** ROI Absent **(B)** ROI Present**.** Exploration was on a single plane (Focal Plane) for talin, vinculin and integrin-β1 expression. Values were expressed as mean±SD. *Statistical analysis*: Tukey's multiple comparisons test. **p<0.01 difference from control and #p<0.05 difference between AAP and SGM

Data analysis and quantification of the proteins of interest was further extended to planes below and above the Focal Plane. The analysis of more focal planes clarified whether proteins were in the level of involvement in cell adhesion or occurring higher in the cytoplasm. Figure 5.3.5 indicates the protein expression using MFI from varying planes: Focal Plane, Below and Above Plane.

*Focal Plane vs Below Plane:* The Below Plane served as a reference point in relation to the Focal Plane. The inclusion of this plane ensured the following plane (Focal Plane) to be the first in-focus level of the Z-stack imaged. The data for this below plane is included in the graphs as reference to illustrate that it cannot be accurately quantified. All treatment groups showed a significant difference for all expressed proteins in the Focal Plane compared to the Plane Below, as the Plane Below was the level of the coverslip with little to no signal, except integrin-β1 SGM migrating cells.

*Focal Plane vs Above Plane:* Talin expression in non-migrating cells, in contrast to vinculin (13.9±9.7 and 17.6±13.11) ($p=0.0049$) and integrin-β1 (11.5±7.1 and 13.9±9.9) ($p=0.0075$) expression, indicated no significant differences within the planes. Interestingly, the planes in question for SGM migrating cells did not yield significant results for all expressed proteins. AAP treated migrating cells for all the expressed proteins indicated a significant difference between focal plane and above plane.

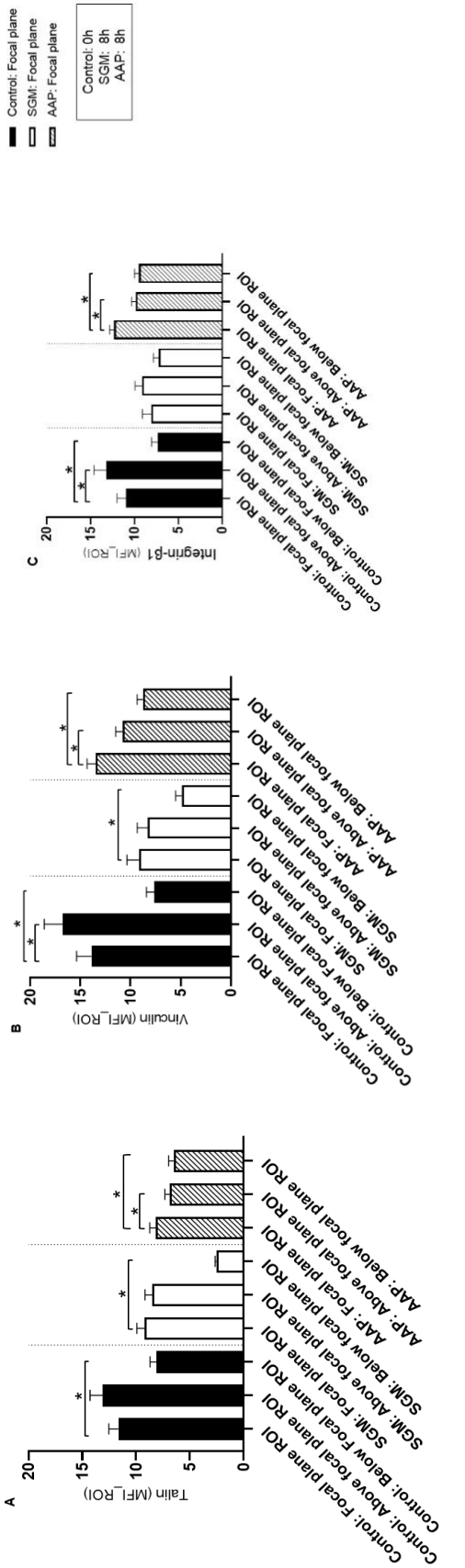


**Figure 5.3.4 Expressed Proteins assessed with MFI on varying planes: Focal, Above and Below Plane** with ROI. Quantified proteins were **(A)** Talin, **(B)** Vinculin **(C)** Integrin-β1. Treatment groups: Control (SGM at 0h) (non-migrating), SGM (at 8h) (migrating) and AAP treated media (at 8h) (migrating). Values were expressed as mean±SD. *Statistical analysis:* ANOVA with Dunnett's multiple comparisons test with significance set at $p<0.05$.

Taken together these results highlight the importance of selecting the appropriate image analysis and data quantification strategy as the results can be significantly altered depending on the approach used.

*5.3.2 Protein Co-localization*

For co-localization analysis two parameters were determined, (1) co-occurrence with Mander's coefficients, an indication of the percentage of total signal from one channel overlapping with signal from another channel (tM1) and vice versa (tM2) (overlap measurement of various signals i.e., proteins) and (2) Pearson's correlation coefficient indicating the relationship between the overlapping signals i.e., proteins.

*Vinculin and Talin:*

*Mander's Coefficient:* 40% of vinculin co-occurred with talin (tM1) in Control and SGM, while 45% co-occurrence was observed in AAP treated media. 25% of expressed talin in Control co-occurred with vinculin while 30% in both SGM and AAP treated media co-occurred with vinculin (tM2) (Fig. 5.3.7).

*Pearson's Coefficient:* Vinculin and talin indicated no significant correlation between the treatment groups with Pearson's R <20% for a set threshold (and R <40% for no set threshold) (Fig. 5.3.8).

The analysis conducted on ROI selected data indicated no significant differences. Figure 5.3.9 illustrates image correlation analysis scatterplots generated from data analysis with and without a ROI.

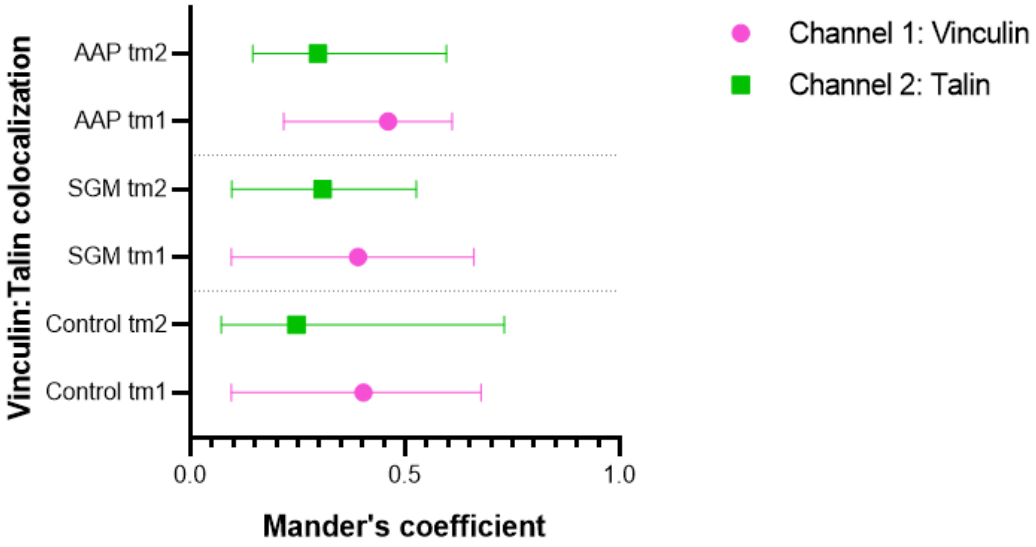


**Figure 5.3.6 Vinculin and Talin co-occurrence test.** Analysis was conducted on Focal Plane of all treatment groups (Control, SGM, AAP treated media) with ROI. Tm1: Vinculin with Talin co-occurrence; Tm2: Talin with Vinculin co-occurrence. Mander's range: 0 – 1; where 0.5 = 50% colocalization from both proteins of interest.

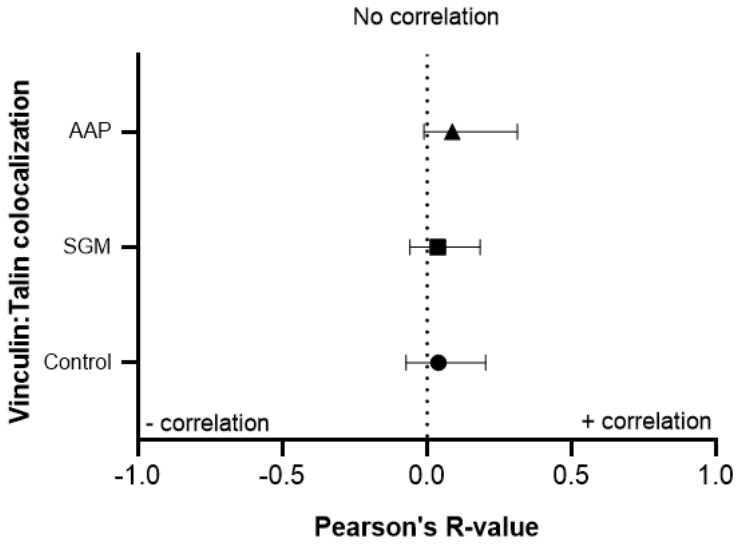


**Figure 5.3.7 Vinculin and Talin correlation test.** Analysis was conducted on Focal Plane for all treatment groups (Control, SGM, AAP treated media) with ROI. Pearson's range: -1 – 1; where 0 = no significant correlation.

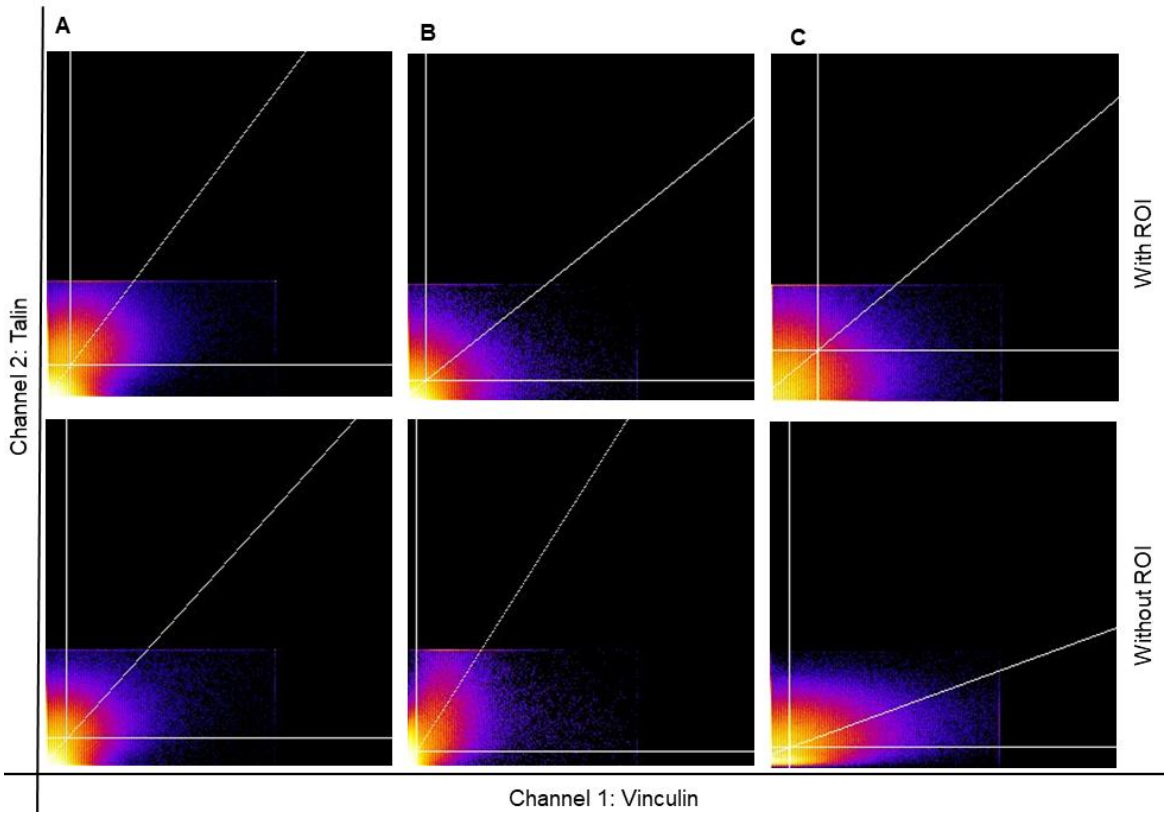


**Figure 5.3.8 Talin and Vinculin co-localization scatterplots** with and without ROI. Generated images are: **(A)** SGM at 0h (Control) **(B)** SGM at 8h **(C)** AAP at 8h produced with the Colocalization Threshold Plugin, FIJI.

*Talin and Integrin-β1:*

*Mander's Coefficient:* Approximately 55% of integrin-β1 co-occurred with talin (tM2) in all groups while talin co-occurrence with integrin-β1 (tM1) decreased in SGM migrating (8h) to 40% and AAP treated media to 45%. Talin interaction with integrin-β1 in migrating cells indicated a decreased in reference to non-migrating cells (Fig. 5.3.10).

*Pearson's Coefficient:* Interactions indicated a correlation of less than 25% between the groups (Fig. 5.3.11). As with the scatterplots accompanying the previous data, no significant differences with or without a selected ROI were found (Fig. 5.3.10).

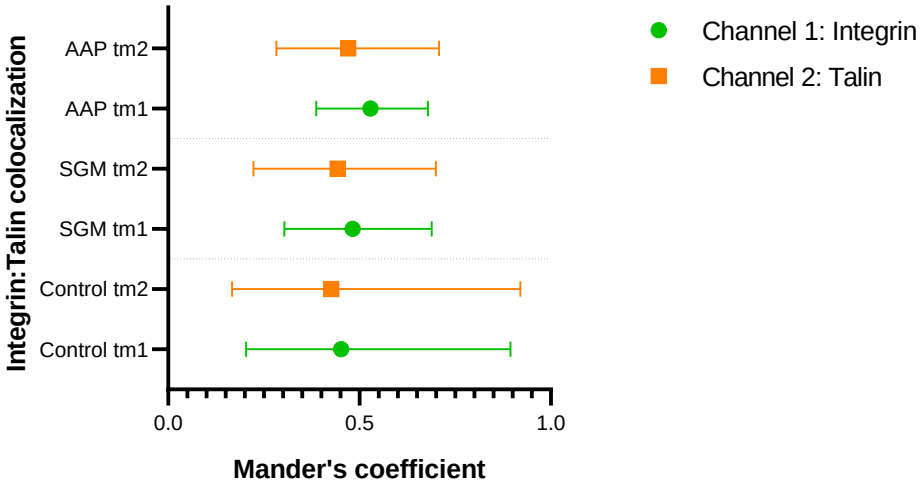


**Figure 5.3.5 Talin and Integrin-β1 co-occurrence test.** Analysis was conducted on Focal Plane of all treatment groups (Control, SGM, AAP treated media) with ROI. Tm1: integrin-β1 with Talin co-occurrence; Tm2: Talin with integrin-β1 co-occurrence. Mander's range: 0 – 1; where 0.5 = 50% colocalization from both proteins of interest.

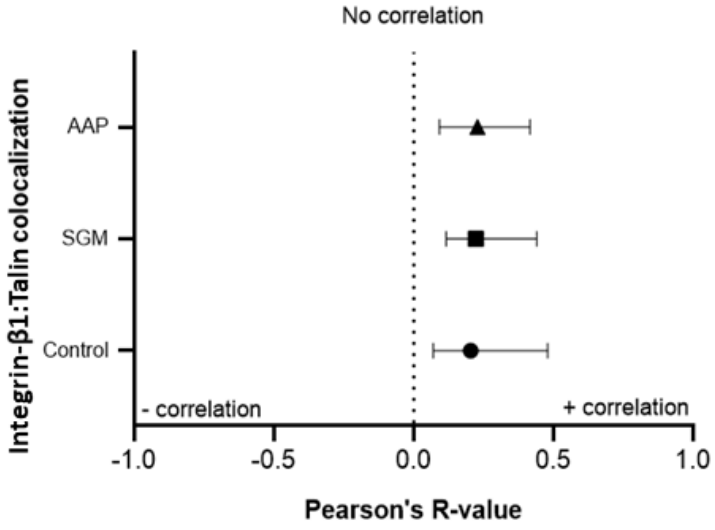


**Figure 5.3.10 Integrin-β1 and Talin correlation test.** Analysis was conducted on Focal Plane of all treatment groups (Control, SGM, AAP treated media) with ROI. Pearson's range: -1 – 1; where 0 = no significant correlation.

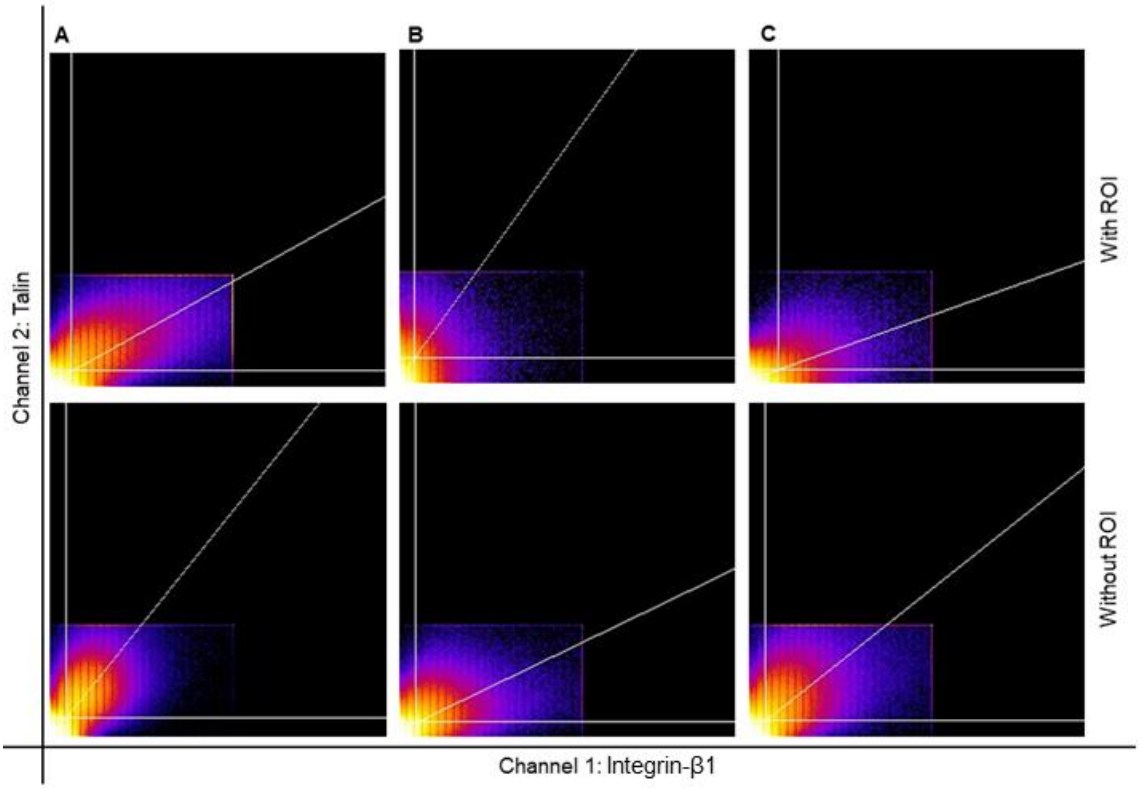


**Figure 5.3.11 Talin and Integrin-β1 co-localization scatterplots** with and without ROI. Generated images are: **(A)** SGM at 0h (Control) **(B)** SGM at 8h **(C)** AAP at 8h produced with the Colocalization Threshold Plugin, FIJI.

*Vinculin and Integrin-β1*

*Mander's Coefficient:* Vinculin co-occurrence with integrin-β1 (tM1) was 40% in the Control, 35% in SGM and 45% in AAP treated media. 20% integrin-β1 co-occurrence with vinculin (tM2) in Control while in SGM and AAP treated media 35% and 40% of integrin-β1 co-occurrence was observed respectively (Fig. 5.3.13).

*Pearson's Coefficient:* Vinculin and integrin-β1 show little significant correlation between the treatment groups, as Pearson's R <15% (Fig. 5.3.14).

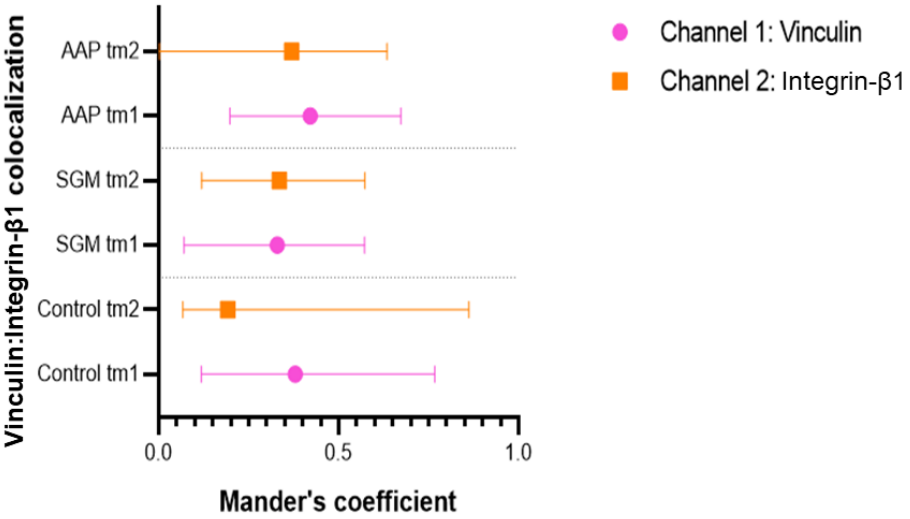


**Figure 5.3.12 Vinculin and Integrin-β1 co-occurrence test.** Analysis was conducted on Focal Plane of all treatment groups (Control, SGM, AAP treated media) with ROI. Tm1: Vinculin with Talin co-occurrence; Tm2: Talin with Vinculin co-occurrence. Mander's range: 0 – 1; where 0.5 = 50% colocalization from both proteins of interest

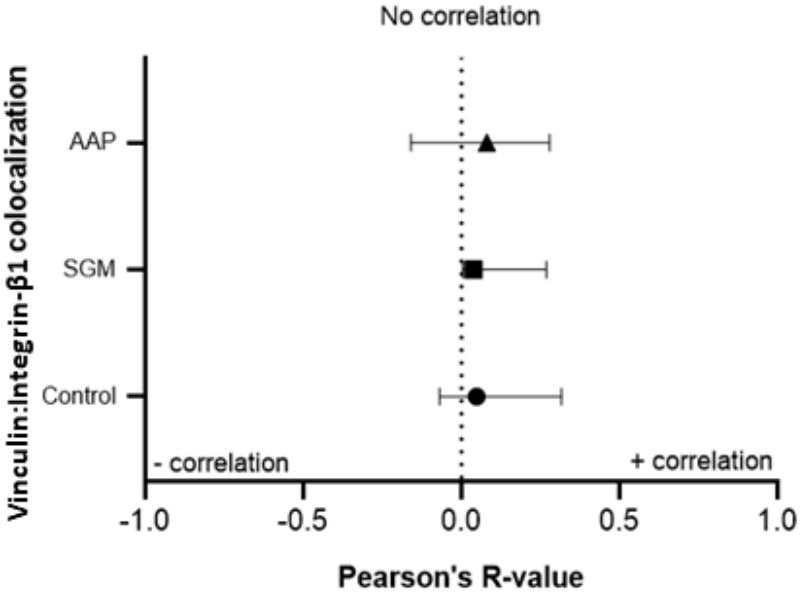


**Figure 5.3.13 Vinculin and Integrin-β1 correlation test.** Analysis was conducted on Focal Plane of all treatment groups (Control, SGM, AAP treated media) with ROI. Pearson's range: -1 – 1; where 0 = no significant correlation.

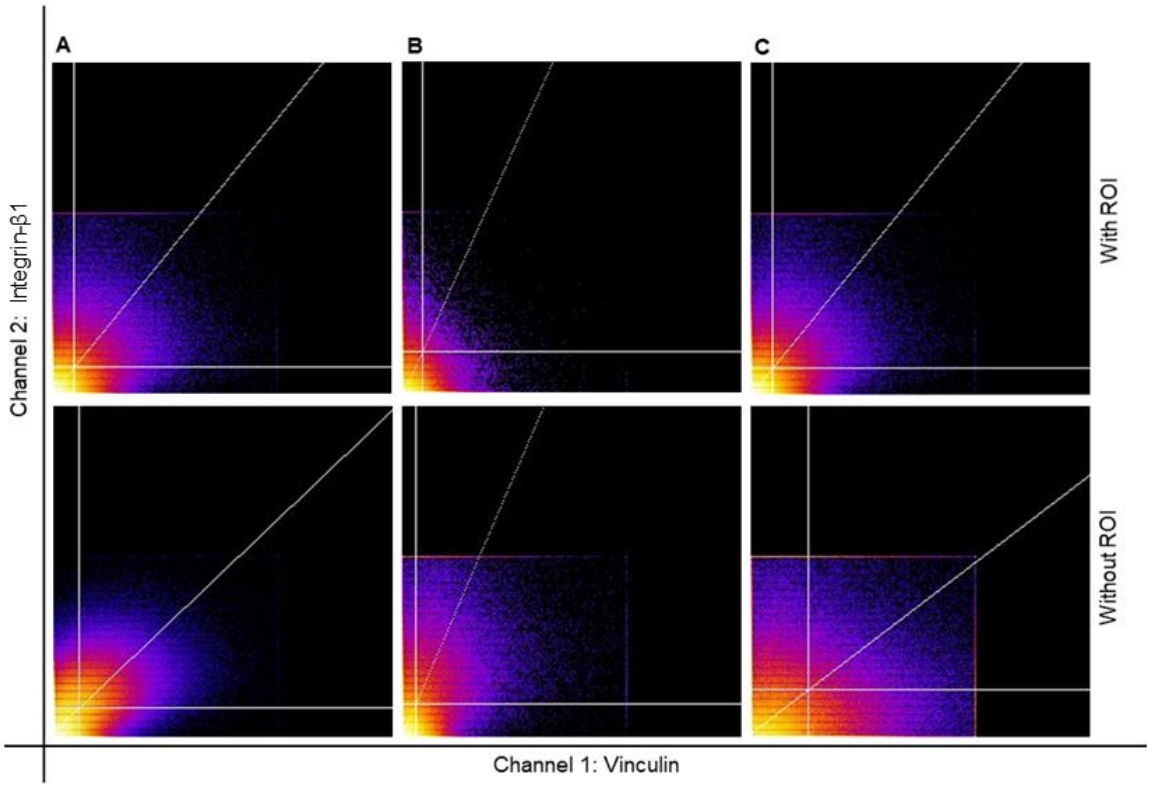


**Figure 5.3.14 Talin and Integrin-β1 co-localization scatterplots** with and without ROI. Generated images are: **(A)** SGM at 0h (Control) **(B)** SGM at 8h **(C)** AAP at 8h produced with Colocalization Threshold Plugin

## 5.4 Super Resolution (SRM): Assessing expressed proteins of interest with TIRF and STORM.

TIRF and STORM were overlayed in several experiments to image talin in SGM and AAP treated migrating cells. The individual configurations were initially optimized separately before the tandem combination. SRM talin (Alexa Fluor 488) imaging was ideal compared to vinculin or integrin-β1. Alexa Fluor 488 optimization was effortless thereby saving time and resources while in contrast Alexa Fluor 647 (vinculin) and Alexa Fluor 555 (integrin-β1) did not produce high signals and bleached immediately when exposed to SRM lasers.

*TIRF*

TIRF yielded images with improved resolution in the Z-dimension in comparison to images acquired with EPI illumination as seen in Figure 5.4.1. TIRF reduced out of focus light, as noted by the diminished nucleus, and improved filament structure resolution. In all TIRF acquired images FA complexes, on the Focal Plane (on coverslip), were clearly visible and emphasized compared to EPI illumination mode. Migrating cells (8h) in SGM indicated less defined FA complexes compared to AAP treated media. Interestingly, as depicted in Figure 5.4.1A-C control (non-migrating cells) showed more distinct FA complexes and generated images with greatly reduced noise compared to SGM migrating cells (8h). In subsequent experiments TIRF and STORM was combined, unlike Figure 5.4.2 that illustrates TIRF imaging separately. Ideally the pathway to generating STORM images would be: EPI illumination (locate cells), TIRF (determine angle), and STORMTIRF combined. However, due to quick photobleaching the TIRF step in the pathway was not completed, in that a TIRF image was not taken only the TIRF angle was determined to use in the next step of STORMTIRF. The exclusion of additional laser activation steps TIRF image acquisition preserved the signal.

The analysis of FA complexes is illustrated in Figure 5.4.3. The length, area, breadth, and perimeter of FA complexes imaged in SGM and AAP treated migrating cells were significantly dissimilar. AAP treated migrating cells had prominent identifiable FA complexes while the SGM treatment group had close to no FA complexes detected even in EPI illumination mode. TIRF images of migrating cells in SGM did not successfully reduce out of focus light as the nucleus was still identified in images. Non-migrating cells relative to AAP treated migrating cells had shorter FA length (Fig.5.4.3 A-B). Non-migrating cells indicated a significant difference in breadth and perimeter compared to SGM and AAP treated media respectively (Fig.5.4.3 C-D). The resulting shape factor of FA from the different treatment groups were the same with no significant differences.

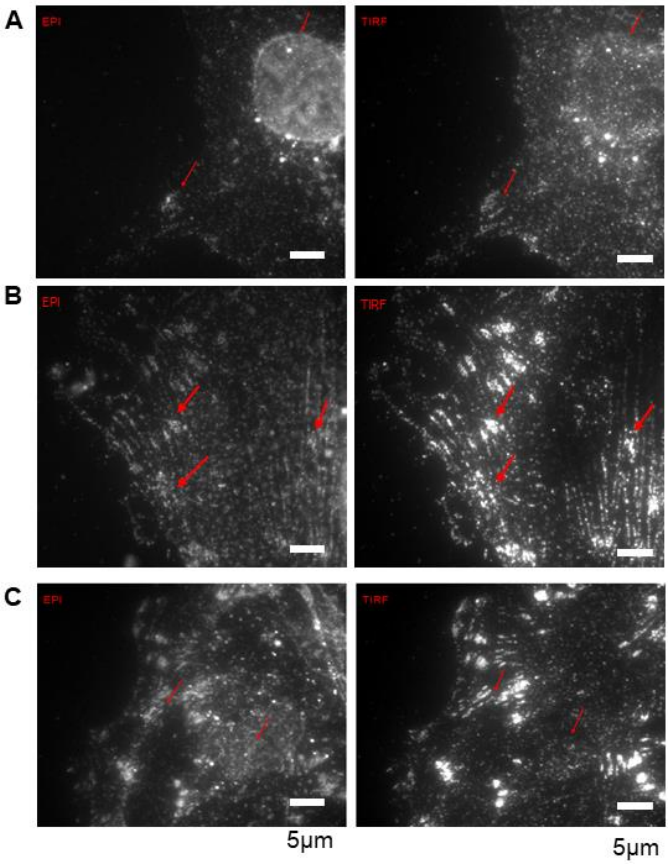


**Figure 5.4.1 Comparative Image Acquisition modes: EPI and TIRF Illumination. (A)** SGM and **(B)** AAP treated media migrating cells (8h) compared to **(C)** non-migrating cells (0h). **Arrows** indicate improved contrast of structure and out of focus light reduction. Scale bar set at 5µm.

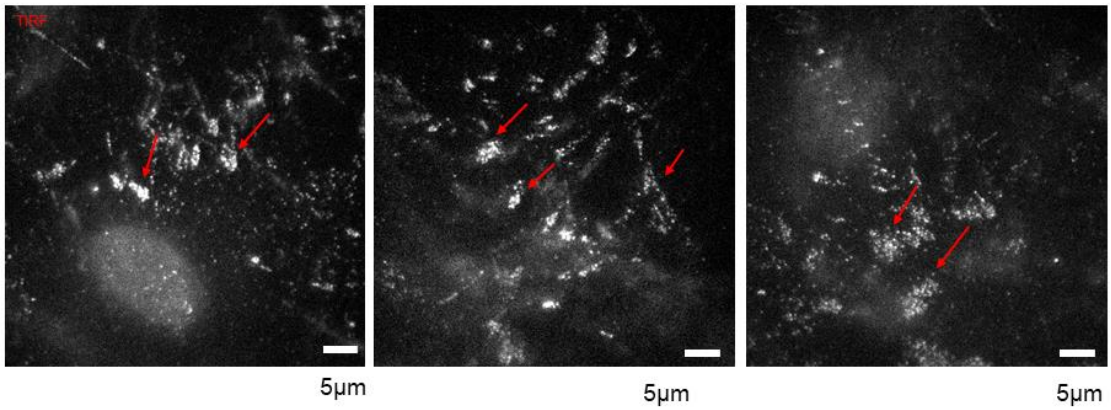


**Figure 5.4.2 Generated TIRF images.** TIRF imagining on AAP treated cells at 8h migrating cells. **Arrows** indicate improved contrast of structure, background and out of focus light reduction. Scale bar set at 5µm.

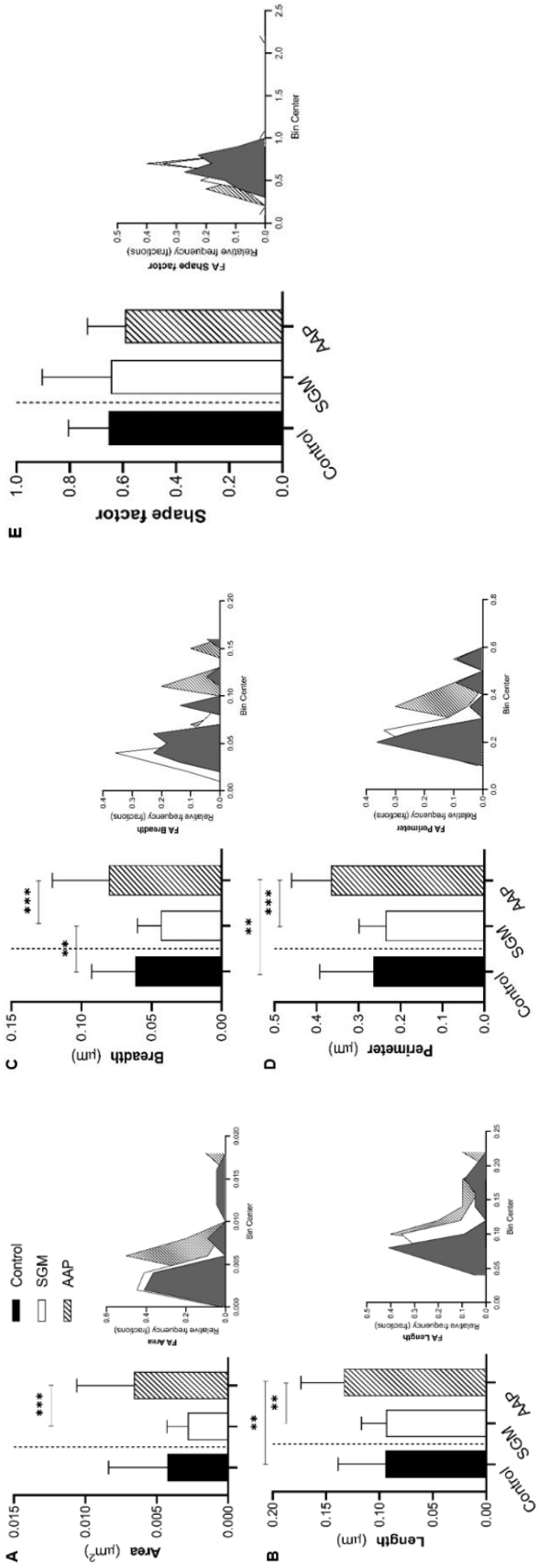


**Figure 5.4.3 FA complexes analysis. (A)** Area, **(B)** Length, **(C)** Breadth, **(D)** Perimeter and (E) Shape Factor were considered for images FA complexes. One Way ANOVA with Tukey post hoc test.

*STORM overlayed with TIRF*

High-precision molecular localization was enabled with STORM configuration acquisition. Subsequent imaging of STORM was overlayed with TIRF to reduce background noise and refine the final constructed image with the additional assistance of post-processing ThunderSTORM functions.

Talin in non-migrating cells FA complexes were imaged with STORM (and TIRF) in Figure 5.4.5. As observed the TIRF defined FA were not constructed appropriately with STORM (with TIRF) hence structure resolution was not distinct. Similarly, SGM and AAP supplemented media final STORM images did not provide clear, resolvable talin filamentous structures (Fig. 5.4.6 – Fig.5.4.7).

The significance of the STORM generated data was referenced to the Control data analysis (Fig.5.4.7) used to determine the baseline for technical artifacts. The generated STORM data did not further expand on the TIRF images acquired. The image reconstruction was not successful. The supporting graphs indicating uncertainty, background, intensity, and sigma distribution indicated peak areas. The distributions showed the blink distributions i.e., the peak distribution in Intensity graph is the brightest, and with the assistance of the optimal uncertainty distributions plots can be altered to reconstruct high-quality images.

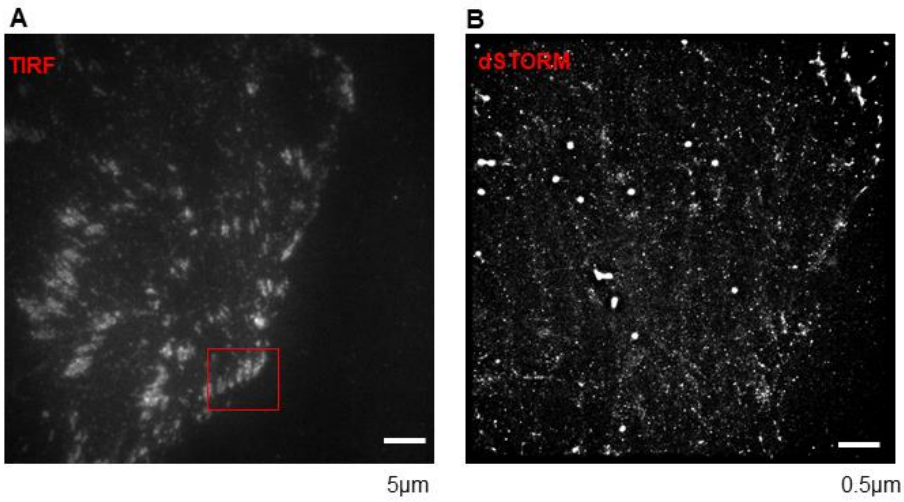


**Figure 5.4.4 Talin detection in non-migrating cells FA. (A)** TIRF and **(B)** STORM with TIRF (unprocessed). Scale bar 5µm and 0.5µm

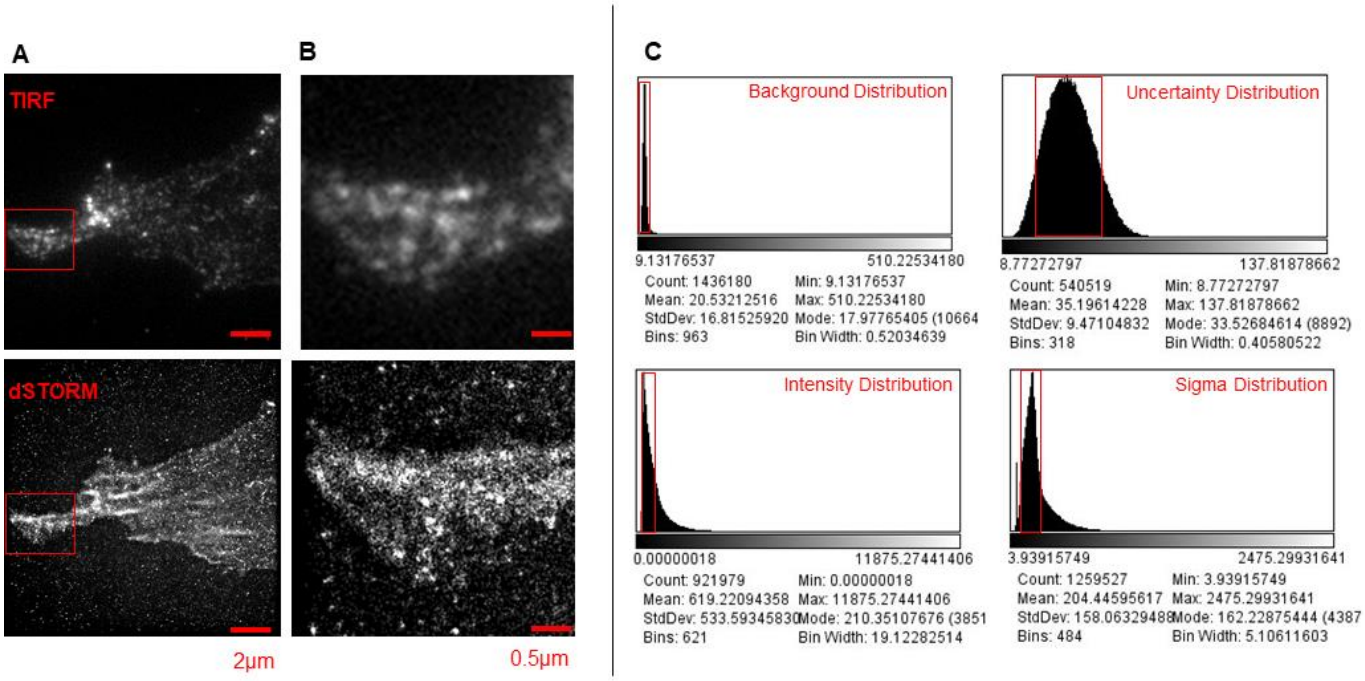


**Figure 5.4.5 STORM imaging in SGM. (A)** TIRF vs dSTORM with TIRF (unprocessed) images. **(B)** Magnified version of (A), however with dSTORM processed. **(C)** The post-processing functions applied to dSTORM raw data. *Histograms*: Background > 12.7742 & Background< 22.6608. Intensity > 172.105 & intensity < 554.562. Sigma > 60.1064 & sigma < 233.714. Uncertainty > 23.7875 & uncertainty < 43.6720. Scale bar 2µm and 0.5µm

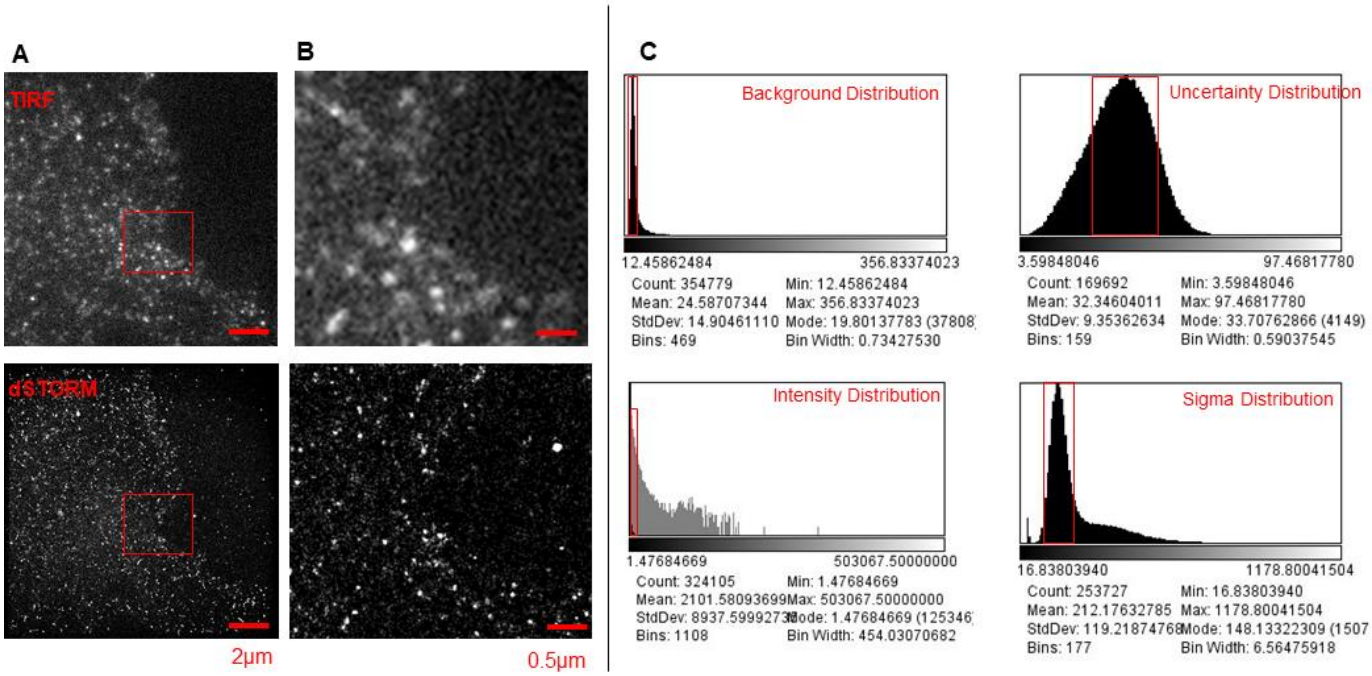


**Figure 5.4.6 STORM imaging in AAP treated media. (A)** TIRF vs dSTORM with TIRF (unprocessed) images. **(B)** Magnified version of (A), however with dSTORM processed. **(C)** The post-processing functions applied to dSTORM raw data. *Histograms*: Background > 15.0 & background < 35.0. Intensity > 300.0 & intensity < 35000.0. Sigma > 102.180 & sigma < 213.781. Uncertainty > 17.1771 & uncertainty < 43.1536. Scale bar 2µm and 0.5µm.

# Chapter 6: Discussion

The purpose of this research project was to investigate the effect of AAP treatment, known to promote collagen deposition in the ECM, on the expression patterns of adhesion proteins during cellular migration whilst optimising advanced microscopy techniques. The optimal AAP concentration was supplemented in migrating MSCs and thereafter pseudopodia was visualized at 8h post migration. The response of the expressed adhesion proteins (talin, vinculin and integrin-β1) in AAP treated migrating cells was quantitatively assessed with confocal imaging. Furthermore, TIRF microscopy enabled the analysis of adhesion protein complexes, FA complexes, of migrating cells in collagen enhanced matrix. This research thus provided valuable insight and a solid foundation for future more in-depth studies to build on.

The dose response data (crystal violet staining) indicated that low concentrations of AAP (0.15mM-1.2mM) could maintain cell viability to a similar extent as SGM over a period of 6 days, whereas a higher concentration (2.4mM) was cytotoxic. This is consistent with previous observations from our laboratory utilizing the same MSC line showing that 0.6mM AAP improves MSC proliferation (BrdU incorporation) under standard culture conditions (Azar *et al.,* 2018). When confluent MSCs do however have contact inhibition and due to their stemness, increased collagen deposition within the ECM together with a high cell density, can trigger spontaneous osteogenic differentiation (Azar *et.al,* 2020). In this study we therefore opted to use the slightly lower AAP concentration (0.6mM) to avoid spontaneous differentiation since a confluent monolayer of cells was required for the migration assays.

AAP is well-known to stimulate collagen production and deposition in the ECM (Hata & Senoo, 1989; Philips *et al.,* 1994; Pullar *et al.,* 2017). Collagen deposition remodels the ECM and enhances adhesion molecule recruitment into FA complexes (Kleinman *et al.,* 1981). In this study we did however not assess the extent of collagen production, although cell migration as assessed by wound closure was investigated since it is a cellular functional parameter which is associated with the composition of the ECM. Differences were observed with regards to the rate of wound (cell-free gap) closure during the migration assay (with and without APP treatment). Wound closure in AAP supplemented media was noted to occur after 24h while SGM occurred after 20h. The latter seemingly contradicts literature but on the contrary: The increased collagen production leads to enhances formation of FA sites thereby slowing down migration in the matrix while it is early to observe an increase in cell growth for the cell line at hand. The wound closure was determined with the migrating cell front using FIJI freehand tool. A concern with this type of assays is that proliferation might occur in conjunction with migration giving a false positive result. Mit. C addition, an inhibitor of proliferation, allow for the investigation of cell migration isolated from the process of proliferation (Glenn *et al.,* 2016). There was already a significant difference in percentage wound closure between SGM with and without mitomycin C at 12 hours, which indicates that wound closure in the absence of Mit. C is somewhat influenced by cell proliferation. The presence of pseudopodia, or elongated cell protrusions, act as an indication of active cell retraction and extension or migration (Petrie & Yamada, 2012). This indicates that cells were indeed migrating to close the cell free gap instead of proliferating. This was further substantiated with cell tracking which indicated

linear migration of single cells. Confluent stem cells have contact inhibition which stops proliferation (Pavel *et al.*, 2018; Leontieva *et al.,* 2014). Moreover at 8h migration time point proliferation should not have played such a significant role, since it is before the expected population doubling time. For the C3H10T1/2 MSC line proliferation occurs at cycles of 24h with slight variation because of the environment (Tang *et al.,* 2004). Nonetheless, only cells with distinct pseudopodia (indication of cell migration) were considered in this study.

Subsequently, confocal microscopy studies assessed the effect of AAP on the expression of adhesion proteins during cell migration with an optimized protocol generating clear cellular structures, with very little background noise. In this study, when referring to MFI, separate levels of a Z-stack were considered to quantify protein expression, while reference to MIP considers all the intensities in an acquired Z-stack as projected in one plane. The MIP data indicated that there is an overall decrease in the expression of adhesion proteins throughout the cell during migration in comparison with non-migrating (control) cells and that AAP treatment did not affect this overall expression. This was consistent for all three proteins of interest (Talin, Vinculin, Integrin β1). The vinculin was mainly centralized around the nucleus, while talin and integrin-β1 were in proximity and co-occurred in the cytoplasm. The adhesion proteins do however form FA complexes on the level of the plasma membrane immediately above the coverslip. To accommodate the 3D natural environment cells inhabit, three focal planes (*Focal Plane, Below Plane, Above Plane*) were subsequently analysed using MFI to provide insight to the expressed protein distributions. The *Below Plane* was out of focus with low signal contrast to the other planes as this level is most likely in the cover slip on which the cells grow. As the focus moved into the cell with increasing levels, the signal intensified. On the focal plane of interest at the level of the plasma membrane immediately above the coverslip (*Focal plane with ROI*), there was significantly less Vinculin and Integrin-β1 expressed in migrating cells in standard growth media compared to AAP treatment. This could potentially be related to the reduced migration rate evident with AAP treatment and warrants further investigation.

Multi-colour confocal imaging provided an opportunity to visualize these proteins in combination to determine any potential changes in protein interactions. This was done by determining protein co-occurrence (spatial overlap between proteins) and co-localization (the degree the overlapping proteins are related to each other) patterns drawn from the multi-colour images. Colocalization investigation provided insight into molecule/proteins interactions (Aaron *et al.,* 2018; Hoffman, 2005). Nearly 55% of integrin-β1 in all treatment groups co-occurred with talin while talin co-occurrence with integrin-β1 reduced by 15% and 10% in SGM and AAP treated media in migrating cells, respectively. The regulated modes of activation for integrin-β1 utilize FAK and talin as the main activators intracellularly. Talin has been described as a master adhesion protein with many binding partners and activators in FA accumulation (Nayal *et al.,* 2004). Mouse models with talin knockouts indicate severe phenotypic effects, inhibiting talin-integrin-β1 interactions and consequently migration (Klapholz *et al.,* 2017; Conti *et al.,* 2009; Calderwood *et al.,* 2013; Brown *et al.,* 2002). The expressed vinculin co-occurred with talin both in SGM and AAP treated media up to 40% and 45% respectively. However, of the total talin less than 20% co-occurred with vinculin. Intriguingly, vinculin co-occurred with integrin-β1 in the same

proportions as talin co-occurrence. Notably vinculin can bind directly or indirectly to integrin-β1 (and other binding partners) hence the illusive nature of determining direct co-occurrence between these proteins (Carisey & Ballestrem, 2011; Ji *et al.,* 2008). These findings suggested that during cell migration the recruiting of vinculin as one of the key migrating proteins supported talin conformational change for the recruitment of additional adhesion proteins reinforcing FA complexes. Vinculin expression in SGM (MFI 9.1±7.7) migrating cells was significantly reduced in contrast to non-migrating cells (MFI 13.9±9.6; $p<0.01$) assessed with MFI (with ROI). However, AAP treatment had no significant changes (MFI 13.5±5.4). Inversely, vinculin reduction in migrating cells compared to non-migrating cells was contrary to known literature. Perhaps the elusive nature of vinculin activation and binding could be attributed to this variation, or vinculin turnover. FA turnover refers to the dynamic changes FA proteins undergo constantly and is comprises of three stages: FA assembly, disassembly, and intermediate phase of intensity fluctuations (Saunders *et al.,* 2006; Stehbens & Wittmann, 2014). The decrease in vinculin could be a result of intensity of fluctuations during FA proteins turnover, supplementary analysis would be followed to substantiate the hypothesis. Nonetheless, all the expressed proteins in AAP treated migrating cells indicated a significant difference in Focal Plane and Above Plane. In literature it is however known that migrating cells possess more FA complexes due to substrate remodelling (Kim, *et al.,* 2013; Trepat *et al.,* 2012). However, adhesion proteins constantly recycle, and quantified data is highly dependent on the association or dissociation stage of leading and lagging fronts during migration (De Pascalis & Etinne-Manneville, 2017; Liang *et al.,* 2017).

The AAP effect on migration in this study was further assessed with TIRF imaging. To reiterate, AAP addition in cell culture enhances collagen and consequently ECM stiffness. It has been reported that an increase in the external stiffness will lead to the recruitment of additional adhesion proteins thereby increasing the size of FA complexes (Fujisawa *et al.,* 2018; Jansen *et al.,* 2017). In literature, the effects of an increase in collagen fibres and matrix stiffness on cell migration (and subsequent FA expression) has been investigated with multiple models including breast carcinoma cells (MDA-MB-231). These cells suspended in an enhanced collagen ECM allowed to migrate for 3 days in 3D microchannel array. Cell counting after migration indicated a decrease in cell number through the matrix. This slowed migration could also be attributed to a decrease in porosity and increase in cell confinement in the 3D ECM, but it could also be that the increased collagen, hence matrix stiffening, delayed migration due to the presence of numerous sites for cellular adhesion (Sawhney & Howard, 2002; Riching *et al.,* 2015).

In our study, advanced TIRF was done with an optimized protocol including utilizing 4% formaldehyde fixative since this has been reported to cause minimal changes to target proteins which in turn is beneficial for the accurate localisation of fluorophores (Hobro & Smith, 2017). The generated TIRF images eliminated out of focus signal and provided improved contrast and resolution (Mattheyses *et al.,* 2010; Funatsu *et al.,*1995). The improved resolution of FA enabled the analysis of FA complexes. Non-migrating cells did not reveal numerous dense FA structures, as the cells required fewer active adhesion sites. In Talin stained migrating cells the area, length, breadth and perimeter of FA was assessed. AAP treated migrating cells indicated a significant difference in the overall size (area, length, breadth, perimeter) of FA complexes compared to migrating cells in SGM. In comparison of little to no FA

complexes in SGM migrating cells, AAP treated media migration showed distinct and prominent FA complexes. However, the shape factor of FA in migrating cells with or without AAP supplementation did not have significant differences. Additionally, FA in SGM migrating cells were not significantly different with non-migrating cells. FA maturity can be influenced by the ECM stiffness and in turn regulates cell migration (Maheshwari *et al.,* 2000; Katz *et al.,* 2000).

The FA quantification showed more pronounced Talin FAs with AAP treatment suggesting that it might be related to the reduced wound closure rate observed – this observation warrants further investigation. It is however unclear if this is related to increased collagen deposition and ECM stiffness or because of the direct effect of AAP on cells to modulate FA. STORM could be utilized as a supporting methodology to verify TIRF generated results. STORM imaging is advantageous to study dynamic cell signalling occurring below the diffraction limit, especially when overlayed and supported by TIRF (Tam & Merino, 2015; Xu *et al.,* 2018). Unfortunately, in the current study STORM images generated were not a true reflection and did not indicate similar structures observed using TIRF. There are several possible explanations for this that are discussed in the Limitations chapter (Chapter 7).

# Chapter 7: Limitations

The final phase of the study design was assessing the adhesion complexes of interest with STORM. The intention to reveal fine structural changes of talin in the FA complexes of enhanced ECM stiffness could not be completed. The optimisation of the STORM protocol was highly elusive, as the distinct FA structures revealed during TIRF were not evident in the STORM images after image processing. During STORM image acquisition, the blinking of most fluorophores was established, but we observed that signal in the dense/prominent FA complexes were not successfully switched to the dark state during the first rounds of the time lapse and therefore subsequent blinking in these areas were insufficient. Additionally, non-specific signal was observed outside the perimeters of the cells as additional blinks. The migration plate coverslips were cleaned using paper towel and ethanol.

The success of any SR microscopy technique is highly influenced by the optimization of the imaging protocols. Imaging protocols include sample preparation, microscope image acquisition setup and post-processing methodologies.

*Sample Preparations* established the optimal antibody staining procedures to obtain bright signals images with the assistance of appropriate fixatives and imaging buffers for confocal, TIRF and STORM. A commercial STORM buffer was used in this study as it is essential to elicit effective blinking of the fluorophores. Although the commercial STORM imaging buffer has been used successfully at CAF laboratory previously (Lumkwana *et al.,* 2021), it is expensive, only available in small volumes and expires quickly. Additionally, the Ibidi migration dishes requires a large volume of buffer to fill the dish, so a wax pen was used to encircle the cells and keep a small droplet of buffer on the area of cell growth. However, the volume in this encircled area could have been insufficient to establish blinking of all fluorophores in the sample and at times the droplet would spread out practically leaving no buffer on the sample. Therefore, it would be beneficial to make use of the cheaper MEA buffer, which can be made up in the laboratory in larger volumes. However, care should be taken to prevent the MEA buffer to collect water/humid air, as it is hygroscopic and can degrade as already as a powder (Heil, 2019).

*Microscope Image Acquisition* consists of various components that influence the outcome image quality or fluorophore blinking. The microscope laser powers, exposure time and gain in imaging act as the imaging "*holy trinity."* During STORM image acquisition two lasers were used: 488nm (talin excitation laser) and 405nm (violet laser). Dempsey et al. (2011) found that use of the violet laser (405 nm) at a low intensity would reactivate fluorophores in the dark state more effectively. However, the 405nm laser is commonly utilized in fluorophore conjugated secondary antibodies i.e., Alexa Fluor 405-Alexa Fluor 488 conjugate (Xu *et al.,* 2018; Li & Vaughan, 2019) in contrast to single fluorophore utilized in the above-mentioned experiments. Regardless, the combination of the 488nm and 405nm laser did not switch all the fluorophores in the FA complexes to the dark state sufficiently and subsequently needs to be addressed in future studies.

*Post processing methodologies* depended on the selected ThunderSTORM/analysis software parameters. The determination of precise blink localizations regulated the reconstruction of accurate

image. The TIRF generated resolvable images were not reconstructed with STORM. The experimental artifacts halted the accurate blink analysis and furthermore experimental controls for STORM were not resolvable therefore no reference point for the STORM generated data. The background noise posed an issue for STORM, perhaps in future studies a revisit to all imaging protocols and STORM settings could reveal the issue of the unsatisfactory image reconstruction.

# Chapter 8: Conclusion and Future Perspective

In support of our initial hypothesis this study demonstrated that there is a change in the expression patterns of talin, vinculin and integrin-β1 during cellular migration. We furthermore demonstrated that AAP stimulation (collagen deposition within the ECM) reduced the migration rate of MSCs and increased the size of FA complexes. FA complexes comprise of FA proteins that in molecular dynamics, work together, and control mechano-signalling. The expression patterns of talin, vinculin and integrin-β1 were determined with and without 0.6mM AAP supplementation at optimal migration time (8h) in comparison to non-migrating cells (0h). The following distributions were noted: majority of vinculin was centralized around the nucleus, while talin and integrin-β1 seemed to closely localize in the cytoplasm. Interestingly, vinculin expression in AAP treated media localized with talin and integrin-β1 to the same extent. The obtained result was in agreement with the following proposed vinculin activation pathway: Vinculin binds to the talin-integrin-β1 complex and undergoes conformational change allowing additional adaptor protein binding (Hirata *et al.,* 2014; Martino *et al.,* 2018). However, more in-depth investigations are required to confirm this observation.

Collagen stiffness on FA complexes was further investigated with TIRF imaging. AAP treated migrating cells indicated prominent and distinct FA complexes in contrast to SGM migrating cells. Furthermore, AAP treated media FA sizes (area, length, breadth and perimeter) were significantly larger than FA in SGM migrating cells. However, the determined shapes of FA were the same. TIRF imaging verified the results obtained from confocal imaging and analysed the AAP enhanced ECM relationship with FA complexes. The incoming external ECM stimuli resulted in an increase in adhesion sites hence encouraged FA maturation in collagen stiff conditions (Grashoff *et al.,* 2010; Park *et al.,* 2011).

TIRF imaging was sufficient to investigate the adhesion patterns of migrating cells in collagen reinforced media. The reduction of out of focus light and TIRF improved resolution enabled FA clear assessment (Parhamifar & Moghimi, 2012). Therefore, STORM imaging was not essential for the research question at hand. STORM introduced an extra layer of protein assessment in that high precision single molecule localization depth analysis was accomplished, in contrast to limited 100nm distance for TIRF (Hosny *et al.,* 2013). Although optimization of advanced TIRF imaging was successful, further optimization of STORM, specifically image acquisition, analysis and processing is required.

# Chapter 9: Bibliography

Aaron, J. S., Taylor, A. B. and Chew, T. L. (2018) 'Image co-localization - co-occurrence versus correlation', *Journal of cell science*, 131(3). doi: 10.1242/jcs.211847.

Alberts B, Johnson A, Lewis J, et al. (2002) Molecular Biology of the Cell. 4th edition. New York: Garland Science. Integrins. Available from: https://www.ncbi.nlm.nih.gov/books/NBK26867/

Alenghat, F. J. *et al.* (2000) 'Analysis of cell mechanics in single vinculin-deficient cells using a magnetic tweezer.', *Biochemical and biophysical research communications*. United States, 277(1), pp. 93–99. doi: 10.1006/bbrc.2000.3636.

Alfieri, C. *et al.,* (2016) Nature 536, 431- 436.

Anthis, N. J. *et al.* (2009) 'The structure of an integrin/talin complex reveals the basis of inside-out signal transduction', *EMBO Journal*. Nature Publishing Group, 28(22), pp. 3623–3632. doi: 10.1038/emboj.2009.287.

Aoki, Y. *et al.* (2001) 'Evaluation of numerical aperture and focusing characteristics of planar microlens for optical interconnects', *Japanese Journal of Applied Physics, Part 2: Letters*, 40(5). doi: 10.1143/jjap.40.l446.

Atherton, P. *et al.* (2015) 'Vinculin controls talin engagement with the actomyosin machinery', *Nature Communications*. Nature Publishing Group, 6, pp. 1–12. doi: 10.1038/ncomms10038.

Azar, Y. M. *et al.* (2018) 'Antioxidant Preconditioning Improves the Paracrine Responsiveness of Mouse Bone Marrow Mesenchymal Stem Cells to Diabetic Wound Fluid', *Stem Cells and Development*, 27(23), pp. 1646–1657. doi: 10.1089/scd.2018.0145.

Azar, Y. M., Niesler, C. U. and van de Vyver, M. (2020) 'Ex vivo antioxidant preconditioning improves the survival rate of bone marrow stem cells in the presence of wound fluid', *Wound Repair and Regeneration*, 28(4), pp. 506–516. doi: 10.1111/wrr.12815.

Almada, P., Culley, S. and Henriques, R. (2015) 'PALM and STORM: Into large fields and high-throughput microscopy with sCMOS detectors', *Methods*. Elsevier Inc., 88, pp. 109–121. doi: 10.1016/j.ymeth.2015.06.004.

Axelrod, D. (2016) 'Total Internal Reflection Fluorescence Microscopy', *Encyclopedia of Cell Biology*, 2, pp. 62–69. doi: 10.1016/B978-0-12-394447-4.20089-8.

Axelrod D. (2001) Total internal reflection fluorescence microscopy in cell biology. *Traffic*. 2:764–774. [PubMed: 11733042]

Balaban, N. Q. *et al.* (2001) 'Force and focal adhesion assembly: a close relationship studied using elastic micropatterned substrates.', *Nature cell biology*. England, 3(5), pp. 466–472. doi: 10.1038/35074532.

Balda, MS., Matter, K., (2008) Epithelial cell adhesion and the regulation of gene expression. Trends Cell Biol 13: 310 –318.

Bakolitsa, C. *et al.* (1999) 'Crystal structure of the vinculin tail suggests a pathway for activation', *Cell*, 99(6), pp. 603–613. doi: 10.1016/S0092-8674(00)81549-4.

Bates, M., Jones, S. A. and Zhuang, X. (2013) 'Stochastic Optical Reconstruction Microscopy (STORM ): A Method for Superresolution Fluorescence Imaging', pp. 498–521. doi: 10.1101/pdb.top075143.

Betzig, E. *et al.* (2006) 'Imaging Intracellular Fluorescent Proteins at Nanometer Resolution', x(September), pp. 1–5.

Bewersdorf J, Schmidt R, Hell SW. (2006) Comparison of I5M and 4Pi-microscopy. *Microscopy,* 222:105–17. [PubMed: 16774519]

Bonnans, C., Chou, J. and Werb, Z. (2014) 'Bonnans, Caroline Chou, Jonathan Werb, Zena', *Nat Rev Mol Cell Biol*, 15(12), pp. 786–801. doi: 10.1038/nrm3904.Remodelling.

Berod, A. and Pujol, F. (1981) 'Importance of Fixation in Immunohistochemistry', pp. 844–850.

Boyera, N., Galey, I. and Bernard, B. A. (1998) 'Effect of vitamin C and its derivatives on collagen synthesis and cross-linking by normal human fibroblasts.', *International journal of cosmetic science*. England, 20(3), pp. 151–158. doi: 10.1046/j.1467-2494.1998.171747.x.

Brown, N. H. *et al.* (2002) 'Talin is essential for integrin function in Drosophila.', *Developmental cell*. United States, 3(4), pp. 569–579. doi: 10.1016/s1534-5807(02)00290-3.

Burridge, K. (2017) 'Focal adhesions: a personal perspective on a half century of progress', 284, pp. 3355–3361. doi: 10.1111/febs.14195.

Cabriel, C. *et al.* (2019) *Combining 3D single molecule localization strategies for reproducible bioimaging*.

Calderwood, D. A., Campbell, I. D. and Critchley, D. R. (2013) 'Talins and kindlins: partners in integrin-mediated adhesion.', *Nature reviews. Molecular cell biology*, 14(8), pp. 503–517. doi: 10.1038/nrm3624.

Cary, L.A., Chang, J.F., Guan, J.L. (1996) Stimulation of cell migration by overexpression of focal adhesion kinase and its association with Src and Fyn, J. Cell Sci. 109 (Pt 7) 1787–1794

Cary, L.A., et al., (1998) Identification of p130Cas as a mediator of focal adhesion kinase promoted cell migration, J. Cell Biol. 140 (1) 211–221.

Carisey, A. and Ballestrem, C. (2011) 'Vinculin, an adapter protein in control of cell adhesion signalling.', *European journal of cell biology*, 90(2–3), pp. 157–163. doi: 10.1016/j.ejcb.2010.06.007.

Cavey, M. and Lecuit, T. (2009) 'Molecular bases of cell-cell junctions stability and dynamics.', *Cold Spring Harbor perspectives in biology*, 1(5), p. a002998. doi: 10.1101/cshperspect.a002998.

Chattopadhyay, S. and Raines, R. T. (2014) 'Review collagen-based biomaterials for wound healing.', *Biopolymers*, 101(8), pp. 821–833. doi: 10.1002/bip.22486.

Chen, X., Zheng, B. and Liu, H. (2011) 'Optical and digital microscopic imaging techniques and applications in pathology', *Analytical Cellular Pathology*, 34(1–2), pp. 5–18. doi: 10.3233/ACP-2011-0006.

Chen, B. H. *et al.* (2002) 'Roles of Rho-associated kinase and myosin light chain kinase in morphological and migratory defects of focal adhesion kinase-null cells', *Journal of Biological Chemistry*. © 2002 ASBMB. Currently published by Elsevier Inc; originally published by American Society for Biochemistry and Molecular Biology., 277(37), pp. 33857–33863. doi: 10.1074/jbc.M204429200.

Choi, K. M. *et al.* (2008) 'Effect of ascorbic acid on bone marrow-derived mesenchymal stem cell proliferation and differentiation', *Journal of Bioscience and Bioengineering*, 105(6), pp. 586–594. doi: 10.1263/jbb.105.586.

Cram, E. J., Clark, S. G. and Schwarzbauer, J. E. (2003) 'Talin loss-of-function uncovers roles in cell contractility and migration in C. elegans', *Journal of Cell Science*, 116(19), pp. 3871–3878. doi: 10.1242/jcs.00705.

Cremer, C. and Masters, B. R. (2015) 'PHYSICAL J OURNAL H Resolution enhancement techniques', (April 2013). doi: 10.1140/epjh/e2012-20060-1.

Conti, F. J. *et al.* (2009) 'Talin 1 and 2 are required for myoblast fusion, sarcomere assembly and the maintenance of myotendinous junctions.', *Development (Cambridge, England)*, 136(21), pp. 3597–3606. doi: 10.1242/dev.035857.

Das, T.; Safferling, K.; Rausch, S.; Grabe, N.; Boehm, H.; Spatz, J. P. A (**2015)** Molecular Mechanotransduction Pathway Regulates Collective Migration of Epithelial Cells. *Nat Cell Biol 17* (3), 276–287. https://doi.org/10.1038/ncb3115.

Davidson, M. W. (2009) 'Ernst Abbe', *Laboratory Medicine*, 40(8), pp. 502–503. doi: 10.1309/lm6yl3shmck6dusm.

Davidson, M. W. (2010) 'Robert Hooke', *Laboratory Medicine*, 41(3), pp. 180–182. doi: 10.1309/lmq8h3hqhzqkeczz.

De Lucas, B., Pérez, L. M. and Gálvez, B. G. (2018) 'Importance and regulation of adult stem cell migration', *Journal of Cellular and Molecular Medicine*, 22(2), pp. 746–754. doi: 10.1111/jcmm.13422.

De Pascalis, C. and Etienne-Manneville, S. (2017) 'Single and collective cell migration: The mechanics of adhesions', *Molecular Biology of the Cell*, 28(14), pp. 1833–1846. doi: 10.1091/mbc.E17-03-0134.

Dempsey, GT. Vaughan, JC. Chen, KH. Bates, M. Zhuang, X. (2011) Evaluation of fluorophores for optimal performance in localization-based super-resolution imaging. Nature Methods 8, 1027–1036 [PubMed: 22056676]

Discher, D. E., Janmey, P. and Wang, Y. (2005) 'Other Cell _2Pdf', 310(NOVEMBER), pp. 1139–1143.Dormann, D. and Weijer, C. J. (2006) 'Imaging of cell migration', *EMBO Journal*, 25(15), pp. 3480–3493. doi: 10.1038/sj.emboj.7601227.

Dumbauld, D. W. *et al.* (2013) 'How vinculin regulates force transmission.', *Proceedings of the National Academy of Sciences of the United States of America*, 110(24), pp. 9788–9793. doi: 10.1073/pnas.1216209110.

Edelblum, K. L.; Turner, J. R.(2015) Epithelial Cells. In *Mucosal Immunology*; Elsevier; pp 187–210. https://doi.org/10.1016/B978-0-12-415847-4.00012-4.

Erickson, C.A. (1990) Cell migration in the embryo and adult organism, Curr. Opin. Cell Biol. 2 (1) 67–74

Ezratty, E. J. *et al.* (2009) 'Clathrin mediates integrin endocytosis for focal adhesion disassembly in migrating cells', 187(5), pp. 733–747. doi: 10.1083/jcb.200904054.

Fang, Y. (2015) 'Total internal reflection fluorescence quantification of receptor pharmacology', *Biosensors*, 5(2), pp. 223–240. doi: 10.3390/bios5020223.

Fackler, O. T.; Grosse, R. **(2008**) Cell Motility through Plasma Membrane Blebbing. *Journal of Cell Biology*, *181* (6), 879–884. https://doi.org/10.1083/jcb.200802081.

Fermor B, Gundle R, Evans M, Emerton M, Pocock A, Murray D. (1998) Primary human osteoblasts proliferation and prostaglandin E2 release in response to mechanical strain in vitro. Bone; 22:637–43

Fili, N. and Toseland, C. (2014) 'Fluorescence and Labelling: How to Choose and What to Do Chapter 1 Fluorescence and Labelling: How to Choose and What to Do', (March 2016). doi: 10.1007/978-3-0348-0856-9.

Fish, K. N. (2015) 'HHS Public Access', (2), pp. 1–21. doi: 10.1002/0471142956.cy1218s50.Total.

Franco, S. J. *et al.* (2004) 'Calpain-mediated proteolysis of talin regulates adhesion dynamics', *Nature Cell Biology*, 6(10), pp. 977–983. doi: 10.1038/ncb1175.

Freundlich, M. M. (1963) 'Origin of the electron microscope', *Science*, 142(3589), pp. 185–188. doi: 10.1126/science.142.3589.185.

Friedl, P.; Wolf, K. (**2003**) Tumour-Cell Invasion and Migration: Diversity and Escape Mechanisms. *Nat Rev Cancer*, *3* (5), 362–374. https://doi.org/10.1038/nrc1075.

Friedl, P. and Wolf, K. (2009). Proteolytic interstitial cell migration: a five-step process. Cancer Metastasis Rev. 28, 129-135.

Fujisawa, K. *et al.* (2018) 'Evaluation of the effects of ascorbic acid on metabolism of human mesenchymal stemmatt cells.', *Stem cell research & therapy*, 9(1), p. 93. doi: 10.1186/s13287-018-0825-1.

Funatsu, T. *et al.* (1995) 'Imaging of single fluorescent molecules and individual ATP turnovers by single myosin molecules in aqueous solution.', *Nature*. England, 374(6522), pp. 555–559. doi: 10.1038/374555a0.

Furuse M, Hirase T, Itoh M, Nagafuchi A, Yonemura S, Tsukita S, Tsukita S. (1993) Occludin: A novel integral membrane protein localizing at tight junctions. J Cell Biol.; 123:1777–1788. [PubMed: 8276896]

Galbraith, C. G. and Galbraith, J. A. (2011) 'ARTICLE SERIES: Imaging Cell Science at a Glance microscopy at a glance'. doi: 10.1242/jcs.080085.

Galbraith, C. G., Yamada, K. M. and Sheetz, M. P. (2002) 'complex development', 159(4), pp. 695–705. doi: 10.1083/jcb.200204153.

Geiger B, Spatz JP, and Bershadsky AD. (2009) Environmental sensing through focal adhesions. Nat. Rev. Mol. Cell Biol.; 10(1):21-33. [PMID: 19197329]

Getsios S, Huen AC, Green KJ. (2004) Working out the strength and flexibility of desmosomes. Nat Rev Mol Cell Biol.; 5:271–281. [PubMed: 15071552]

Garrod D, Chidgey M. (2008) Desmosome structure, composition and function. Biochim Biophys Acta. 1778:572–587. [PubMed: 17854763]

Ghabrial, A. S. and Krasnow, M. A. (2006). Social interactions among epithelial cells during tracheal branching morphogenesis. Nature 441, 746-749

Gingras, A. R. *et al.* (2005) 'Mapping and consensus sequence identification for multiple vinculin binding sites within the talin rod', *Journal of Biological Chemistry*. Â© 2005 ASBMB. Currently published by Elsevier Inc; originally published by American Society for Biochemistry and Molecular Biology., 280(44), pp. 37217–37224. doi: 10.1074/jbc.M508060200.

Gkretsi, V. and Stylianopoulos, T. (2018) 'Cell adhesion and matrix stiffness: Coordinating cancer cell invasion and metastasis', *Frontiers in Oncology*, 8(MAY). doi: 10.3389/fonc.2018.00145.

Glenn, H. L., Messner, J. and Meldrum, D. R. (2016) 'A simple non-perturbing cell migration assay insensitive to proliferation effects', *Scientific Reports*. Nature Publishing Group, 6(August), pp. 1–12. doi: 10.1038/srep31694.

Godin, A. G., Lounis, B. and Cognet, L. (2014) 'Biophysical Review Super-resolution Microscopy Approaches for Live Cell Imaging', *Biophysj*. Biophysical Society, 107(8), pp. 1777–1784. doi: 10.1016/j.bpj.2014.08.028.

Goldmann, W. H. (2016) 'Role of vinculin in cellular mechanotransduction', *Cell Biology International*, 40(3), pp. 241–256. doi: 10.1002/cbin.10563.

Goldmann, W. H. (2002) 'Mechanical aspects of cell shape regulation and signaling.', *Cell biology international*. England, 26(4), pp. 313–317. doi: 10.1006/cbir.2002.0857.

Golji, J., Wendorff, T. and Mofrad, M. R. K. (2012) 'Phosphorylation primes vinculin for activation.', *Biophysical journal*, 102(9), pp. 2022–2030. doi: 10.1016/j.bpj.2012.01.062.

Goult, B. T. *et al.* (2010) 'Structure of a double ubiquitin-like domain in the talin head: A role in integrin activation', *EMBO Journal*, 29(6), pp. 1069–1080. doi: 10.1038/emboj.2010.4.

Grashoff, C. *et al.* (2010) 'Measuring mechanical tension across vinculin reveals regulation of focal adhesion dynamics.', *Nature*, 466(7303), pp. 263–266. doi: 10.1038/nature09198.

Gustafsson, M. G. (1999) 'Extended resolution fluorescence microscopy', *Current Opinion in Structural Biology*, 9(5), pp. 627–628. doi: 10.1016/S0959-440X(99)00016-0.

Gustafsson, M. G. L. (2005) 'Nonlinear structured-illumination microscopy: Wide-field fluorescence imaging with theoretically unlimited resolution', 102(37), pp. 13081–13086.

Gustafsson, M. G. L. (2000) 'Surpassing the lateral resolution limit by a factor of two using structured illumination microscopy'.

Ha, T. and Tinnefeld, P. (2012) 'Photophysics of Fluorescent Probes for Single-Molecule Biophysics and Super-Resolution Imaging', *Annual Review of Physical Chemistry*. Annual Reviews, 63(1), pp. 595–617. doi: 10.1146/annurev-physchem-032210-103340.

Hagen, G. M., Ovesny, M. and Svindrych, Z. (2015) 'ThunderSTORM : Methodology and Algorithms ( update ) Charles University in Prague ThunderSTORM : a comprehensive ImageJ plugin for PALM and STORM data analysis and super-resolution imaging', (October).

Han, D. C. and Guan, J. L. (1999). Association of focal adhesion kinase with Grb7 and its role in cell migration. J. Biol. Chem. 274, 24425-24430.

Han, S. *et al.* (2012) 'Three-dimensional extracellular matrix-mediated neural stem cell differentiation in a microfluidic device.', *Lab on a chip*. England, 12(13), pp. 2305–2308. doi: 10.1039/c2lc21285d.

Hartsock A, Nelson WJ. (2008) Adherens and tight junctions: Structure, function and connections to the actin cytoskeleton. Biochim Biophys Acta. 1778:660–669. [PubMed: 17854762]

Harris, T. J. C. and Tepass, U. (2010) 'Adherens junctions: From molecules to morphogenesis', *Nature Reviews Molecular Cell Biology*. Nature Publishing Group, 11(7), pp. 502–514. doi: 10.1038/nrm2927.

Hata, R. -I and Senoo, H. (1989) 'L-ascorbic acid 2-phosphate stimulates collagen accumulation, cell proliferation, and formation of a three-dimensional tissuelike substance by skin fibroblasts', *Journal of Cellular Physiology*, 138(1), pp. 8–16. doi: 10.1002/jcp.1041380103.

Hauch, K. D. and Ratner, B. D. (2012) *CHAPTER II 3 .8 MICROSCOPY FOR BIOMATERIALS SCIENCE Resolution in Light Microscopy Magnification in Light Microscopy*. Third Edit, *Biomaterials Science: An Introduction to Materials in Medicine*. Third Edit. Elsevier. doi: 10.1016/B978-0-08-087780-8.00058-9.

Haugh, J. M. *et al.* (2000) 'Spatial Sensing in Fibroblasts

Heil, H. S. (2019) 'Sharpening super-resolution by single molecule localization microscopy in front of a tuned mirror Einzelmolekül-Lokalisationsmikroskopie vor einem abgestimmten Spiegel zur Auflösungsverbesserung Submitted by'.

Heilemann, M., van de Linde, S., Schuttpelz, M., Kasper, R., Seefeldt, B., Mukherjee, A., Tinnefeld, P., Sauer, M., van de Linde, S., and Schüttpelz, M. (2008). Subdiffractionresolution fluorescence imaging with conventional fluorescent probes. Angewandte Chemie International Edition, 47:6172–6176.

Heintzmann, R. & Gustafsson, M. G. L. (2009) *Nature Photon.* **3**, 362–364

Heintzmann, R. and Huser, T. (2017) 'Super-Resolution Structured Illumination Microscopy'. doi: 10.1021/acs.chemrev.7b00218.

Hell, S. W., Schmidt, R. & Egner, A. (2009). *Nature Photon.* **3**, 381–387

Hell, S. W. (2003) 'Toward fluorescence nanoscopy', 21(11), pp. 1347–1355. doi: 10.1038/nbt895.

Helmchen, F. and Denk, W. (2005) 'Deep tissue two-photon microscopy', 2(12). doi: 10.1038/NMETH818.

Hirata, H. *et al.* (2014) 'Force-dependent vinculin binding to talin in live cells: A crucial step in anchoring the actin cytoskeleton to focal adhesions', *American Journal of Physiology - Cell Physiology*, 306(6). doi: 10.1152/ajpcell.00122.2013.

Hobro, A. J. and Smith, N. I. (2017) 'An evaluation of fixation methods: Spatial and compositional cellular changes observed by Raman imaging', *Vibrational Spectroscopy*. Elsevier B.V., 91, pp. 31–45. doi: 10.1016/j.vibspec.2016.10.012.

Hoffman, R. M. (2005) 'Advantages of multi-color fluorescent proteins for whole-body and in vivo cellular imaging', *Journal of Biomedical Optics*, 10(4), p. 041202. doi: 10.1117/1.1992485.

Hood, J. D. and Cheresh, D. A. (2002) 'Role of integrins in cell invasion and migration', *Nature Reviews Cancer*, 2(2), pp. 91–100. doi: 10.1038/nrc727.

Horwitz - Asymmetric, J. A. *et al.* (2000) 'Cell migration', 13(19), pp. 756–759.

Hosny, N. A. *et al.* (2013) 'Super-Resolution Imaging Strategies for Cell Biologists Using a Spinning Disk Microscope', *PLoS ONE*, 8(10). doi: 10.1371/journal.pone.0074604.

Hovis, D. B. and Heuer, A. H. (2010) 'The use of laser scanning confocal microscopy (LSCM) in materials science', *Journal of Microscopy*, 240(3), pp. 173–180. doi: 10.1111/j.1365-2818.2010. 03399.x

Huang, B., Bates, M. and Zhuang, X. (2009) 'Super-resolution fluorescence microscopy', *Annual Review of Biochemistry*, 78, pp. 993–1016. doi:

Huang, B., Babcock, H. and Zhuang, X. (2010) 'Primer Breaking the Diffraction Barrier : Super-Resolution Imaging of Cells', *Cell*. Elsevier Inc., 143(7), pp. 1047–1058. doi: 10.1016/j.cell.2010.12.002.

Humphries, J. D. *et al.* (2009) 'Proteomic analysis of integrin-associated complexes identifies RCC2 as a dual regulator of Rac1 and Arf6', *Science Signaling*, 2(87), pp. 1–15. doi: 10.1126/scisignal.2000396.

Humphrey, J. D. *et al.* (2015) 'HHS Public Access', 15(12), pp. 802–812. doi: 10.1038/nrm3896.Mechanotransduction.

Huttenlocher, A. and Horwitz, A. R. (2011) 'CONSELLERIA MEDI AMBIENT.pdf', *Cold Spring Harbor Perspectives*, 3, pp. 1–16. Available at: papers3://publication/doi/10.1101.

Jakobs, S. and Wurm, C. A. (2014) 'Super-resolution microscopy of mitochondria', *Current Opinion in Chemical Biology*. Elsevier Ltd, 20(1), pp. 9–15. doi: 10.1016/j.cbpa.2014.03.019.

Janoštiak, R. *et al.* (2014) 'CAS directly interacts with vinculin to control mechanosensing and focal adhesion dynamics.', *Cellular and molecular life sciences: CMLS*, 71(4), pp. 727–744. doi: 10.1007/s00018-013-1450-x.Janssen, M. E. W. *et al.* (2006) 'Three-dimensional structure of vinculin bound to actin filaments', *Molecular Cell*, 21(2), pp. 271–281. doi: 10.1016/j.molcel.2005.11.020.

Jansen, K. A., Atherton, P. and Ballestrem, C. (2017) 'Mechanotransduction at the cell-matrix interface', *Seminars in Cell and Developmental Biology*. Elsevier Ltd, 71, pp. 75–83. doi: 10.1016/j.semcdb.2017.07.027.

Ji, L., Lim, J. and Danuser, G. (2008) 'Fluctuations of intracellular forces during cell protrusion.', *Nature cell biology*, 10(12), pp. 1393–1400. doi: 10.1038/ncb1797.

Joe, S.S *et al.* (2020) 'The diffraction Barrier in Optical Microscopy'. Nikon: Microscopy – The source for microscopy education.

Jones, S. A., S. H. Shim., X. Zhuang. 2011. Fast, three-dimensional super-resolution imaging of live cells. Nat. Methods. 8:499–508.

Jungbauer, S. *et al.* (2008) 'Two characteristic regimes in frequency-dependent dynamic reorientation of fibroblasts on cyclically stretched substrates.', *Biophysical journal*, 95(7), pp. 3470–3478. doi: 10.1529/biophysj.107.128611.

Karamanou, M. *et al.* (2010) 'Anton van Leeuwenhoek (1632-1723): Father of micromorphology and discoverer of spermatozoa', *Revista Argentina de Microbiologia*, 42(4), pp. 311–314. doi: 10.1590/S0325-75412010000400013.

Katz, B. Z. *et al.* (2000) 'Physical state of the extracellular matrix regulates the structure and molecular composition of cell-matrix adhesions.', *Molecular biology of the cell*, 11(3), pp. 1047–1060. doi: 10.1091/mbc.11.3.1047.

Kawata, S., Inouye, Y. & Verma, P. (2009) *Nature Photon.* 3, 388–394

Kim M, Carman CV, Springer TA. (2003) Bidirectional transmembrane signaling by cytoplasmic domain separation in integrins. Science. 301:1720–1725. [PubMed: 14500982]

Kim, C., Ye, F. and Ginsberg, M. H. (2011) 'Regulation of integrin activation', *Annual Review of Cell and Developmental Biology*, 27, pp. 321–345. doi: 10.1146/annurev-cellbio-100109-104104.

Kim, M. C. *et al.* (2013) 'Dynamic Modeling of Cell Migration and Spreading Behaviors on Fibronectin Coated Planar Substrates and Micropatterned Geometries', *PLoS Computational Biology*, 9(2). doi: 10.1371/journal.pcbi.1002926.

Kühlbrandt, W. (2014) Science 343, 1443-1444.

Klapholz, B. and Brown, N. H. (2017) 'Talin - The master of integrin adhesions', *Journal of Cell Science*, 130(15), pp. 2435–2446. doi: 10.1242/jcs.190991.

Kleinman, H. K., Klebe, R. J. and Martin, G. R. (1981) 'Role of collagenous matrices in the adhesion and growth of cells', *Journal of Cell Biology*, 88(3), pp. 473–485. doi: 10.1083/jcb.88.3.473.

Klemke, R.L., et al., CAS/Crk coupling serves as a "molecular switch" for induction of cell migration, J. Cell Biol. 140 (4) (1998) 961–972

Kwakwa, K. *et al.* (2016) 'easySTORM: a robust, lower-cost approach to localisation and TIRF microscopy', 957(9), pp. 948–957. doi: 10.1002/jbio.201500324.

Lämmermann, T. *et al.* (2008) 'Rapid leukocyte migration by integrin-independent flowing and squeezing', *Nature*, 453(7191), pp. 51–55. doi: 10.1038/nature06887.

Lane, N. (2015) 'The unseen World: Reflections on Leeuwenhoek (1677) "Concerning little animals"', *Philosophical Transactions of the Royal Society B: Biological Sciences*, 370(1666). doi: 10.1098/rstb.2014.0344.

Lawson, C. *et al.* (2012) 'FAK promotes recruitment of talin to nascent adhesions to control cell motility', *Journal of Cell Biology*, 196(2), pp. 223–232. doi: 10.1083/jcb.201108078.

Leontieva, O. V., Demidenko, Z. N. and Blagosklonny, M. V. (2014) 'Contact inhibition and high cell density deactivate the mammalian target of rapamycin pathway, thus suppressing the senescence program', *Proceedings of the National Academy of Sciences of the United States of America*, 111(24), pp. 8832–8837. doi: 10.1073/pnas.1405723111.

Li, H. and Vaughan, J.C. (2019) 'HHS Public Access', 118(18), pp. 9412–9454. doi: 10.1021/acs.chemrev.7b00767.Switchable.

Linster, C. L. and Schaftingen, E. Van (2007) 'Biosynthesis, recycling and degradation in mammals', 274, pp. 1–22. doi: 10.1111/j.1742-4658.2006.05607.x.

Liu, K. *et al.* (2019) 'Synthetic Extracellular Matrices with Nonlinear Elasticity Regulate Cellular Organization', *Biomacromolecules*, 20(2), pp. 826–834. doi: 10.1021/acs.biomac.8b01445.

Liang, E. I. *et al.* (2017) 'Correlation of focal adhesion assembly and disassembly with cell migration on nanotopography.', *Integrative biology : quantitative biosciences from nano to macro*, 9(2), pp. 145–155. doi: 10.1039/c6ib00193a.

Ilić D, Kovacic B, Johkura K, Schlaepfer DD, Tomasević N, Han Q. (2004) FAK promotes organization of fibronectin matrix and fibrillar adhesions. J Cell Sci; 117:177-87; PMID:14657279; http://dx.doi.org/10.1242/jcs.00845

Lock, JG, Wehrle-Haller B, and Strömblad S. (2007) Cell-matrix adhesion complexes: master control machinery of cell migration. Semin. Cancer Biol. ; 18(1):65-76. [PMID: 18023204]

Lumkwana, D., Engelbrecht, L. and Loos, B. (2021) *Monitoring autophagy using super-resolution structured illumination and direct stochastic optical reconstruction microscopy*. 1st edn, *Methods in Cell Biology*. 1st edn. Elsevier Inc. doi: 10.1016/bs.mcb.2020.12.005.

Maheshwari, G. *et al.* (2000) 'Cell adhesion and motility depend on nanoscale RGD clustering.', *Journal of cell science*. England, 113 (Pt 10), pp. 1677–1686.

Maître, J.-L. and Heisenberg, C.-P. (2011) 'The role of adhesion energy in controlling cell-cell contacts.', *Current opinion in cell biology*, 23(5), pp. 508–514. doi: 10.1016/j.ceb.2011.07.004.

Manahan, C. L., Iglesias, P. A., Long, Y. and Devreotes, P. N. (2004). Chemoattractant signaling in dictyostelium discoideum. Annu. Rev. Cell. Dev. Biol. 20, 223-253.

Martin-Fernandez, M. L., Tynan, C. J. and Webb, S. E. D. (2013) 'A "pocket guide" to total internal reflection fluorescence', *Journal of Microscopy*, 252(1), pp. 16–22. doi: 10.1111/jmi.12070.

Mattheyses, A. L., Simon, S. M. & Rappoport, J. Z. (2010) Imaging with total internal reflection fluorescence microscopy for the cell biologist. J Cell Sci. Nov 1; 123(21): 3621–3628. doi: 10.1242/jcs.056218

Mattheyses, A. L., Shaw, K., and Axelrod, D., (2006) Microsc. Res. Tech. 69, 642–647

Martel, V. *et al.* (2001) 'Conformation, Localization, and Integrin Binding of Talin Depend on Its Interaction with Phosphoinositides', *Journal of Biological Chemistry*, 276(24), pp. 21217–21227. doi: 10.1074/jbc.M102373200.

Martino, F. *et al.* (2018) 'Cellular mechanotransduction: From tension to function', *Frontiers in Physiology*, 9(JUL), pp. 1–21. doi: 10.3389/fphys.2018.00824.

Martynov, V. I. *et al.* (2016) 'Synthetic Fluorophores for Visualizing Biomolecules in Living Systems', 8(31), pp. 33–46.

Mayer, A. *et al.* (1990) 'Two-Photon Laser Scanning Fluorescence Microscopy', (April), pp. 1–

McFadden, J. T. (2000) 'History of the operating microscope: From magnifying glass to microneurosurgery [4]', *Neurosurgery*, 46(2), p. 511. doi: 10.1097/00006123-200002000-00059.

McNamara, G. *et al.* (2017) 'Microscopy and image analysis', *Current Protocols in Human Genetics*, 2017(August), pp. 4.4.1-4.4.89. doi: 10.1002/cphg.42.

Macan Meščić, A., Gazivoda Kraljević, T. and Raić-Malić, S. (2019) 'Therapeutic Perspective of Vitamin C and Its Derivatives.', *Antioxidants (Basel, Switzerland)*, 8(8). doi: 10.3390/antiox8080247.

Mennens, S. F. B. *et al.* (2017) 'Substrate stiffness influences phenotype and function of human antigen-presenting dendritic cells', *Scientific Reports*, 7(1), p. 17511. doi: 10.1038/s41598-017-17787-z.

Merchant, F. A. and Castleman, K. R. (2009) *Chapter 27 - Computer-Assisted Microscopy*. 1st edn, *The Essential Guide to Image Processing*. 1st edn. Elsevier. doi: 10.1016/B978-0-12-374457-9.00027-5.

Mese G, Richard G, White TW. (2007) Gap junctions: Basic structure and function. J Invest Dermatol.; 127:2516–2524. [PubMed: 17934503]

Metcalf, D. J. *et al.* (2013) 'Test Samples for Optimizing STORM Super-Resolution Microscopy', (September), pp. 1–17. doi: 10.3791/50579.

Mitra, S. K., Hanson, D. A. and Schlaepfer, D. D. (2005) 'Focal adhesion kinase: In command and control of cell motility', *Nature Reviews Molecular Cell Biology*, 6(1), pp. 56–68. doi: 10.1038/nrm1549.

Molony, L. and Burridge, K. (1985) 'Molecular shape and self-association of vinculin and metavinculin', *Journal of Cellular Biochemistry*, 29(1), pp. 31–36. doi: 10.1002/jcb.240290104.

Momethylase, C. (2002) 'A Photoactivatable GFP for Selective Photolabeling of Proteins and Cells', 297(September), pp. 1873–1878.

Mouw, J. K., Ou, G. and Weaver, V. M. (2014) 'Extracellular matrix assembly: a multiscale deconstruction.', *Nature reviews. Molecular cell biology*, 15(12), pp. 771–785. doi: 10.1038/nrm3902.

Mukamel, E. A., Babcock, H. and Zhuang, X. (2012) 'Statistical Deconvolution for Superresolution Fluorescence Microscopy', *Biophysj*. Biophysical Society, 102(10), pp. 2391–2400. doi: 10.1016/j.bpj.2012.03.070.

Nahidiazar, L., Agronskaia, A. V., Broertjes, J., van den Broek, B. and Jalink, K. (2016) 'Optimizing Imaging Conditions for Demanding Multi-Color Super Resolution Localization Microscopy. *PLoS ONE* 11 (7), e0158884. doi:10.1371/journal.pone.0158884

Nayal, A., Webb, D. J. and Horwitz, A. F. (2004). Talin: an emerging focal point of adhesion dynamics. Curr. Opin. Cell Biol. 16, 94-98.

Nimesh, N., Joon, D. and Nimesh, M. (2017) 'Advances in Microscopy-A Review', VIII(1).

Nusrat A, Brown GT, Tom J, Drake A, Bui TT, Quan C, Mrsny RJ. (2005) Multiple protein interactions involving proposed extracellular loop domains of the tight junction protein occludin. Mol Biol Cell. 16:1725–1734. [PubMed: 15659655]

Olivier, N. *et al.* (2013) 'Simple buffers for 3D STORM microscopy', *Biomedical Optics Express*, 4(6), p. 885. doi: 10.1364/boe.4.000885.

Otomo, K., Hibi, T. and Kozawa, Y. (2015) 'STED microscopy — super-resolution bio-imaging utilizing a stimulated emission depletion', (July), pp. 227–236. doi: 10.1093/jmicro/dfv036.

Padayatty, S. J. and Levine, M. (2016) 'Vitamin C: the known and the unknown and Goldilocks.', *Oral diseases*, 22(6), pp. 463–493. doi: 10.1111/odi.12446.

Park, J. S. *et al.* (2012) 'Seven year outcome-Chesterman', 32(16), pp. 3921–3930. doi: 10.1016/j.biomaterials.2011.02.019.

Paper, I., Gundlach, H. and Zeiss, C. (1846) 'Phase contrast and DIC, instrumentation and applications in cell, developmental and marine The last 15 years saw a renaissance of light microscopy which was not expected in such a genes and chromosomes also in combination with transmitted light contras', 1846, pp. 126–139.

Parsons, J. T. *et al.* (2000) 'Focal Adhesion Kinase: A regulator of focal adhesion dynamics and cell movement', *Oncogene*, 19(49), pp. 5606–5613. doi: 10.1038/sj.onc.1203877.

Parhamifar, L. and Moghimi, S. M. (2012) 'Total internal reflection fluorescence (TIRF) microscopy for real-time imaging of nanoparticle-cell plasma membrane interaction.', *Methods in molecular biology (Clifton, N.J.)*. United States, 906, pp. 473–482. doi: 10.1007/978-1-61779-953-2_38.

Pasapera AM, Schneider IC, Rericha E, Schlaepfer DD, Waterman CM. (2010) Myosin II activity regulates vinculin recruitment to focal adhesions through FAK-mediated paxillin

phosphorylation. J Cell Biol; 188:877- 90; PMID:20308429; http://dx.doi.org/10.1083/jcb.200906012

Patterson, G. H. (2010) 'Fluorescence microscopy below the diffraction limit', 20(8), pp. 886–893. doi: 10.1016/j.semcdb.2009.08.006.Fluorescence.

Patterson, G. H. and Lippincott-schwartz, J. (2012) 'A Photoactivatable GFP for Selective Photolabeling of Proteins and Cells', 1873(2002). doi: 10.1126/science.1074952.

Pavel, M. *et al.* (2018) 'Contact inhibition controls cell survival and proliferation via YAP/TAZ-autophagy axis.', *Nature communications*, 9(1), p. 2961. doi: 10.1038/s41467-018-05388-x.

Pelham, R. J. and Wang, Y. (1997) 'Cell locomotion and focal adhesions are regulated by substrate flexibility', *Proceedings of the National Academy of Sciences*. National Academy of Sciences, 94(25), pp. 13661–13665. doi: 10.1073/pnas.94.25.13661.

Petrie, R. J. and Yamada, K. M. (2012) 'At the leading edge of three-dimensional cell migration', *Journal of Cell Science*, 125(24), pp. 5917–5926. doi: 10.1242/jcs.093732.

Phillips, C. L., Combs, S. B. and Pinnell, S. R. (1994) 'Effects of ascorbic acid on proliferation and collagen synthesis in relation to the donor age of human dermal fibroblasts', *Journal of Investigative Dermatology*. Elsevier Masson SAS, 103(2), pp. 228–232. doi: 10.1111/1523-1747.ep12393187.

Pinnell, S. R. (1985) 'Regulation of collagen biosynthesis by ascorbic acid: A review', *Yale Journal of Biology and Medicine*, 58(6), pp. 553–559.

Piston, D. W. (1998) 'Concepts in Imaging and Microscopy. Choosing objective lenses: The importance of numerical aperture and magnification in digital optical microscopy', *Biological Bulletin*, 195(1), pp. 1–4. doi: 10.2307/1542768.

Priddle, H. *et al.* (1998) 'Disruption of the talin gene compromises focal adhesion assembly in undifferentiated but not differentiated embryonic stem cells', *Journal of Cell Biology*, 142(4), pp. 1121–1133. doi: 10.1083/jcb.142.4.1121.

Pullar, J. M., Carr, A. C. and Vissers, M. C. M. (2017) 'The roles of vitamin C in skin health', *Nutrients*, 9(8). doi: 10.3390/nu9080866.

Rasnik, I., McKinney, S. A. & Ha, T. (2006) Nonblinking and long-lasting single- molecule fluorescence imaging. Nat. Methods 3, 891–893

Rees, E., et al. (2012) Blind Assessment of Localisation Microscope Image Resolution. Journal of Optical Nanoscopy. 1, 12, doi:10.1186/2192-2853-1-12

Ren, X. D. *et al.* (2000) 'Focal adhesion kinase suppresses Rho activity to promote focal adhesion', *Journal of Cell Science*, 113(20), pp. 3673–3678.

Renkawitz, J.; Kopf, A.; Stopp, J.; de Vries, I.; Driscoll, M. K.; Merrin, J.; Hauschild, R.; Welf, E. S.Danuser, G.; Fiolka, R.; Sixt, M. (**2019)** Nuclear Positioning Facilitates Amoeboid Migration along the Path of Least Resistance. *Nature*, *568* (7753), 546–550. https://doi.org/10.1038/s41586-019-1087-5.

Ricard-Blum, S. (2011) 'The collagen family.', *Cold Spring Harbor perspectives in biology*, 3(1), p. a004978. doi: 10.1101/cshperspect.a004978.

Riching, K. M. *et al.* (2015) '3D collagen alignment limits protrusions to enhance breast cancer cell persistence', *Biophysical Journal*. Biophysical Society, 107(11), pp. 2546–2558. doi: 10.1016/j.bpj.2014.10.035.

Robson, A. *et al.* (2018) 'Advantages and Limitations of Current Imaging Techniques for Characterizing Liposome Morphology', 9(February), pp. 1–8. doi: 10.3389/fphar.2018.00080.

Rochow, T. G. and Rochow, E. G. (1978) 'A Brief History of Microscopy', in *An Introduction to Microscopy by Means of Light, Electrons, X-Rays, or Ultrasound*. Boston, MA: Springer US, pp. 1–13. doi: 10.1007/978-1-4684-2454-6_1.

Rust, M. J., Bates, M. and Zhuang, X. (2006) 'imaging by stochastic optical reconstruction microscopy (STORM)', 3(10), pp. 793–795. doi: 10.1038/NMETH929.

Sanderson, M. J. *et al.* (2016) 'Cold Spring Harb Protoc', *Physiology & behavior*, 2014(10), pp. 1–36. doi: 10.1101/pdb.top071795.Fluorescence.

Saunders, R. M. *et al.* (2006) 'Role of vinculin in regulating focal adhesion turnover', *European Journal of Cell Biology*, 85(6), pp. 487–500. doi: 10.1016/j.ejcb.2006.01.014.

Sawhney, R. K. and Howard, J. (2002) 'Slow local movements of collagen fibers by fibroblasts drive the rapid global self-organization of collagen gels', *Journal of Cell Biology*, 157(6), pp. 1083–1091. doi: 10.1083/jcb.200203069.

Selinummi, J. *et al.* (2009) 'Bright Field Microscopy as an Alternative to Whole Cell Fluorescence in Automated Analysis of Macrophage Images', 4(10). doi: 10.1371/journal.pone.0007497.

Sellaro, T. *et al.* (2013) 'Relationship between magnification and resolution in digital pathology systems', *Journal of Pathology Informatics*, 4(1), p. 21. doi: 10.4103/2153-3539.116866.

Schaller, M.D., et al., (1992) pp 125FAK a structurally distinctive protein-tyrosine kinase associated with focal adhesions, Proc. Natl Acad. Sci. USA 89 (11) 5192–5196.

Schaller, M.D., et al., (1995) Focal adhesion kinase and paxillin bind to peptides mimicking beta integrin cytoplasmic domains, J. Cell Biol. 130 (5) 1181–1187.

Schramp, M. *et al.* (2012) *Erratum: Phosphoinositides I: Enzymes of synthesis and degradation [2012]*, *Sub-Cellular Biochemistry*. doi: 10.1007/978-94-007-3012-0.

Singh, A. (1998) 'Confocal Microscopy: a Powerful Tool for Biological Research Co11focal microscopy: A powerful technique for biological research'.

Shao, L. *et al.* (2008) 'I 5 S : Wide-Field Light Microscopy with 100-nm-Scale Resolution in Three Dimensions', 94(June), pp. 4971–4983. doi: 10.1529/biophysj.107.120352

Shattil, S. J., Kim, C. and Ginsberg, M. H. (2010) 'The final steps of integrin activation: the end game Sanford', *Changes*, 29(6), pp. 997–1003. doi: 10.1038/nrm2871.The.

Shroff, H., Galbraith, C., Galbraith, J., & Betzig, E. (2008) Live-cell photoactivated localization microscopy of nanoscale adhesion dynamics. Nature Methods. 5, 417-423, doi: 10.1038/nmeth.1202

Somaiah, C. *et al.* (2015) 'Collagen Promotes Higher Adhesion, Survival and Proliferation of Mesenchymal Stem Cells.', *PloS one*, 10(12), p. e0145068. doi: 10.1371/journal.pone.0145068.

Stehbens, S. J. and Wittmann, T. (2014) 'Analysis of focal adhesion turnover: a quantitative live-cell imaging example.', *Methods in cell biology*, 123, pp. 335–346. doi: 10.1016/B978-0-12-420138-5.00018-5.

Stokes, T. (1998) 'Principles and Application of Fluorescence'. doi: 10.1002/0471142727.mb1410s44.

Stutchbury, B. *et al.* (2017) 'Distinct focal adhesion protein modules control different aspects of mechanotransduction.', *Journal of cell science*, 130(9), pp. 1612–1624. doi: 10.1242/jcs.195362.

Sydor, A. M. *et al.* (2015) 'Super-Resolution Microscopy: From Single Molecules to Supramolecular Assemblies', *Trends in Cell Biology*. Elsevier Ltd, 25(12), pp. 730–748. doi: 10.1016/j.tcb.2015.10.004.

Takamizawa, S. (2004) 'Effects of ascorbic acid and ascorbic acid 2-phosphate, a long-acting vitamin C derivative, on the proliferation and differentiation of human osteoblast-like cells', *Cell Biology International*, 28(4), pp. 255–265. doi: 10.1016/j.cellbi.2004.01.010.

Tam, J. and Merino, D. (2015) 'Stochastic optical reconstruction microscopy (STORM) in comparison with stimulated emission depletion (STED) and other imaging methods', *Journal of Neurochemistry*, 135(4), pp. 643–658. doi: 10.1111/jnc.13257.

Tang, Q.Q., Otto, T. C. and Lane, M. D. (2004) 'Commitment of C3H10T1/2 pluripotent stem cells to the adipocyte lineage.', *Proceedings of the National Academy of Sciences of the United States of America*, 101(26), pp. 9607–9611. doi: 10.1073/pnas.0403100101.

Tham - Control, Q. (2017) 'Beating Rayleigh's Curse by Imaging Using Phase Information', 070801(February), pp. 1–6. doi: 10.1103/PhysRevLett.118.070801.

Thorn, K. and Kellogg, D. (2016) 'A quick guide to light microscopy in cell biology', 27. doi: 10.1091/mbc.E15-02-0088.

Thompson NL, Lagerholm BC. (1997) Total internal reflection fluorescence: applications in cellular biophysics. Curr Opin Biotechnol.; 8:58–64. [PubMed: 9013655]

Trappmann, B. and Chen, C. S. (2014) 'perspective', 24(5), pp. 948–953. doi: 10.1016/j.copbio.2013.03.020.How.

Trepat, X., Chen, Z. and Jacobson, K. (2012) 'Cell migration.', *Comprehensive Physiology*, 2(4), pp. 2369–2392. doi: 10.1002/cphy.c110012.

Valm, A.M *et al.,* (2017) Nature 536, 39-40

van de Linde, S., et al. (2011). Direct stochastic optical reconstruction microscopy with standard fluorescent probes. Nature protocols. 6, 991-1009, doi: 10.1038/nprot.2011.336

Van Seijen, M. *et al.* (2019) 'Impact of delayed and prolonged fixation on the evaluation of immunohistochemical staining on lung carcinoma resection specimen'. Virchows Archiv, pp. 191–199.

Velde, J. H. M. Van Der *et al.* (2018) 'A simple and versatile design concept for fluorophore derivatives with intramolecular photostabilization'. doi: 10.1038/ncomms10144.

Verdaasdonk, J. S. *et al.* (2014) 'Bending the Rules: Widefield Microscopy and the Abbe Limit of Resolution', *Journal of Cellular Physiology*, 229(2), pp. 132–138. doi: 10.1002/jcp.24439.

Vicente-Manzanares, M., Webb, D. J. and Horwitz, A. R. (2005) 'Cell migration at a glance', *Journal of Cell Science*, 118(21), pp. 4917–4919. doi: 10.1242/jcs.02662.

Vizcay-Barrena, G. *et al.* (2011) 'Subcellular and single-molecule imaging of plant fluorescent proteins using total internal reflection fluorescence microscopy (TIRFM)', *Journal of Experimental Botany*, 62(15), pp. 5419–5428. doi: 10.1093/jxb/err212.

Wang, P., Ballestrem, C. and Streuli, C. H. (2011) 'The C terminus of talin links integrins to cell cycle progression', *Journal of Cell Biology*, 195(3), pp. 499–513. doi: 10.1083/jcb.201104128.

Webb, R. L. *et al.* (2009) 'Using total internal reflection fluorescence (TIRF) microscopy to visualize cortical actin and microtubules in the Drosophila syncytial embryo', *Developmental Dynamics*, 238(10), pp. 2622–2632. doi: 10.1002/dvdy.22076.

Webster, K. D., Ng, W. P. and Fletcher, D. A. (2014) 'Tensional homeostasis in single fibroblasts.', *Biophysical journal*, 107(1), pp. 146–155. doi: 10.1016/j.bpj.2014.04.051.

Wegener KL, Partridge AW, Han J, Pickford AR, Liddington RC, Ginsberg MH, Campbell ID. (2007) Structural basis of integrin activation by talin. Cell.; 128:171–182. [PubMed: 17218263]

Wimmer, W. (2017) 'Carl Zeiss, Ernst Abbe, and Advances in the Light Microscope', *Microscopy Today*, 25(4), pp. 50–57. doi: 10.1017/s155192951700058x.

Wolf, K. and Friedl, P. (2011) 'Extracellular matrix determinants of proteolytic and non-proteolytic cell migration.', *Trends in cell biology*. England, 21(12), pp. 736–744. doi: 10.1016/j.tcb.2011.09.006.

Won, R. (2009) *Nature Photon.* **3**, 368–369

Wombacher, R., M. Heidbreder, M. Sauer. 2010. Live-cell super-resolution imaging with trimethoprim conjugates. Nat. Methods. 7: 717–719.

Wu, Y.-K. *et al.* (2020) 'The Influence of Cell Culture Density on the Cytotoxicity of Adipose-Derived Stem Cells Induced by L-Ascorbic Acid-2-Phosphate.', *Scientific reports*, 10(1), p. 104. doi: 10.1038/s41598-019-56875-0.

Xu, W., Baribault, H. and Adamson, E. D. (1998) 'Vinculin knockout results in heart and brain defects during embryonic development', *Development*, 125(2), pp. 327–337.

Xu, J., Ma, H. and Liu3, Y. (2018) 'stochastic optical microscopy (STORM)', *Current Protocols in Cytometry*, 15(5), pp. 477–491. doi: 10.1002/cpcy.23.Stochastic.

Yamada, K. M. (2019) 'Mechanisms of 3D cell migration', *Nature Reviews Molecular Cell Biology*. Springer US, 20(DECEMBER). doi: 10.1038/s41580-019-0172-9.

Yamann, R. L. and Mahesh, M. (2018) 'The Importance of Spatial Resolution to Medical Imaging', *Journal of the American College of Radiology*. American College of Radiology, 15(8), p. 1127. doi: 10.1016/j.jacr.2018.03.042.

Yamanaka, M., Smith, N. I. and Fujita, K. (2014) 'Introduction to super-resolution microscopy', pp. 177–192. doi: 10.1093/jmicro/dfu007.

Yamamoto, Y. and Shinohara, K. (2002) 'Application of X-ray microscopy in analysis of living hydrated cells', *Anatomical Record*, 269(5), pp. 217–223. doi: 10.1002/ar.10166.

Yao, Z. and Carballido-l, R. (2014) 'Fluorescence Imaging for Bacterial Cell Biology: From Localization to Dynamics, From Ensembles to Single Molecules', (June), pp. 459–476. doi: 10.1146/annurev-micro-091213-113034.

Yoshigi, M. *et al.* (2005) 'Mechanical force mobilizes zyxin from focal adhesions to actin filaments and regulates cytoskeletal reinforcement.', *The Journal of cell biology*, 171(2), pp. 209–215. doi: 10.1083/jcb.200505018.

Zamir, E. and Geiger, B. (2001) 'Molecular complexity and dynamics of cell-matrix adhesions.', *Journal of cell science*. England, 114(Pt 20), pp. 3583–3590.

Zhang, X. *et al.* (2008) 'Talin depletion reveals independence of initial cell spreading from integrin activation and traction.', *Nature cell biology*, 10(9), pp. 1062–1068. doi: 10.1038/ncb1765.

Zhao, X. and Guan, J. (2011) 'Focal adhesion kinase and its signaling pathways in cell migration and angiogenesis', *Advanced Drug Delivery Reviews*. Elsevier B.V., 63(8), pp. 610–615. doi: 10.1016/j.addr.2010.11.001.

Zhenga, Qinsi Manuel F. Juettea, Steffen Jockuschc, Michael R. Wassermana, Zhou Zhoua, Roger B. Altmana, and S. C. B. (2012) 'Ultra-Stable Organic Fluorophores for Single-Molecule Research', 76(October 2009), pp. 211–220. doi: 10.1039/c3cs60237k.Ultra-Stable.

Zhong, H. (2010) 'Photoactivated Localization Microscopy (PALM): An Optical Technique for Achieving ~ 10-nm Resolution', pp. 1325–1336. doi: 10.1101/pdbtop91.

Zhuang, X. (2009) *Nature Photon.* 3, 365–367

Ziegler, W. H., Liddington, R. C. and Critchley, D. R. (2006) 'The structure and regulation of vinculin.', *Trends in cell biology*. England, 16(9), pp. 453–460. doi: 10.1016/j.tcb.2006.07.004.

# Chapter 10: Appendices

## Appendix A: Ethical Exemption

UNIVERSITEIT•STELLENBOSCH•UNIVERSITY
jou kennisvennoot • your knowledge partner

**PROJECT EXEMPT FROM ETHICS CLEARANCE**

15 April 2020

Project number: **BEE-2020-1604E**

Title: Using TIRF and STORM in tandem to investigate adherence and migration patterns in stem cells (C3H10T1/2 cells).

Dear Dr M Van de Vyver

Your application received on **18 February 2020** was reviewed by the REC: Biosafety and Environmental Ethics. You have confirmed in the proposal submitted for review that you do not transfect any of the cell lines as part of our routine laboratory work and that all the cell lines you intend to use are classified at BSL1 safety conditions.

The project is, therefore, exempt from ethics review and clearance. You may commence with your project as set out in the submission to the Research Ethics Committee: Biosafety and Environmental Ethics.

If the research deviates from the application submitted for REC clearance, the researcher must notify the REC of these changes well before the amendment commences. In certain circumstances, a new application may be required for the project.

Please remember to use your project number (BEE-2020-1604E) on any documents or correspondence with the REC concerning your project.

Sincerely,

REC Coordinator: Research Ethics Committee: Animal Care and Use (REC: ACU)
Tel:

## Appendix B: Wide Field and Confocal Settings Antibody Titrations

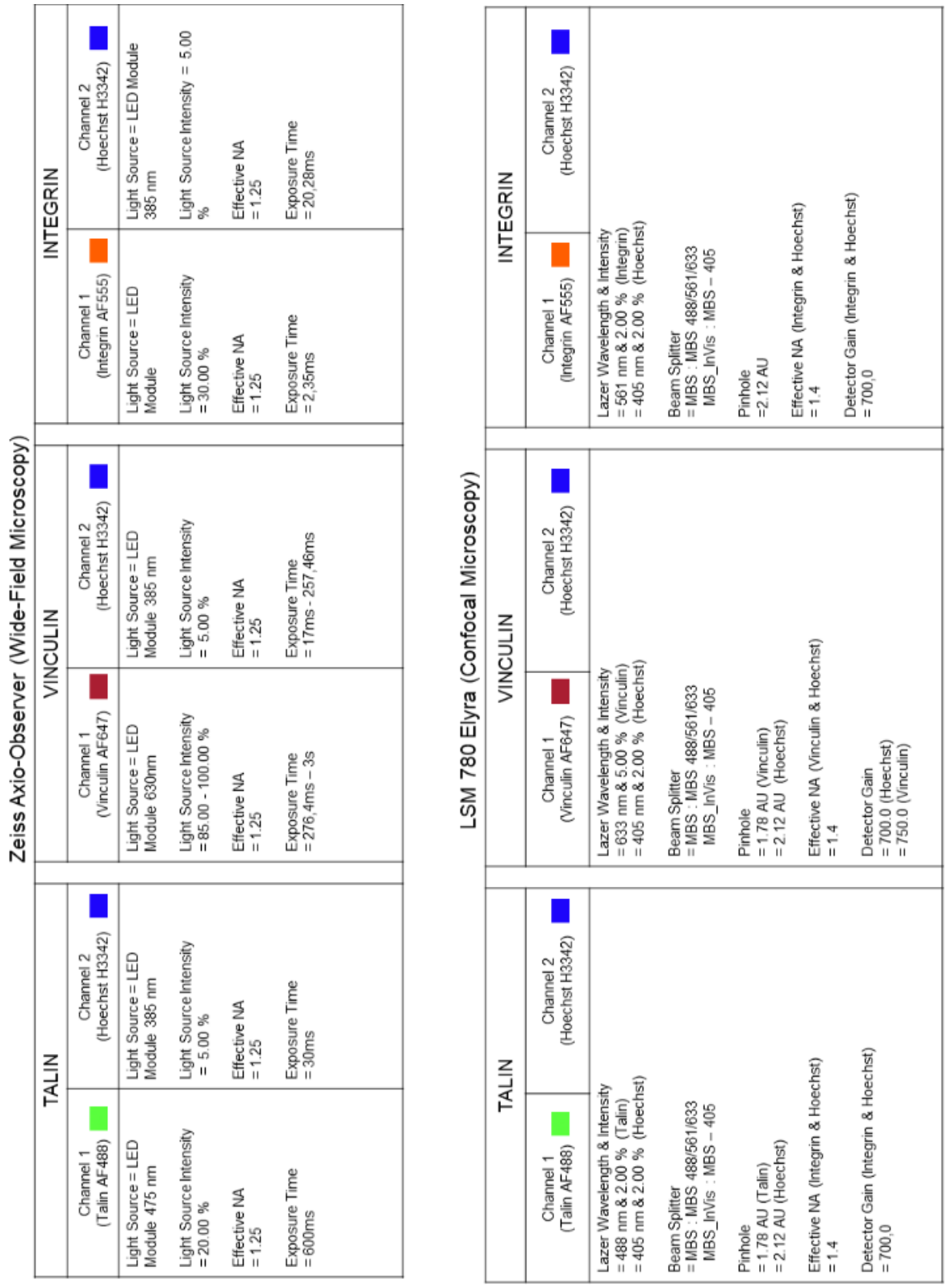

**Zeiss Axio-Observer (Wide-Field Microscopy)**

| TALIN | | VINCULIN | | INTEGRIN | |
|---|---|---|---|---|---|
| Channel 1 (Talin AF488) | Channel 2 (Hoechst H3342) | Channel 1 (Vinculin AF647) | Channel 2 (Hoechst H3342) | Channel 1 (Integrin AF555) | Channel 2 (Hoechst H3342) |
| Light Source = LED Module 475 nm | Light Source = LED Module 385 nm | Light Source = LED Module 630nm | Light Source = LED Module 385 nm | Light Source = LED Module | Light Source = LED Module 385 nm |
| Light Source Intensity = 20.00 % | Light Source Intensity = 5.00 % | Light Source Intensity = 85.00 - 100.00 % | Light Source Intensity = 5.00 % | Light Source Intensity = 30.00 % | Light Source Intensity = 5.00 % |
| Effective NA = 1.25 | Effective NA = 1.25 | Effective NA = 1.25 | Effective NA = 1.25 | Effective NA = 1.25 | Effective NA = 1.25 |
| Exposure Time = 600ms | Exposure Time = 30ms | Exposure Time = 276,4ms – 3s | Exposure Time = 17ms - 257,46ms | Exposure Time = 2,35ms | Exposure Time = 20,28ms |

**LSM 780 Elyra (Confocal Microscopy)**

| TALIN | | VINCULIN | | INTEGRIN | |
|---|---|---|---|---|---|
| Channel 1 (Talin AF488) | Channel 2 (Hoechst H3342) | Channel 1 (Vinculin AF647) | Channel 2 (Hoechst H3342) | Channel 1 (Integrin AF555) | Channel 2 (Hoechst H3342) |
| Lazer Wavelength & Intensity = 488 nm & 2.00 % (Talin) = 405 nm & 2.00 % (Hoechst) | | Lazer Wavelength & Intensity = 633 nm & 5.00 % (Vinculin) = 405 nm & 2.00 % (Hoechst) | | Lazer Wavelength & Intensity = 561 nm & 2.00 % (Integrin) = 405 nm & 2.00 % (Hoechst) | |
| Beam Splitter = MBS : MBS 488/561/633 MBS_InVis : MBS – 405 | | Beam Splitter = MBS : MBS 488/561/633 MBS_InVis : MBS – 405 | | Beam Splitter = MBS : MBS 488/561/633 MBS_InVis : MBS – 405 | |
| Pinhole = 1.78 AU (Talin) = 2.12 AU (Hoechst) | | Pinhole = 1.78 AU (Vinculin) = 2.12 AU (Hoechst) | | Pinhole =2.12 AU | |
| Effective NA (Integrin & Hoechst) = 1.4 | | Effective NA (Vinculin & Hoechst) = 1.4 | | Effective NA (Integrin & Hoechst) = 1.4 | |
| Detector Gain (Integrin & Hoechst) = 700,0 | | Detector Gain = 700.0 (Hoechst) = 750.0 (Vinculin) | | Detector Gain (Integrin & Hoechst) = 700,0 | |

## Appendix C: TIRF and STORM Settings

**A:** Flow Chart

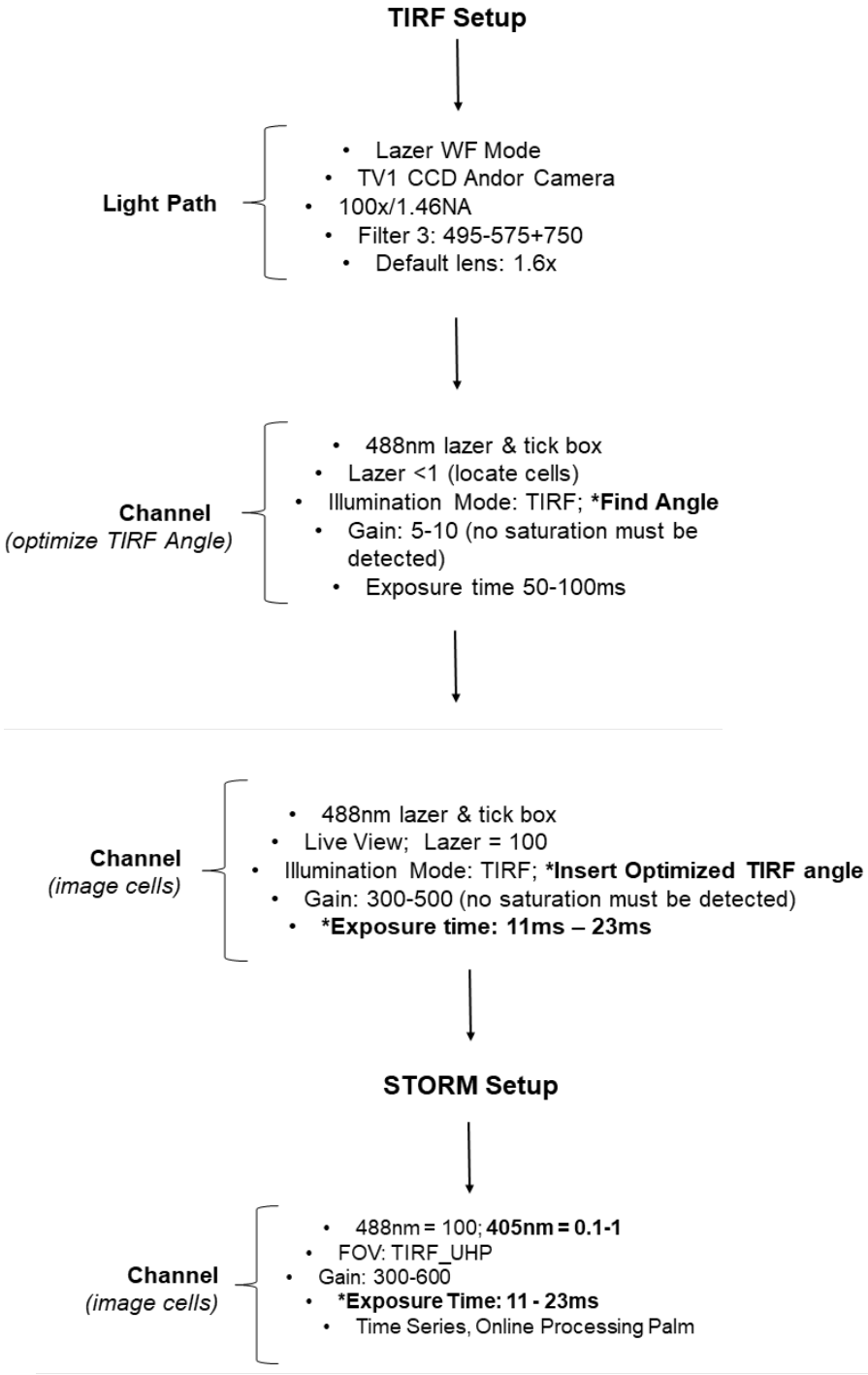

**B:** TIRF optimal fixative

| Fixative | TIRF angle | Exposure Time | Gain | TIRF representation (5µm) |
|---|---|---|---|---|
| Methanol | 58.02° - 58.92° | 24ms | 400 | 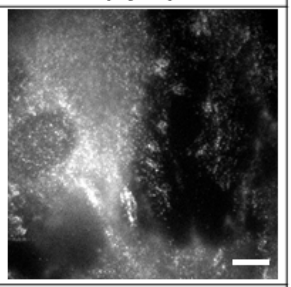 |
| 2.5% Glutaraldehyde | 60.42° – 61.32° | 20ms | 460 | 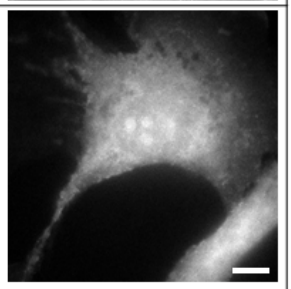 |

| Fixative | TIRF angle | Exposure Time | Gain | TIRF representation (5µm) |
|---|---|---|---|---|
| 4% Formaldehyde | 59.32° - 61.32° | 13ms | 500 | 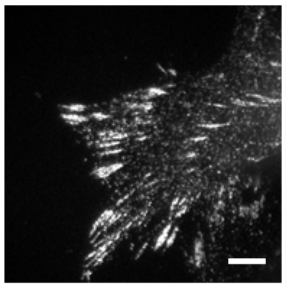 |
| 2.5% Glutaraldehyde & 4% Formaldehyde | 55.52° – 56.41° | 25ms | 450 | 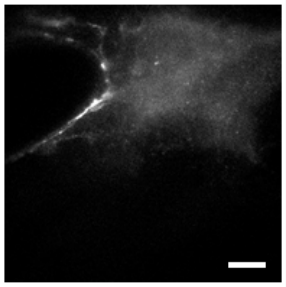 |

**C:** STORM optimal fixative (with TIRF)

| Fixative | TIRF angle | Exposure Time | Gain | STORM representation (2µm) |
|---|---|---|---|---|
| Methanol | 58.12° | 27ms | 370 | 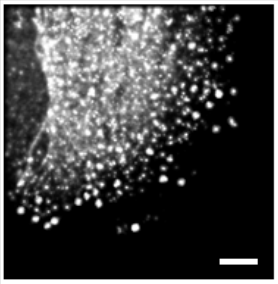 |
| 2.5% Glutaraldehyde | 61.73° | 19ms | 430 | 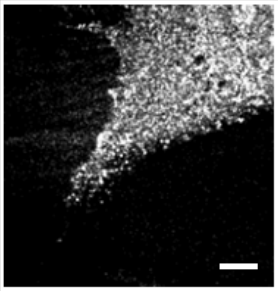 |

| Fixative | TIRF angle | Exposure Time | Gain | STORM representation (2µm) |
|---|---|---|---|---|
| 4% Formaldehyde | 61.74° | 22ms | 470 | 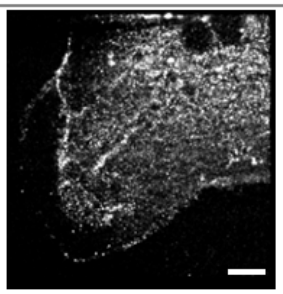 |
| 2.5% Glutaraldehyde & 4% Formaldehyde | 58.32° | 11ms | 350 | 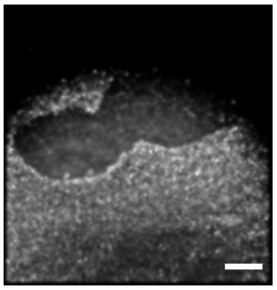 |

## Appendix D: 24h Live Cell Migration

**A:** AAP treated media

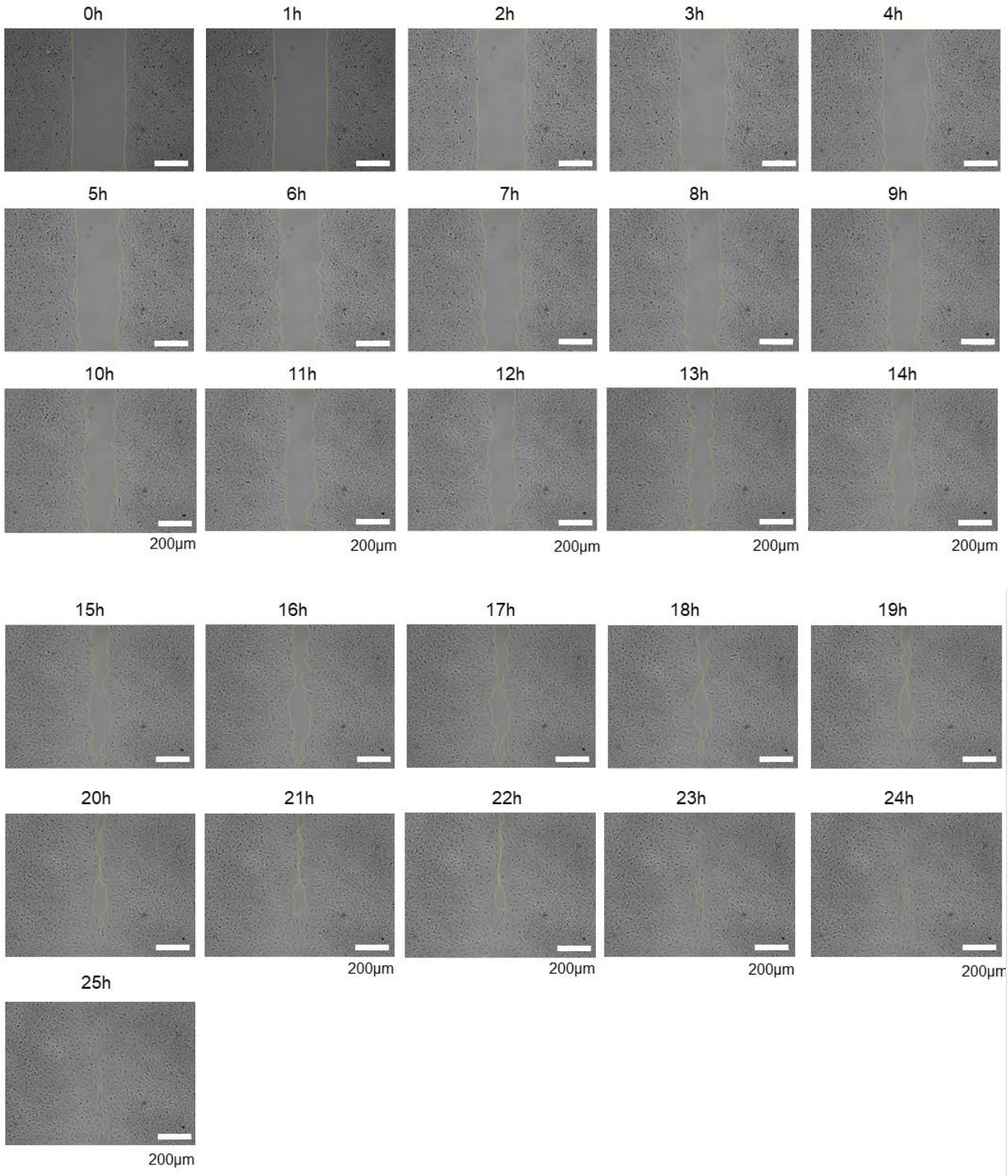

**B:** Standard Growth Media

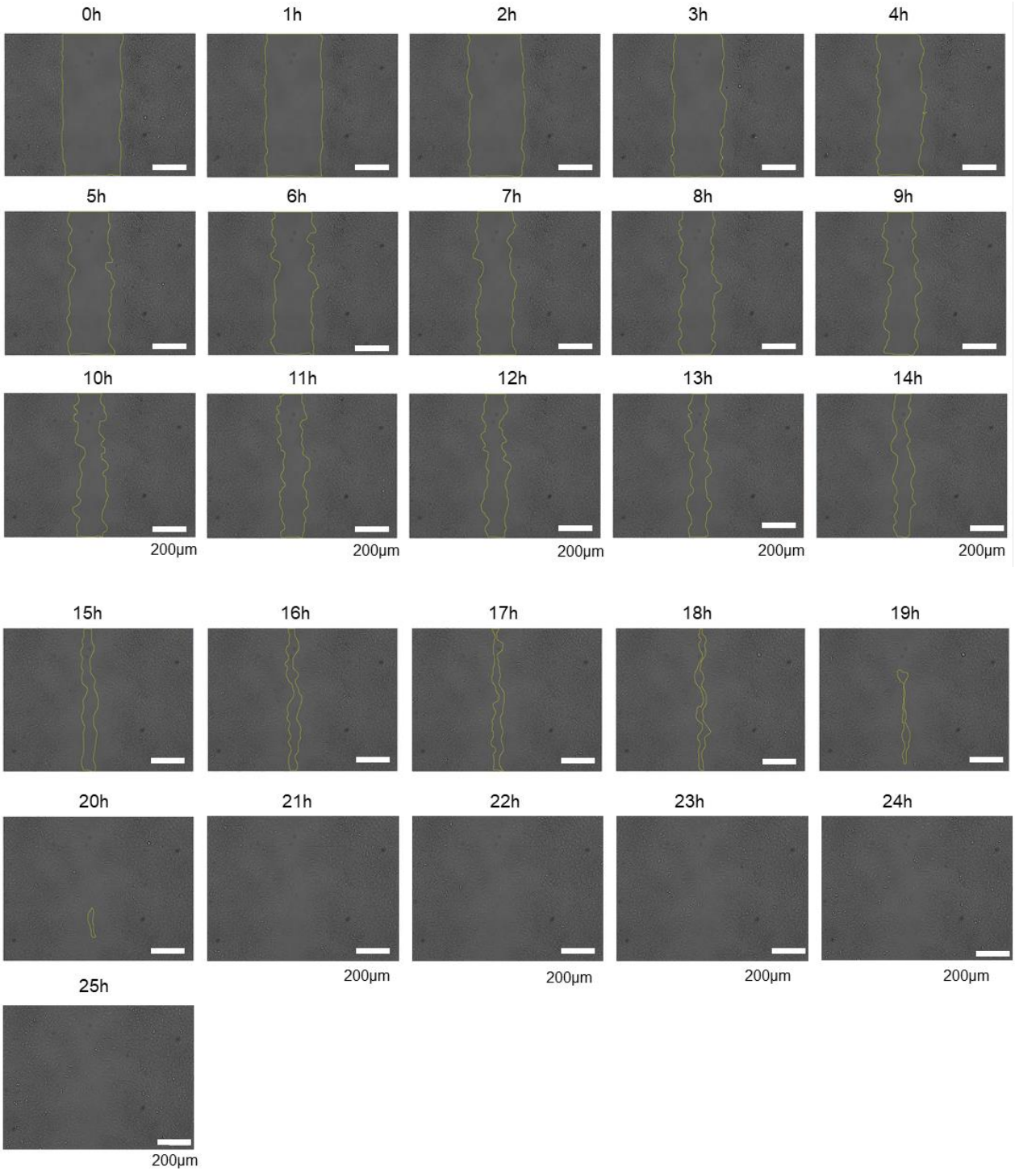

**C:** Standard Growth Media with Mit C

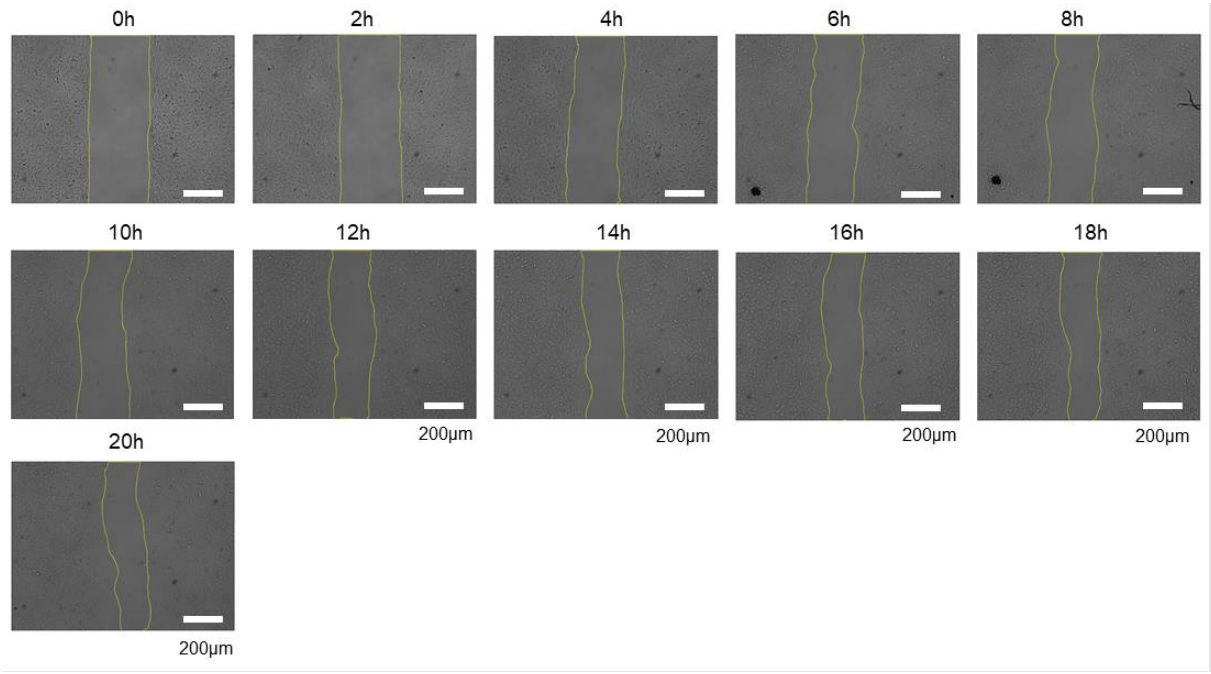


**D:** AAP Treated Media with Mit C

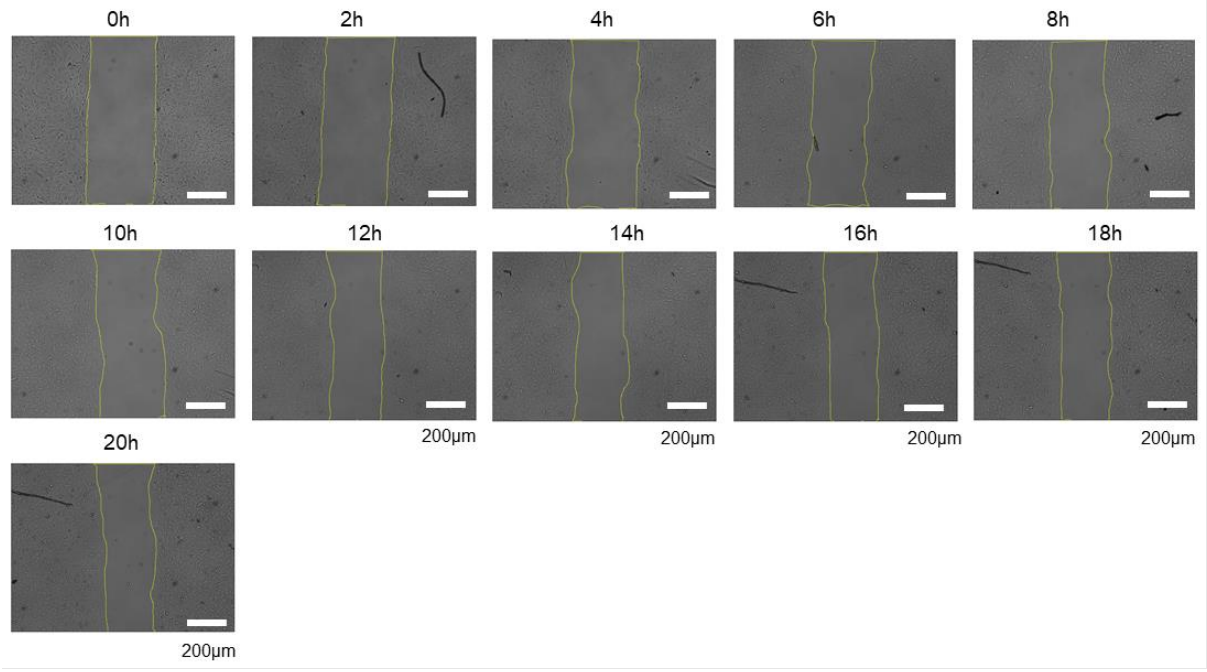

## Appendix E: Image Permissions

**A:** Figure 2.1.6 A

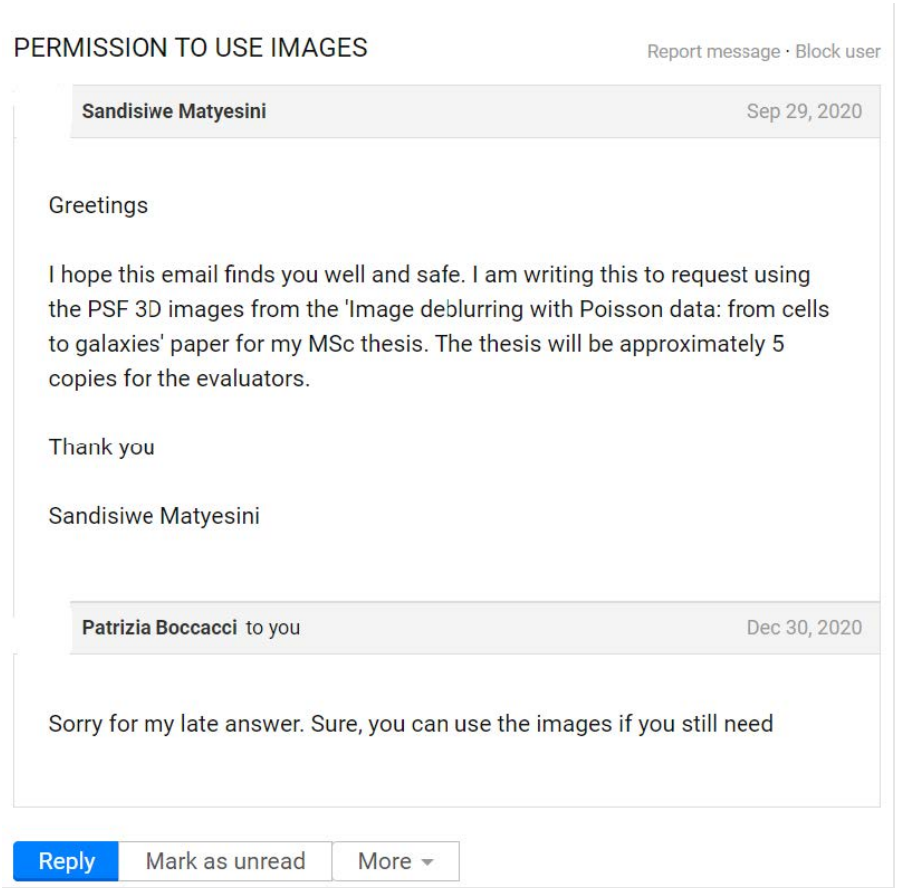


**B:** Figure 2.1.6B